The Dissertation Committee for Thomas Eugene Murphy
certifies that this is the approved version of the following dissertation:

Artificial Leaf for Biofuel Production and Harvesting: Transport Phenomena and Energy Conversion

Committee:

_____
Halil Berberoglu, Supervisor

_____
Brad Bebout

_____
Alexandre da Silva

_____
Erich Fleming

_____
Carlos Hidrovo

_____
John Howell

Artificial Leaf for Biofuel Production and Harvesting: Transport Phenomena and Energy Conversion

by

Thomas Eugene Murphy, B.S., M.S.E.

DISSERTATION

Presented to the Faculty of the Graduate School of

The University of Texas at Austin

in Partial Fulfillment

of the Requirements

for the Degree of

DOCTOR OF PHILOSOPHY

THE UNIVERSITY OF TEXAS AT AUSTIN

August 2013

Dedicated to my family.

To my parents, Dana and Mike, and my brothers, Dan and Jack, for their truly unconditional love and support.
And to my grandparents, Mona and Jim McNeese, Tom Zimmerman, and Mary and Gene Murphy for their tremendous encouragement.

Acknowledgments

I would like to gratefully acknowledge my advisor, Halil Berberoglu for his immense effort in guiding these studies toward their fullest potential. I'd also like to sincerely thank Altan Ozkan, Onur Taylan and Akhil Kulkarni. Their friendship and expertise tremendously enhanced my experience in the Solar Energy and Biofuels Lab, here in Austin, TX. I would also like to thank all of the lab members for a friendly and hard working lab environment: Angel Wileman, Edwin Peng, Babak Nasouri, Mahesh Venkatesan, Rudy Torres, and Luis Galindo.

I would like to sincerely thank Victoria Work and Matthew Posewitz for providing the *Synechococcus* sp. strain used in the experimental synthetic leaf study, as well as for their valuable guidance in working with the strain. I would like to express my sincere gratitude to Dwight Romanovicz in the UT-Austin Institute for Cellular and Molecular Biology for his invaluable expertise in generating the SEM and TEM images of the *Synechococcus* sp. I also thank Rhykka Connelly for generously offering her time, expertise, and equipment for teaching me the thin layer chromatography procedure. I would also like to thank Danny Jares and Sara Norris for their tireless effort in constructing the chambers for housing the synthetic leaves. Furthermore, I gratefully acknowledge the intellectual contributions of Evan Fleming and Carlos Hidrovo to the

study modeling the vascular transport system. I'd also like to thank Robert Crawford and Alex da Silva for their helpful discussions.

I would like to sincerely thank the members of the Exobiology lab at NASA Ames Research Center: Lee and Brad Bebout, Erich Fleming, and Angela Detweiler, for the personal and professional hospitality they showed me during the summers of 2011 and 2012. Moreover, I sincerely thank Angela Detweiler for her help with cultivating the microorganisms and designing and building the experimental setup for the spectral scoring study (Appendix A).

Additionally, I cannot express fully enough my appreciation for the hard work and friendship of Keith Macon, an undergraduate researcher with wisdom truly beyond his years. Keith was the second author for the multispectral imaging paper presented in Chapter 5 as he performed most of the experiments for that study. Keith also contributed in some way to much of the other research presented here, and provided the lab with an optimistic spirit and intellectual curiosity.

I'd like to thank and wish the best of luck to Ethan Rohrer, with whom I had the distinct pleasure of working for the last two years. I would also like to thank Begum Baysan for her time and effort in finding and nicely summarizing many of the journal articles cited in this dissertation.

I cannot complete any notable engineering accomplishment without paying homage to my dear friends Jeff Manian and Max Tuttman, without whom I probably wouldn't have even become an engineer. I might have become

something else entirely. I'd like to thank my dear friend and colleauge, Nathan Putnam, for his guidance and companionship.

I cannot thank enough my roommates over the last four years: Stephen Salisbury, Cassie Mitchell, Caitlin Boehne, and, I guess, Dane Jensen. The patience these folks showed while I shirked general life duties in pursuit of the research presented in this dissertation has been truly remarkable. Thank you.

Artificial Leaf for Biofuel Production and Harvesting: Transport Phenomena and Energy Conversion

Thomas Eugene Murphy, Ph.D.
The University of Texas at Austin, 2013

Supervisor: Halil Berberoglu

Microalgae cultivation has received much research attention in recent decades due to its high photosynthetic productivity and ability to produce biofuel feedstocks as well as high value compounds for the health food, cosmetics, and agriculture markets. Microalgae are conventionally grown in open pond raceways or closed photobioreactors. Due to the high water contents of these cultivation systems, they require large energy inputs for pumping and mixing the dilute culture, as well as concentrating and dewatering the resultant biomass. The energy required to operate these systems is generally greater than the energy contained in the resultant biomass, which precludes their use in sustainable biofuel production. To address this challenge, we designed a novel photobioreactor inspired by higher plants. In this synthetic leaf system, a modified transpiration mechanism is used which delivers water and nutrients to photosynthetic cells that grow as a biofilm on a porous, wicking substrate.

Nutrient medium flow through the reactor is driven by evaporation, thereby eliminating the need for a pump.

This dissertation outlines the design, construction, operation, and modeling of such a synthetic leaf system for energy positive biofuel production. First, a scaled down synthetic leaf reactor was operated alongside a conventional stirred tank photobioreactor. It was demonstrated that the synthetic leaf system required only 4% the working water volume as the conventional reactor, and showed growth rates as high as four times that of the conventional reactor. However, inefficiencies in the synthetic leaf system were identified and attributed to light and nutrient limitation of growth in the biofim. To address these issues, a modeling study was performed with the aim of balancing the fluxes of photons and nutrients in the synthetic leaf environment. The vascular nutrient medium transport system was also modeled, enabling calculation of nutrient delivery rates as a function of environmental parameters and material properties of the porous membrane. These models were validated using an experimental setup in which the nutrient delivery rate, growth rate, and photosynthetic yield were measured for single synthetic leaves. The synthetic leaf system was shown to be competitive with existing technologies in terms of biomass productivity, while requiring zero energy for nutrient and gas delivery to the microorganisms. Future studies should focus on utilizing the synthetic leaf system for passive harvesting of secreted products in addition to passive nutrient delivery.

Table of Contents

List of Tables

List of Figures

xviii

Chapter 1

Introduction

Algae cultivation is of commercial interest as its high photosynthetic productivity makes possible solar generation of biofuels, as well as food, cosmetic, and pharmaceutical products. Moreover, algae can utilize the nitrogen and phosphorous content of wastewater to support its growth, thus enabling bioproduct formation using an otherwise untapped resource. Conventionally, algae has been grown in open ponds or closed photobioreactors, both of which require large volumes of water and large energy inputs for operation. In contrast, vascular plants cultivate and transport bioproducts passively using very little water. This research aims to create a novel type of algae photobioreactor, inspired by vascular plants, for efficient, energy positive biofuel generation.

1.1 Applications of algal biomass cultivation and bioproduct harvesting

1.1.1 Algae as a biofuel source

Biofuels derived from microalgae have received much attention in recent decades [26–28, 114]. Unlike fossil fuels, the biofuel life cycle can be (i) carbon neutral, in that the CO_2 emitted by fuel combustion is recycled during biofuel crop growth, and (ii) renewable, as the sun is the energy source. Biofuels de-

rived from algae are particularly promising due to algae's high photosynethetic productivity and lipid content compared to conventional biofuel crops [26]. It was estimated that algae derived biofuels have a potential areal productivity as large as 250 times that of biofuel derived from conventional crops like corn and soybean [26]. Moreover, algae can grow in saline or brackish water and do not require arable land to grow.

Chemical energy can be extracted from algae in several ways. First, both green algae and cyanobacteria are capable of producing hydrogen gas, which can be used to power fuel cells [12, 14, 45]. Under anaerobic conditions, green algae use a hydrogenase enzyme to combine protons from the intracellular medium with electrons from either stored organic material or from water during oxygenic photosynthesis [45]. Moreover, nitrogen fixing cyanobacteria produce hydrogen gas as a byproduct of the conversion of nitrogen gas to ammonia [72]. In nature, the H_2 is consumed using the enzyme uptake hydrogenase, which is undesirable from a hydrogen production perspective. Thus, efforts have been made to genetically engineer cyanobacteria to lack uptake hydrogenase [129]. Solar to H_2 conversion efficiencies of up to 5-10% have been reported [45]. However, hydrogen gas can be difficult to harvest on a large scale due to concerns over leakage stemming from its high diffusivity. Furthermore, the lack of an existing hydrogen fuel infrastructure has limited its widespread acceptance as a fuel.

The majority of algal biofuel research is currently focused on the production of liquid fuels, particularly biodiesel [26, 105, 114]. To produce biodiesel

2

from algal biomass, first the lipids, specifically triaglycerides (TAGs), are extracted from the biomass using chemical and/or mechanical methods [100, 115]. Then, through a process called transesterification, an acid or alkali catalyst is used to convert TAGs and methanol to glycerol and fatty acid methyl esters (FAMEs), which is biodiesel [113]. The TAG content of microalgal strains varies between about 10% and 40%, although TAG contents as high as 80% have been observed under deprivation of essential nutrients, most commonly nitrogen [26, 112]. The effect of depriving cells of a nutrient on the lipid productivity of a culture must be carefully analyzed, as nutrient deprivation increases the lipid content per cell but decreases the growth rate [105, 112]. Genetic engineering of algae with high lipid content has also been proposed [35, 114].

Furthermore, anaerobic digestion of algal biomass produces natural gas (methane, CH_4), and has been proposed for renewable biogas generation [26, 117, 123]. In this process, which also naturally occurs in anoxic, aphotic aquatic zones, methanogenic anaerobes break down biomass and water into to methane (CH_4), carbon dioxide (CO_2), and ammonia (NH_3). It has been proposed that this technology be used in conjunction with commercial biodiesel plants as the methane can provide auxiliary power for plant operation and the ammonium generation provides a means of nitrogen recycling [26, 117]. Algal biogas, biohydrogen, and biodiesel generation have been demonstrated at the laboratory scale in numerous studies [27, 45, 117]. However, high capital and operating costs of large scale production have limited algal biofuels' commercial success.

3

1.1.2 Algae cultivation for non-biofuel products

As a result of the high costs of production of biofuels compared to conventional fuels, many commercial algae ventures have begun marketing algal bioproducts to the food, aquaculture, cosmetic, and pharmaceutical industries [33, 80, 108, 123]. These markets are characterized as high price, low volume markets, in contrast to the low price, high volume biofuels markets. As of 2006, the global microalgal biomass market had a size and annual turnover of 5,000 tons of dry biomass per year and \$1.3 billion, respectively [108]. About 30% of global algae production is used as animal feed, most of which is used in aquaculture for fish production [80]. The cyanobacterium *Spirulina* (also known as *Arthrospira*), and to a lesser extent the green alga *Chlorella*, are the primary genera used in this market. *Spirulina* and *Chlorella* are also sold as food for humans, but primarily as a supplement rather than a staple. These organisms are sold as powder and tablets, and are high in proteins and nutrients, as well as linolenic acid, an essential fatty acid [11, 123]. Moreover, diatoms, such as *Crypthecodinium conhii* and *Phaeodactylum tricornutum*, are producers of omega-3 fatty acids, the health benefits of which are well documented [23].

Additionally, phycobiliproteins, part of the photosynthetic machinery of cyanobacteria and red algae [24, 80], are currently sold as natural colorants for food products and cosmetics. The global market for phycobiliproteins is estimated at \$50 million. The market is supported primarily by the cyanobacterium *Spirulina* and the red algae *Porphyridium* and *Rhodella*. Green algae

are of interest for their production of carotenoids, which are also used as natural colorants for cosmetics and food products. Specifically, *Dunaliella* and *Haematococcus* are grown commercially for their production of β-carotene and astaxanthin, respectively. These products can also be used as animal feed supplements.

1.1.3 Algae for wastewater and waste gas remediation

Algal ponds have also been used to remove nitrates and phosphates from municipal, agricultural, and industrial waste streams [25, 30, 31, 89]. This technology abates eutrophication of natural waters with the added benefit of producing biofuel feedstock. Mulbry *et al.* used freshwater algae to treat dairy manure effluent and reported total nitrogen and total phosphorous consumption rates of 2.5 g/m^2-d and 0.42 g/m^2-d while cultivating biomass at a rate of 25 g/m^2-d [89]. Utilization of wastewater for algae cultivation can significantly reduce the cost of algae production by reducing nutrient costs as well as using existing water treatment facilities.

Algal photosynthesis has also been proposed as a method for capturing waste CO_2 from industrial processes as a means to mitigate global climate change [64, 102]. This concept has been demonstrated, but it is important to note that for the process to be carbon negative, the algal biomass must be sequestered rather than converted to biofuel, the combustion of which re-releases the captured CO_2. Algae have also been proposed as a candidate to recycle CO_2 exhaled by humans for advanced life support in space [46, 65, 93].

Currently, oxygen generation aboard the International Space Station relies on transport of water from Earth, and CO_2 and other waste is vented to space rather than being recycled. However, long duration space missions will requrire closed loop life support. As algae are responsible for most of the oxygen content in the Earth's atmosphere, they are a good candidate for oxygen production in space as well.

1.2   Challenges to large scale algae production

To this date, no company profitably produces algal biofuels. Chisti estimated that in order for algal biofuel to be competitive with conventional fuels, it would have to be produced at a cost of about $0.48/l, whereas this cost, as of 2007, was about $2.80/l [26]. It has also been shown that the majority of the costs of biofuel production come from growing the algae and harvesting the resultant biomass [10]. At large scales, algae are conventionally grown in open pond raceways and closed photobioreactors, examples of which are shown in Figure 1.1. Open pond raceways, generally about 1 m wide and 0.2 m deep, are open to the atmosphere and typically operate with microorganism concentrations of about 0.5 g/l [21]. On the other hand, closed photobioreactors, which can be planar or cylindrical in geometry and horizontally or vertically oriented, are closed to the atmosphere and operate using higher microorganism concentrations of 2 to 10 g/l [58]. Closed photobioreactors are generally more expensive to build and to operate than open raceways, but are less prone to contamination and typically provide larger biomass outputs.
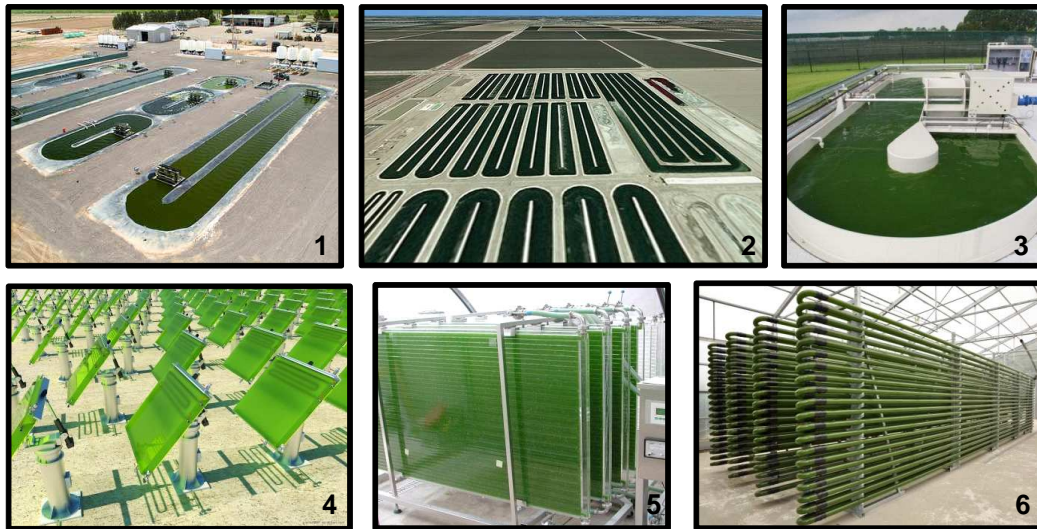
[1] http://www.biopondpaddlewheel.com/images/TX-PW-c.jpg
[2] http://www.pnnl.gov/news/release.aspx?id=859
[3] http://www.energyrealities.org/images/otc/input/content/598/w/erpB5E6A7E23592B6FDB.jpg
[4] http://fc00.deviantart.net/fs71/f/2012/123/a/7/photobioreactors_by_silentcenter-d4ydxjj.jpg
[5] http://upload.wikimedia.org/wikipedia/commons/0/0f/Photobioreactor_PBR_500_P_IGV_Biotech.jpg
[6] http://upload.wikimedia.org/wikipedia/commons/b/ba/Photobioreactor_PBR_4000_G_IGV_Biotech.jpg

Figure 1.1: (Top) open pond raceways and (bottom) closed photobioreactors.

Many of the economic challenges faced by large scale cultivation stem from energetic challenges in operating open ponds and bioreactors. Beal *et al.* estimated that the energy return on investment (EROI) for biodiesel produced in these cultivation systems ranged from 0.001 to 0.22, meaning that the energy required to produce the fuel was between 5 and 1000 times as large as the energy contained in the fuel itself [10].

Much of the energy required for cultivation is a direct result of the dilute nature of the culture. For a typical biomass concentration of 1 g/l, harvesting 1 kilogram of biomass necessitates processing 1,000 liters of water, which is an energy intensive process [10, 21]. Beal *et al.* estimated that even

for an efficiently operated closed photobioreactor system, mixing the culture would require 12.2 kJ per liter of processed culture volume, representing 38% of the overall cultivation and processing energy input requirement [10]. Assuming a microorganism concentration of 1 g/l and a heating value of 22 kJ/g for dry algal biomass, this mixing energy represents approximately 55% of the chemical energy contained in the algal biomass output. Moreover, dilute cultures require large energy inputs for concentrating and dewatering the resultant biomass. Gudin and Thepenier estimated that concentrating the biomass from the working concentration to a concentration at which lipids can be extracted accounts for 20 to 30% of the total biofuel production cost [48].

Open ponds also suffer from low illuminated surface area to volume ratios, resulting in inefficient light utilization [58, 91]. Under full sunlight, cells near the illuminated surface can become photoinhibited, a condition in which excessive irradiance damages the photosynthetic machinery and decreases the photosynthetic rate [19, 85]. On the other hand, cells nearer the bottom surface of the culture suffer from low photosynthetic rate due to shading by the cells above them. The number of cells exposed to the optimal irradiance for photosynthesis is relatively low. Closed photobioreactors have generally higher illuminated surface area to volume ratios, enhancing light delivery to the cells. However, this increased surface ara to volume comes at the expense of increased required pumping power, which can be 13 to 500 times larger for closed photobioreactors than for open ponds [58].

Moreover, open ponds lose water to the environment by evaporation.

8

This serves to keep the pond cool but comes at the expense of water that must be replaced, typically at a rate of about 5 L/m²-d [51, 93]. Closed photobioreactors do not lose water by evaporation, and as a result an active cooling mechanism must be employed.

1.3   The synthetic tree concept

Trees can be thought of as photobioreactors with significantly lower water contents and higher illuminated surface area to volume ratios than open ponds and closed photobioreactors. The water content of trees varies across species and environmental conditions, but on average a tree contains about 0.3 liters of water per kilogram of biomass, compared to 999 and 990 liters of water per kilogram of biomass in open ponds and photobioreactors, respectively [37]. Furthermore, trees use the process of transpiration to deliver water and nutrients to photosynthetic cells, thus eliminating the need for active mechanical pumping and agitation [77, 133]. As water evaporates from the stomata of leaves, the cohesive property of water brings nutrient-rich water from the soil, through the xylem, to the leaves [77]. In the leaves, photosynthetic cells fix carbon dioxide into sugars, which are then transported back to the plant via the phloem for utilization. Unlike the xylem, which contains dead cells and uses no energy, the phloem consists of living, dynamic cells that use molecular pumps to actively transport sugars to the non-photosynthetic regions of the plant. The phloem's interconnection between photosynthetic cells that generate chemical energy and non-photosynthetic cells that consume it allows

sugars to be transported out of photosynthetic cells at rates equal to the rates at which they are generated. This elegant strategy is significantly more energy positive than the process of extracting bioproducts in commercial algae operations, in which the cells must be lysed thus killing them and requiring regrowth.

Plants also utilize transpiration as an evaporative cooling mechanism. Nagler *et al.* showed that over the span of an August week in Tuscon, AZ, USA, a culture of cottonwood, willow, and saltcedar trees maintained their leaf temperatures an average of 2.1^oC cooler than the surrounding air by transpiring at an average rate of 2.1 liters per square meter of leaf area per day [95]. On average, trees feature leaf area indices (LAI) of 10 m^2 leaf area per m^2 ground cover, so the average evaporative loss per square meter of ground cover was closer to 21 $L/m^2/day$. Thus, trees benefit from the high illuminated surface area to volume ratio of closed photobioreactors while also benefiting from the evaporative cooling of open pond raceways. Moreover, the transpiration process that provides the cooling doubles as the nutrient delivery mechanism.

The synthetic leaf photobioreactor is a novel system that utilizes a modified transpiration mechanism to deliver water and nutrients to and harvest products from algal cells. Figure 1.2 shows the mechanism of operation in which a benthic microorganism culture grows on a porous substrate.

The uppermost section of the porous substrate does not support biofilm growth and is exposed to relatively drier air than is the biofilm-supporting substrate. Evaporation from this uppermost section drives liquid flow through the

10
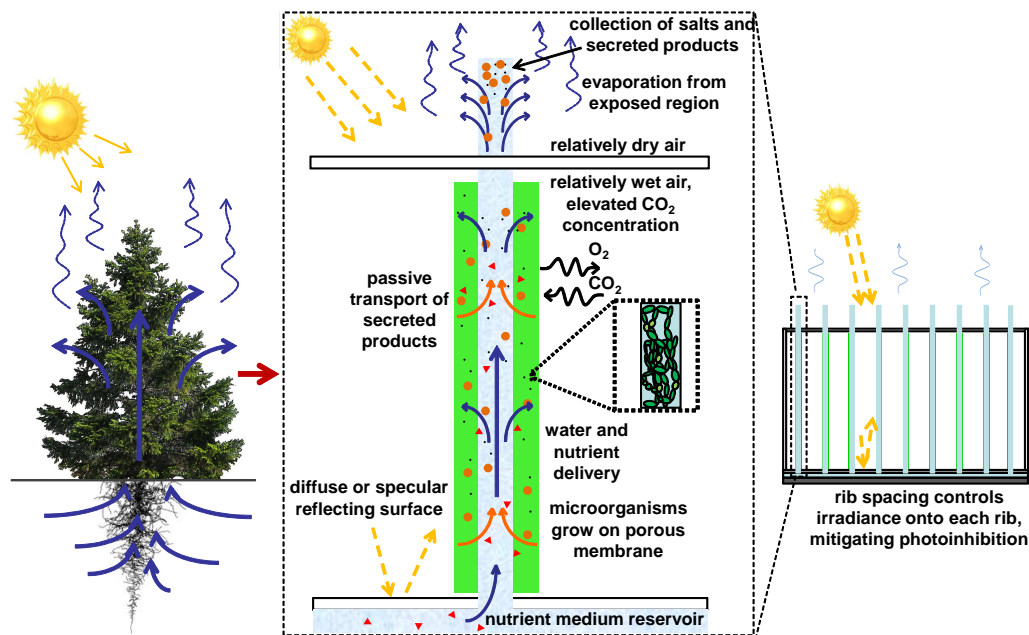
Figure 1.2: The synthetic leaf concept.

substrate and also serves as a collection area for salts and secreted products. Thus, in contrast to natural trees, in which nutrients flow from the soil to the leaves and secreted products flow back toward the roots, in the synthetic leaf system, secreted products flow toward the terminal end where they can be extracted for use rather than reinvested into the vascular system. The terminal evaporation region also collects salts from the nutrient medium, which can later be extracted and reused. Moreover, as shown in the right panel of Figure 1.2, a scaled up leaf system utilizes multiple vertical units, thereby increasing the specific surface area of the reactor, enhancing both light utilization and gas transfer. This novel concept of cultivating photosynthetic microorganisms and harvesting their secreted products provides the platform necessary for shifting

11

the paradigm from biomass harvesting and product extraction to using these microbial cells as true biochemical factories or biocatalysts for ultra-passive, energy-positive biofuel generation.

1.4 Organization of the dissertation

This dissertation describes the design, construction, performance, modeling, and optimization of a synthetic leaf for sustainable biofuel production. Chapter 2 presents the results from the operation of a scaled down prototype cultivating the cyanobacteria *Anabaena variabilis*, and identifies challenges and opportunities for scale up. One of the challenges for scale up was the imbalance in the photon flux and nutrient flux to photosynthetic cells in the synthetic leaf environment. This challenge is tackled in Chapter 3, which is a modeling study aimed at balancing the fluxes of photons, dissolved gases, and dissolved nutrients in the synthetic leaf. Moreover, Chapter 4 aims to model the nutrient medium flow within the synthetic leaf vascular transport network as a function of mechanical properties of the leaf itself as well as environmental parameters.

Another challenge in operating and characterizing the synthetic leaf system lied in real time productivity monitoring. Chapter 5 presents a novel, non invasive, real time biomass quantification method using three band spectral imaging with a simple RGB digital camera. This method can be used for measuring the biomass concentration in the synthetic leaf as a function of both time and space. This method was employed for the study presented in Chap-

ter 6, the goal of which is to experimentally characterize the performance of synthetic leaves from the perspective of nutrient delivery, growth, microorganism health, and product secretion. Finally, Chapter 7 summarizes the benefits and limitations of the synthetic leaf platform, and offers recommendations for research moving forward.

Chapter 2

Operation of a scaled-down Surface-Adhering Bioreactor

2.1   Introduction

A Surface-Adhering Bioreactor (SABR) was constructed and operated to demonstrate its ability to host microorganism growth. A conventional planktonic photobioreactor was also operated as a performance comparison. The SABR prototype required 4% the working volume of water as the planktonic prototype. Moreover, SABR required no mixing power, whereas the mixing power requirement of the planktonic photobioreactor was equal to about 12% of the incident radiant power. The SABR showed local growth rates as great as four times that of the planktonic prototype. However, the growth rate within the SABR was highly non-uniform, and low growth in certain regions is attributed to light and nutrient limitation. Strategies for improving nutrient and light delivery were identified.

2.2   Materials and Methods

Figure 2.1 shows the SABR prototype alongside the conventional planktonic photobioreactor prototype. Each prototype was 10 cm long, 6.5 cm wide,

and 8 cm tall. The SABR prototype consisted of 10 vertical porous cellulose ribs that supported microorganism growth. The ribs had a thickness 320 μm with porosity 0.87 and average pore diameter of about 2 μm. The base of each rib rested in a 1.5 mm hydraulic diameter channel at the bottom of the device which contained the BG11 nutrient medium [124]. Carbon dioxide-enriched air (0.8 $\pm$ 0.1 %vol CO_2) was delivered into the SABR through the manifold on the side at a rate of 35 ml/min, while it was delivered at the same rate into the headspace of the planktonic photobioreactor prototype. Each prototype was placed under a cool white fluorescent light bulb, and the incident irradiance onto the top horizontal surface of each prototype was 16 $\pm$ 2 W/m^2 in the photosynthetically active region (PAR). A magnetic stirbar was used to enhance mixing in the planktonic prototype. Each prototype was inoculated with 40 mg of the cyanobacteria *Anabaena variabilis* (ATCC 29413-U). This species was used as an exemplary photosynthetic microorganism due to its nitrogen fixation capability and its widespread use in experimental studies on photobiological CO_2 mitigation and H_2 production [14, 47, 106, 131].

Chlorophyll content was measured as a proxy for biomass concentration, and was measured upon initial inoculation of the bioreactors and after 158 hours of operation. For the planktonic photobioreactor prototype, 10 ml of culture volume was centrifuged at 3,000 RPM for five minutes. The supernatant was discarded, and 10 ml of 95% ethanol was added to the concentrated slurry. The ethanol solution was shaken manually and left in the dark for one hour. The resulting solution was then centrifuged at 3,000 RPM for two min-
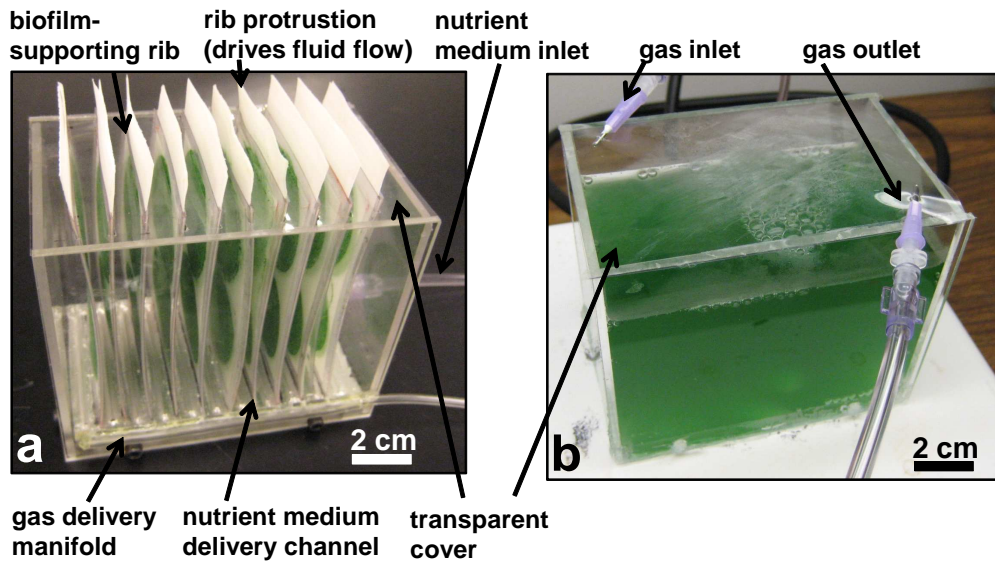
Figure 2.1: (a) Surface-Adhering Bioreactor (SABR) prototype and (b) planktonic photobioreactor prototype.

utes. The absorbance of the ethanol phase was then measured at 649 nm (A_{649}) and 665 nm (A_{665}) in a Genesys-20 spectrophotometer (Thermo). The chlorophyll concentration in μg/ml was then calculated as, $[Chl] = 6.10\ A_{665} + 20.0\ A_{649}$ [3]. For the SABR prototype, the chlorophyll content of the outside top, outside bottom, inside top, and inside bottom regions of the outermost rib were measured. Each rib section was removed from the SABR and left in 10 ml of 95% ethanol in the dark for one hour. The resulting solution was analyzed in the same way as the PP prototype solution.

2.3 Results and Discussion

2.3.1 Water and energy requirements

The working water volume in SABR was calculated by adding the water content of the microchannels in the base to the water content in the ribs. The working water requirement of SABR was 16 ml. By comparison, the planktonic prototype required 400 ml of water. Thus, SABR offered a 96% decrease in working water requirement. This reduction in water volume is advantageous in many applications, including life support of humans in space, in which system mass must be minimized due to fuel requirements. The reduction in working water mass also reduced the power required for bioreactor mixing. For the SABR prototype, no mixing energy was required, whereas the planktonic prototype required power for rotating the magnetic stirrer to keep the reactor well mixed. The power required to rotate the stir bar was estimated by dividing the stir bar into infinitesimal lengths and estimating each length as a cylinder in cross flow.[1] The power required to mix the culture was estimated to be 16 mW. By comparison, the irradiant power onto the top surface of the culture

---

[1]Each section had a length dx and distance from the axis of rotation x. The drag force on a given section $F_{D,dx}$ is given by $F_{D,dx} = 1/2 C_D \rho A v^2$, where C_D is the drag coefficient, ρ is the mass density of the culture, and v is the local free stream velocity over the section, given by $v = x\omega$, where ω is the angular velocity of the stirbar. The frontal area of the section A is equal to $2rdx$, where r is the stirbar radius. The torque applied by the section on the axis of rotation is then given by $\tau_{dx} = x F_{D,dx}$. The power required to move the section is the product of the torque and the angular velocity. Integrating over the length of the bar, the power required to move the bar P is given by $P = 1/4 \rho C_D \omega^3 r l^4$. The values for ρ, r, and l were 1000 kg/m^3, 0.006 m, and 0.038 m, respectively. The angular velocity ω was 16 rad/s, which corresponds to the set rotation speed of 150 RPM. The drag coefficient was estimated as 1.2, corresponding to an average Reynolds number for flow over the bar of 2400 [134].

was 130 mW. Therefore, the power required to mix the reactor corresponded to about 12% of the irradiant energy incident onto the reactor. As SABR does not require this mixing energy, it potentially has a greater energy return on investment than planktonic bioreactors.

2.3.2   Growth in each prototype

Figure 2.2 shows the chlorophyll increase after 158 hours of operation in the outward facing top, outward facing bottom, inward facing top, and inward facing bottom regions of the outermost SABR rib, as well as the chlorophyll increase in the planktonic photobioreactor. The outward-facing bottom rib section had a chlorophyll increase approximately four times that of the planktonic prototype. The outward facing top and inward facing top samples had chlorophyll increases less than that of the planktonic prototype, and no appreciable chlorophyll increase was observed in the inward facing bottom sample. The increased productivity of the outward facing bottom sample compared to the outward facing top sample was attributed to nutrient limitation. Nutrient medium was fed from the bottom delivery channel upward, so nutrients were consumed along the medium's flow path and the nutrient medium at the top of the rib was less nutrient-rich than the medium at the bottom.

This nutrient limitation presents a challenge for scale-up. A scalable SABR must be capable of providing fresh nutrient medium to microorganisms at locations far from the nutrient medium reservoir. We envision larger SABRs incorporating microchannel networks designed to feed fresh nutrient medium
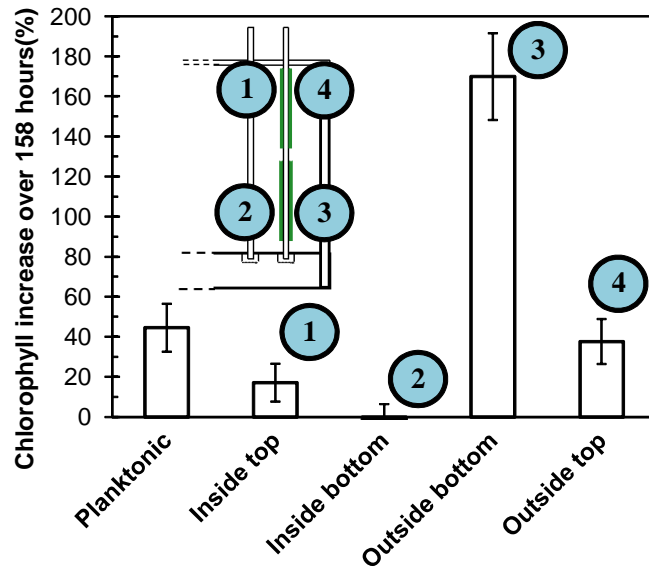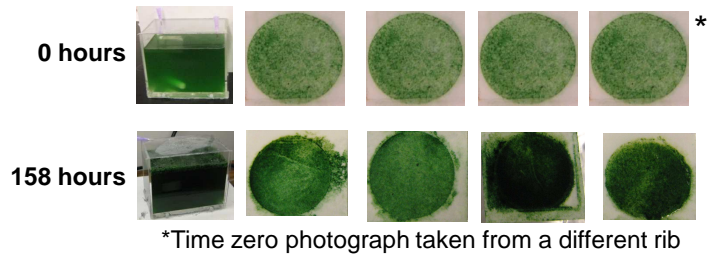
Figure 2.2: Increase in chlorophyll content for four regions of the SABR prototype as well as for the planktonic photobioreactor prototype.

to the biofilm-supporting porous medium at multiple locations, rather than at a single location. Such a strategy enables microorganism productivity at large physical distances from the reservoir, analogous to photosynthesis occurring in the mesophyll cells of redwood trees 100 m above the roots. The consequent challenge will be in designing a microcapillary network capable of overcoming the pressure drop caused by friction from the microchannel walls and transporting the fluid against gravity. Wheeler and Stroock have provided insight

on the design of such synthetic xylems [133]. The authors etched microchannels into a hydrophilic hydrogel substrate and induced flow through them by evaporation from a synthetic leaf membrane, simulating transpiration. They demonstrated that evaporation from the leaf membrane was capable of pulling water through microchannel pressure drops of up to 1 MPa. Optimally designing the vascular nutrient medium delivery structure to address both the mechanical limitations of the flow network as well as the biological requirements pertaining to nutrient depletion will be a key challenge for designing scaled up systems.

Furthermore, in the SABR prototype, light limitation was the principal reason for the lower productivity of the inside bottom sample compared to the inside top sample. The view factor between the bottom rib region and the light source was smaller than that between the top region and the light source. In optimized designs, light incident onto the top horizontal surface of SABR can be evenly distributed onto the ribs through strategic design of the bottom reflecting boom, as shown conceptually in Figure 2.3. The inset of the figure shows how a normally incident beam with irradiance G_1 and cross sectional area A_1 is reflected onto the rib area A_2 using a specular reflector. The irradiance onto the rib, G_2, is then equal to $G_1(A_1/A_2)$. In this way, rib spacing is a mechanism for controlling the irradiance onto each rib, thus mitigating the phenomenon of photoinhibition in which excessive irradiance damages cells [19, 116]. Interestingly, trees also employ this strategy. It was shown by Nagler *et al.* that the average leaf area index, defined as the ratio of

leaf area to ground cover area, of a sample of cottonwood, willow, and saltcedar trees was about 8.5. Assuming that the sun is directly overhead and provides a collimated irradiance of 1,000 W/m^2, the average irradiance onto each leaf is about 110 W/m^2, which corresponds, approximately, to the irradiance for maximum photosynthetic productivity for many species [39, 130].
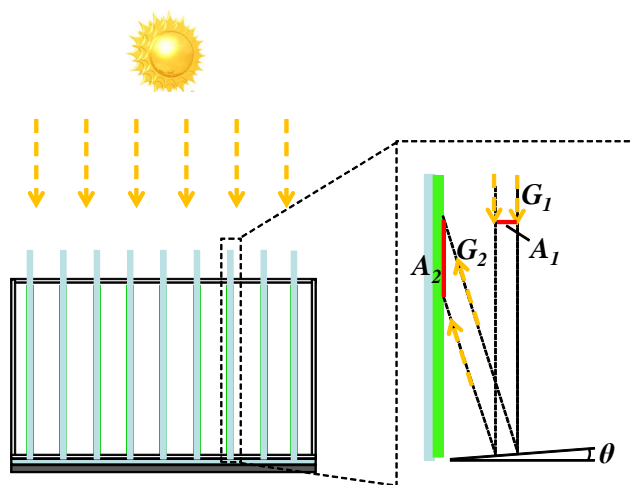
Figure 2.3: Optimal angle of bottom reflecting boom θ redirects the incident irradiance onto the rib, thus reducing the irradiance onto the rib to a level that corresponds to maximum photosynthetic productivity.

2.3.3   Toward a product-harvesting synthetic tree

The photosynthetic cells of vascular plants secrete organic compounds, predominantly sugars, which are transported via the phloem to non-photosynthetic cells for storage or utilization [77]. The goal of a product-harvesting SABR is to (i) cultivate cells that secrete neutral lipids or other biofuel feedstocks, rather than carbohydrates, and (ii) extract those compounds passively. Thus,

21

SABR can be conceptualized as a tree whose roots, trunk, and branches are abiotic and do not require maintenance energy. Thus, chemical energy surplusses from the leaves can all be extracted for utilization.

Photosynthetic microorganisms that secrete energy-dense molecules for biofuel production have been demonstrated [110, 138, 139]. The aforementioned studies utilize two distinct strategies to extract energy-dense molecules from algae. Reppas and Ridley of *Joule Unlimited* patented a microorganism that has been genetically modified to secrete ethanol [110]. The organism can be induced to switch from growth mode to product formation mode by altering the composition of the nutrient medium surrounding the cells. Alternatively, Zhang *et al.* have demonstrated the feasibility of milking lipids from naturally occurring algae strains using non-lethal solvents. They showed that adding 10% v/v tetradecane to a culture of the green algae *Botryococcus braunii* weakens the cell membrane to enable *in situ* lipid extraction without sacrificing the health of the cells [138]. They also determined that using 10% v/v hexadecane can be used for non-lethal lipid milking from *Nannochloropsis* sp. [139].

Once secreted, SABR provides a method for passive concentration of bioproducts as particles carried by the liquid phase collect in terminal evaporation regions. To experimentally demonstrate SABR's capability to harvest secreted products, we constructed a model abiotic single rib, which consisted of a strip of cellulose filter paper with an average pore diameter of 5 to 10 μm and a length and width of approximately 5 cm and 0.5 cm, respectively

(Figure 2.4). One end of the rib was placed in contact with a water-palm oil emulsion with an oil volume fraction of approximately 10% (Figure 2.4b)[2]. The other end of the rib, which served as the lipid-concentrating region, was exposed to air with a temperature and relative humidity of 21 ± 1 ^{o}C and 60 ± 5%, respectively. The rib region between the two ends was exposed to air that was nearly saturated with water vapor. Figure 2.4c shows that the lipid concentrating region became yellow and translucent, indicative of concentration of palm oil in that region. Compared to planktonic photobioreactors, the harvesting of whose bioproducts requires concentration and lysing of the cells, the SABR demonstrates a passive, evaporation-driven mechanism to bypass both of these energy-intensive processes.

For efficient generation of bioproducts, it is desirable to grow the SABR biofilm to a steady state thickness, and subsequently use the existing cells as biocatalysts, while preventing further biomass accumulation. This strategy increases bioproduct generation efficiency as incident solar energy is diverted into product formation, rather than cell division. Moreover, generation of algal biomass requires the consumption of of a given element by an amount dictated by the element's mass fraction in the biomass. Therefore, preventing excessive biomass accumulation diminishes the input requirement of elements of limited

---

[2]Palm oil (mixture of glyceryl laurate, myristate, palmitate, stearate, oleate, linoleate, and alpha-linolenate [29]) was centrifuged at 3,000 RPM for 20 minutes to remove particulates. The oil was then added at an approximate volume fraction of 5% to deionized water. The emulsion was generated by placing the mixture in a sonicator (Fisher, Sonic Dismembrator 550) for two minutes at 30% power. The resulting emulsion was then filtered through filter paper with an average particle retention size of 5-10 μm (Fisher, P5) to remove the larger oil droplets.
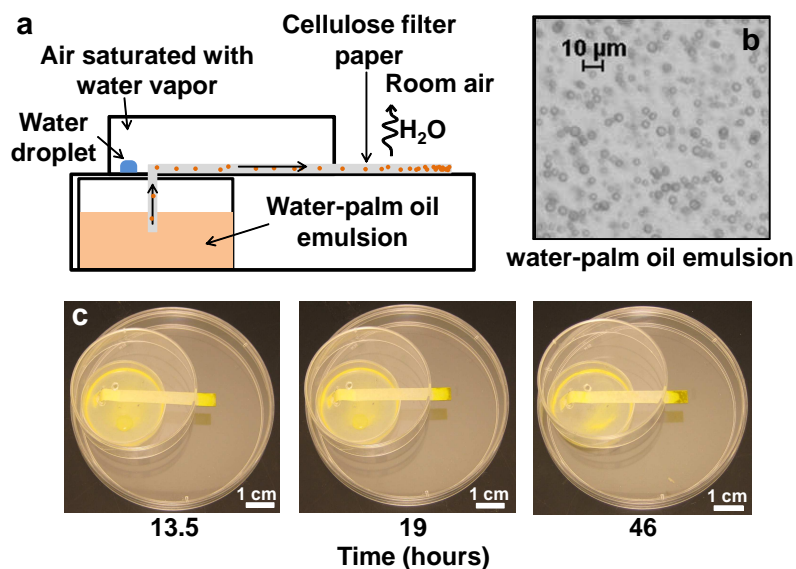
Figure 2.4: (a) Schematic of the single rib platform used to demonstrate lipid-concentrating capability. (b) Micrograph of the water-palm oil emulsion transported through the rib. (c) Lipid concentration near the terminal end of the exposed region of the rib.

resource such as phosphorus or nutrients of high embedded energy such as nitrogen. Finally, maintaining the biofilm at a steady state thickness can mitigate nutrient-limited metabolism of cells by limiting the distance across which nutrients must travel.

Microorganisms in the SABR can be induced to switch from growth mode to bioproduct formation mode by temporally varying the composition of the nutrient medium. The rate of delivery of this nutrient medium to the cells is controlled by the evaporative flux from the exposed region. By tuning the rate of delivery of a given nutrient to the rate of its utilization by the cell, no energy is wasted in moving the nutrient medium.

24

2.4 Conclusions

Here we have presented a novel Surface-Adhering Bioreactor (SABR) for microorganism cultivation and bioproduct harvesting. The technology utilizes a simulated transpiration mechanism to deliver nutrients and water to cells and harvest secreted products without the need for auxiliary energy inputs for culture pumping and mixing. A scaled-down SABR prototype was constructed and operated alongside a similarly sized planktonic photobioreactor prototype. The working water volume required of the SABR prototype was 25 times less than that of the planktonic photobioreactor prototype. Moreover, the SABR required no auxiliary energy for pumping or mixing, whereas culture mixing for the plankotnic photobioreactor prototype required an amount of power that corresponded to about 12% of the irradiant power onto the prototype. Furthermore, although the local growth rate of *Anabaena variabilis* was highly variable within SABR, the growth rate at locations with favorable nutrient and light delivery attained productivities as large as four times that of a comaparable planktonic system.

Chapter 3

Flux balancing of light and nutrients in a biofilm photobioreactor for maximizing photosynthetic productivity

3.1 Introduction

Algae cultivation has a wide variety of applications, including but not limited to wastewater remediation, production of food supplements, high value chemicals, and biofuels, as well as life support of humans in space [26, 36, 67, 93, 108]. Traditionally, algae has been cultivated in open ponds or closed photobioreactors, both of which employ suspended cell culturing [21, 121]. Suspended culturing suffers from several drawbacks, including requirements for large working water volume and large energy inputs for pumping and mixing the culture, as well as dewatering and concentrating the biomass during harvesting [9, 28].

In light of these challenges, biofilm photobioreactors have been proposed in which algae are cultivated attached to a solid surface rather than in suspension [69, 101, 120]. The large microorganism densities characteristic of such photobioreactors significantly reduce the working water volume and associated energy input requirements [101]. However, a flowing liquid layer is

still required adjacent to the biofilm to keep the cells hydrated and provide nutrients, which limits the potential for reducing the water and energy input.

Recently, a subclass of biofilm photobioreactors has been presented wherein algae are cultivated as a biofilm attached to a porous substrate which delivers water and nutrients to the microorganisms [71, 93, 97]. Such systems, here referenced as porous substrate bioreactors (PSBRs), further reduce the water and energy input requirements for cultivation. Moreover, having an array of vertical units in a given volume enhances the illuminated surface area to volume ratio of the photobioreactor system, which has been shown to enhance productivity [58]. Moreover, gas transfer is also enhanced in PSBRs compared to other cultivation systems due to (i) the increased surface area to volume ratio and (ii) the microorganisms being in direct contact with the gas phase.

However, PSBRs introduce a new set of engineering challenges. For example, nutrient delivery to the cells is accomplished by diffusion, rather than advection, which motivates the concern that growth in these systems could be diffusion-limited. An optimally designed system is one that delivers nutrients to the cells at the rate at which the cells would consume them based on the local photon availability. This strategy enables maximum photon utilization by avoiding nutrient limited and nutrient inhibited growth. Thus, it is first necessary to understand the transport of light and mass in the bioreactor in relation to the growth kinetics.

This study addresses this need and reports a comprehensive model in-

27

tegrating light transport, mass transport, and growth kinetics in a general PSBR setting. The model provides insight into transport phenomena in photosynthetic biofilm systems and enables maximization of the overall biofilm productivity by balancing the fluxes of dissolved nutrients and photons to the cells.

3.2 Current State of Knowledge

3.2.1 Porous substrate bioreactor (PSBR) technology

Naumann *et al.* cultivated a variety of green algae and diatom strains on a Twin-Layer Photobioreactor (TLP) for generation of aquaculture feed [97]. The TLP consisted of multiple vertical planar units. Each vertical unit consisted of a non-woven glass fiber inner layer and outer paper layers, which hosted microbial growth, on either side of the inner layer. The pore size of the paper was small enough that the microorganisms could not cross into the inner layer, but large enough to enable nutrient diffusion. A pump was used to circulate nutrient medium through the inner layer, and water and nutrients were delivered to the cells by wicking and diffusion. A combination of solar light and sodium discharge lamps was used to provide the cells with a 15h/9h light/dark cycle, where the average irradiance during the light period was 67 $\mu E/m^2$-s. The authors reported growth rates for *Phaeodactylum tricornutum*, *Tetraselmis suecica*, *Nannochloropsis* sp., and *Isochrysis* sp. of 1.8, 1.5, 0.8, and 0.6 grams of biomass per square meter of biofilm area per day, respectively.

Moreover, Liu *et al.* reported a similar system in which microalgae were

cultivated on vertical sheets of filter paper, each supported by a solid glass pane [71]. A drip system was used to deliver nutrient medium into the filter paper from the top. The authors constructed multiple parallel vertical panes and defined the light dilution ratio as the ratio of the substrate surface area to the footprint area of the reactor. Using a light dilution ratio of 10 under outdoor solar lighting, the average biomass productivity over a cultivation period of eight days was 65 grams of *Scenedesmus obliquus* per square meter of footprint area per day.

Finally, Murphy *et al.* constructed and operated a Surface-Adhering Bioreactor (SABR) to cultivate the cyanobacteria *Anabaena variabilis* [93]. The reactor consisted of ten vertical porous ribs that hosted cyanobacterial growth on each side. The bottom of each rib was immersed in a nutrient medium flow channel. The top region of the rib was exposed to ambient air, and evaporation from this region drove the flow of nutrient medium through the rib, mimicking the transpirative operation of a tree. Therefore, in contrast to the aforementioned attached photobioreactors, the SABR did not require an active pump for operation. The top horizontal surface of the reactor was subjected to an irradiance of 74 ± 9 $\mu E/m^2$-s using cool white fluorescent bulbs for a cultivation period of 21 days, during which the cyanobacterial growth rate was approximately 0.5 grams per square meter of footprint area per day.

3.2.2 Biofilm modeling

A vast body of research exists on modeling the formation, growth, metabolic rates, and death of non-photosynthetic biofilms [66, 98, 132]. Such modeling studies have predominantly been motivated by (i) design and optimization of engineered biofilm systems, such as wastewater bioreactors, and (ii) eliminating undesirable biofilms, which can cause infectious diseases, increase drag on the hulls of ships, decrease heat transfer rates through pipes, and corrode metals [132]. Modeling of PSBRs presents two unique challenges compared to previously reported modeling efforts. First, the previously reported biofilm models consider the biofilm at the interface of a bulk liquid layer and an impermeable solid substratum [132], whereas in PSBRs the biofilm is at the interface of a porous substratum and the gas phase [71, 93, 97]. Second, most previous studies have focused on non-photosynthetic biofilms in which light availability to cells is not a parameter.

More recent studies have presented models of photosynthetic biofilms in photobioreactors for hydrogen production [68, 137]. Liao *et al.* modeled photosynthetic biofilm growth on a solid surface in a flat panel photobioreactor using the lattice Boltzmann method [68]. The authors employed a two-dimensional model that took into account diffusion, consumption, and production, and modeled growth using the cellular automata method [104]. The authors investigated the effects of initial inoculation concentration, light intensity, and pH on biofilm growth rate. However, their model assumed uniform light intensity within the biofilm, which is not a realistic assumption as light attenuates ex-

ponentially over the thickness of the biofilm, giving rise to significant intensity gradients [91].

The current study reports, for the first time, a comprehensive PSBR model integrating light and mass transport from first principles with semi-empirical models for growth kinetics. The model provides insight into the local fluxes of photons, nutrients, and inhibitory metabolites such as oxygen within the biofilm and their influence on cellular growth kinetics. Thus, the model can be used to design PSBRs that deliver photons and nutrients to cells at optimal rates maximizing productivity and nutrient utilization.

3.3   Analysis

Figure 3.1 shows the schematic of the PSBR modeled in this study. In this system a biofilm of thickness L_b is cultivated on a porous substrate of thickness L_p. The length of the system is l, which was equal to 2.5 cm in this study due to relative ease of constructing such a system experimentally. The nutrient medium flows in the the porous medium with superficial velocity u_p and can be driven by gravity, evaporation, or a pump. The chemical potential difference of species i between the porous medium and the biofilm drives the transport of nutrients to the cells. The photosynthetic biofilm is in direct contact with the gas phase at temperature T and pressure p, containing water vapor, carbon dioxide, and oxygen at partial pressures p_{H_2O}, p_{CO_2}, and p_{O_2}, respectively. The biofilm is illuminated with uniform diffuse spectral irradiance $G_{\lambda,in}$ as shown. The spatial coordinates x and y signify the distances

31

from the origin in the in-plane and out-of-plane directions, respectively. The biofilm thickness and microorganism concentration were treated as constants for the duration of the simulation times as the time scale for photoautotrophic growth was much greater than the time scales for light and mass transport. For all simulations, it was assumed that the biomass concentration X was spatially homogeneous and equal to 100 kilograms dry weight per cubic meter (kg DW/m^3) [101].
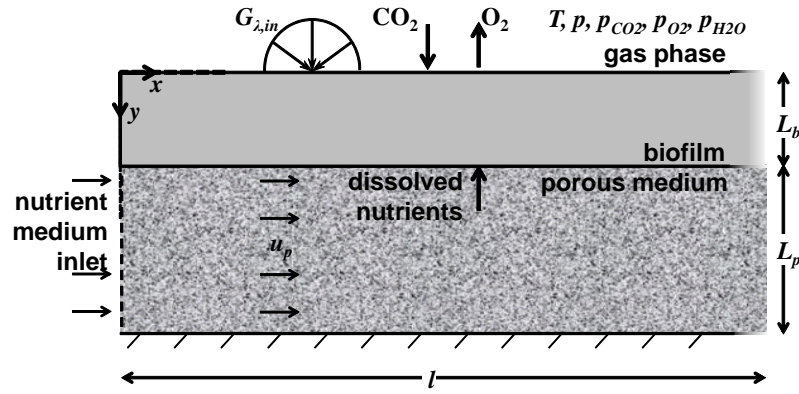
Figure 3.1: Schematic of the PSBR.

3.3.1 Light transport model

3.3.1.1 Assumptions

In order to make light transport in the biofilm mathematically tractable, it was assumed that: (1) light transport was one-dimensional and steady with respect to mass transport, (2) the medium surrounding the cells in the biofilm was non-emitting, weakly absorbing, and non-scattering in the photosynthetically active region (PAR) of the spectrum, and (3) independent scattering

32

dominated over dependent scattering for the cell size parameters and volume fractions considered [118].

3.3.1.2 Governing equations

The local light availability is governed by the radiative transport equation (RTE). The one dimensional, spectral, steady-state RTE can be written as [118],

$$\frac{\partial I_\lambda(y,\hat{s})}{\partial y} = -\kappa_{eff,\lambda}I_\lambda(y,\hat{s}) - \sigma_{eff,\lambda}I_\lambda(y,\hat{s}) + \frac{\sigma_{eff,\lambda}}{4\pi}\int_{4\pi}I_\lambda(y,\hat{s}_i)\Phi_\lambda(\hat{s}_i,\hat{s})d\Omega_i$$

(3.1)

where $I_\lambda(y,\hat{s})$ is the spectral radiant intensity at location y traveling in the direction $\hat{s}$, expressed in W/m^2-nm-sr. The parameters $\kappa_{eff,\lambda}$ and $\sigma_{eff,\lambda}$ are the effective absorption and scattering coefficients of the biofilm in m^{-1}, and can be written as,

$$\kappa_{eff,\lambda} = \kappa_{m,\lambda}(1 - \nu X) + A_{abs,\lambda}X$$

(3.2)

$$\sigma_{eff,\lambda} = S_{sca,\lambda}X$$

(3.3)

where X is the microorganism concentration and $\kappa_{m,\lambda}$ is the absorption coefficient of the medium surrounding the cells, which was assumed to be equal to that of water. The spectral absorption coefficients of water can be written as [15],

$$\kappa_{m,\lambda} = \frac{4\pi k_\lambda}{\lambda}$$

(3.4)

where k_λ is the absorption index of water reported by Hale and Querry [52]. In Equation (3.2), the parameter ν is the specific volume of the microorganisms,

33

assumed to be equal to 0.001 m^3/kg [15]. The mass absorption and scattering cross sections, A_{abs} and S_{sca}, respectively, are both expressed in m^2/kg and were reported by Berberoglu and Pilon [16].

Moreover, in Equation (3.1), Φ_λ is the scattering phase function, which is the probability that radiation traveling in the solid angle $d\Omega_i$ around the direction $\hat{s}_i$ will be scattered into the solid angle $d\Omega$ around direction $\hat{s}$. The integral term in Equation (3.1) accounts for the multiple scattering phenomena in a dense culture. The photosynthetically active irradiance, G_{PAR}, was defined as [118],

$$G_{PAR}(y) = \int_{400 \text{ nm}}^{700 \text{ nm}} \int_{4\pi} I_\lambda(y, \hat{s}) d\Omega d\lambda \qquad (3.5)$$

Finally, the optical thickness has been shown to be an appropriate parameter for scaling light availability in algae cultivation systems [91]. The local optical thickness τ is the product of mass extinction coefficient, E_{ext}, the volumetric biomass concentration, X, and the physical distance from the light facing surface, y. The mass extinction cross section in the photosynthetically active region was reported to be 355 m^2/kg for *A. variabilis* [15].

3.3.1.3 Boundary conditions

The biofilm was illuminated with diffuse solar lighting, the spectral content of which was reported by Gueymard *et al.* at 10 nm resolution [49].

34

The boundary conditions for light intensity in the biofilm can be written as,

$$I_\lambda(y = 0, \theta) = (1 - r_b)G_{\lambda,in}/\pi \quad \text{for} \quad 0 \leq \theta \leq \pi/2$$

$$I_\lambda(y = L_b, \theta) = r_p G_\lambda^+(y = L_b)/\pi \quad \text{for} \quad \pi/2 \leq \theta \leq \pi \qquad (3.6)$$

where θ is the zenith angle with respect to the normal into the biofilm. The parameter G_λ^+ is the spectral irradiance at the biofilm-porous medium interface in the direction into the porous medium. The parameters r_b and r_p represent the hemispherical-hemispherical reflectances of the biofilm and porous medium, and were equal to 0.04 and 0.5, respectively, in the PAR [60].

3.3.1.4 Solution method and grid size independence

The RTE was solved numerically using the discrete ordinates method with a combination of two Gauss quadrature having 24 discrete directions per hemisphere along with the associated weighting factors successsfully used by Baillis *et al.* for strongly forward media [6, 16]. Convergence studies were performed to ensure that the computed values of $G_\lambda(y)$ were independent of both the grid size and the angular discretization. To do so, the number of grid points was doubled until the relative discrepancy between $G_\lambda(y)$ obtained for two consecutive grid refinements did not change by more than 1%. It was found that 240 points along the y-direction satisfied this criterion. Moreover, the values of $G_\lambda(y)$ did not vary by more than 0.6% as the number of directions per hemisphere was increased from 24 to 30 [16].

3.3.2 Mass transport model

3.3.2.1 Assumptions

To facilitate modeling of mass transport in the system, it was assumed that (1) advection in the out-of-plane direction was negligible in the biofilm and porous medium as the gas phase adjacent to the biofilm was saturated with water vapor, (2) the in-plane velocity, and hence in-plane advective transport in the biofilm was negligible, (3) the temperature, pressure, and partial pressures of CO_2, O_2, and H_2O in the gas phase were actively maintained at constant values, and (4) the pH was uniform across the thickness of the biofilm. Indeed, pH gradients in the out-of-plane direction in photosynthetic biomats generally do not exceed 1.8×10^{-3} pH units per micrometer [2, 96, 111].

3.3.2.2 Governing equations

With these assumptions, the equation governing the concentration of nutrient i in the porous medium, denoted as $[i]$, can be written as [83],

$$\frac{\partial [i]}{\partial t} = D_{i,p}\frac{\partial^2 [i]}{\partial y^2} + D_{i,p}\frac{\partial^2 [i]}{\partial x^2} - \frac{\partial}{\partial x}([i]u_p) \qquad (3.7)$$

where $D_{i,p}$ is the diffusion coefficient of nutrient i in the porous medium. The left hand side of Equation (3.7) accounts for storage of nutrient i. The first two terms on the right hand side account for diffusion in the out-of-plane and in-plane directions, respectively, and the third term accounts for advection in the in-plane direction.

Similarly, the governing equation for mass transport in the biofilm can

be written as [83],

$$\frac{\partial [i]}{\partial t} = D_{i,b}\frac{\partial^2 [i]}{\partial y^2} + D_{i,b}\frac{\partial^2 [i]}{\partial x^2} - \gamma_i \qquad (3.8)$$

where $D_{i,b}$ is the diffusive permeability of species i, which is the appropriate parameter governing transport of solutes that are produced or consumed in biofilms, such as nutrients and molecular oxygen [126]. The consumption term γ_i can be written as,

$$\gamma_i = \frac{\mu X}{Y_{X/i}} \qquad (3.9)$$

where μ is the local growth rate, expressed in s^{-1}, and X is the biomass concentration in kg/m^3. The parameter $Y_{X/i}$ is the biomass yield based on the amount of nutrient i consumed, expressed in kg biomass/kmol i [38].

3.3.2.3 Closure laws

Identification of growth-limiting nutrients

First, the nutrients whose availabilities were most likely to limit growth were identified. Table 3.1 compares the elemental compositions of 14 different cyanobacterial species to that of the nutrient medium BG11 [17, 54, 62, 63, 119, 124]. The table indicates that, from an elemental analysis perspective, cyanobacteria growing in BG11 will first exhaust the available phosphorous before exhausting any other macronutrient present therein. Moreover, it was evident that the micronutrients Fe, Mn, Zn, Mo, Cu, and Co would not be growth-limiting as BG11 is replete with these elements with respect to algal biomass composition [55]. Therefore, this study focused on the transport

37

of phosphate through the SABR to identify locations of phosphate-limited growth. Nitrate transport was also modeled to investigate possible circumstances of nitrate-limited growth. Moreover, inorganic carbon transport was also considered because it is delivered from the gas phase rather than from the porous medium and can be a limiting factor in high cell density systems [70]. Finally, molecular oxygen transport was also modeled to identify locations of oxygen inhibition [22, 76].

Table 3.1: Elemental composition of 14 cyanobacterial strains and BG11 nutrient medium with respect to phosphorous content.

| Cyanobacterium | mol/mol P | | | | | |
	N	P	K	Mg	S	Ca
Synechococcus (2 strains) [17]	29	1.0	–	–	–	–
Synechococcus (2 strains) [54]	14	1.0	–	–	–	–
Prochlorococcus (7 strains) [17, 54]	20	1.0	–	–	–	–
Anabaena flos-aquae [119]	–	1.0	0.89	0.34	0.20	0.19
Anabaena sp. [62]	–	1.0	1.03	0.23	0.44	0.66
Microcystis aeruginosa [63]	–	1.0	0.91	0.58	0.52	0.79
Average	**20**	**1.0**	**0.94**	**0.38**	**0.39**	**0.54**
Standard deviation	8.0	0.0	0.08	0.18	0.17	0.32
BG11 [124]	**77**	**1.0**	**2.00**	**1.33**	**1.33**	**1.07**

Growth kinetic model

The local growth rate μ was calculated using the Monod model taking into account limitation and inhibition for nutrients and irradiance, which can be written as [5],

$$\mu = \mu_{max} \left(\frac{G_{PAR}}{K_{S,G} + G_{PAR} + G_{PAR}^2/K_{I,G}} \right) \prod_i \frac{[i]}{K_{S,i} + [i] + [i]^2/K_{I,i}} \quad (3.10)$$

38

where μ_{max} is the maximum specific growth rate in s^{-1} and $K_{S,G}$ and $K_{I,G}$ are the half-saturation and inhibition constants for irradiance, respectively, expressed in W/m^2. The parameters $K_{S,i}$ and $K_{I,i}$ are the half-saturation and inhibition constants for nutrient i, given in mol/L.

Parameters for growth kinetics and biomass yield

Table 3.2 shows the half-saturation and inhibition constants $K_{S,i}$ and $K_{I,i}$ for each nutrient considered. The maximum specific growth rate μ_{max} was 4.2×10^{-5} s^{-1} and the half-saturation and inhibition constants for irradiance, $K_{S,G}$ and $K_{I,G}$ were 38 W/m^2 and 400 W/m^2, respectively [13, 73]. As molecular oxygen was not a nutrient but an inhibitor, it featured an inhibition constant but no half-saturation constant [76]. Table 3.2 also presents the biomass yields based on consumption of each nutrient, $Y_{X/i}$. These yields assume a cyanobacterial stoichiometry of C$_{159}$H$_{263}$O$_{63}$N$_{20}$P$_1$K$_{0.94}$Mg$_{0.38}$S$_{0.39}$Ca$_{0.54}$ [4, 17, 54, 62, 63, 119].

Table 3.2: Transport and modified Monod model parameters for the dominant species of inorganic carbon, nitrate, phosphate, and molecular oxygen, in the pH range of 7 to 10.

	C	N	P	O
Dominant species	HCO$_3^-$	NO$_3^-$	H$_2$PO$_4^-$/HPO$_4^{2-}$	O$_2$
$K_{S,i}$ **(mM)** [**13, 57, 75**]	0.2	0.5	0.017	–
$K_{I,i}$ **(mM)** [**76**]	–	–	–	2.7
$Y_{X/i}$ **(kg/kmol)** [**4, 17, 54**]	22.4	178	3570	–
$D_{i,w}$ **(m^2/s$\times$10^{10})** [**61, 127**]	11.8	17.0	7.6/8.8	20.0
$D_{i,b}$ **(m^2/s$\times$10^{10})**	2.2	3.2	1.5/1.7	3.8
$D_{i,p}$ **(m^2/s$\times$10^{10})**	9.4	13.6	6.1/7.0	16.0

Diffusive permeabilities of nutrient species

Table 3.2 also shows the dominant species containing C, N, and P in the pH range 7 to 10, along with their diffusion coefficients in the porous medium $(D_{i,p})$ and their diffusive permeabilities in the biofilm $(D_{i,b})$ [40, 61, 87, 127]. The relative effective diffusion coefficient of each species in the porous medium, $D_{i,p}^*$, was defined as its diffusion coefficient in the porous medium with respect to its diffusion coefficient in water. The value of $D_{i,p}^*$ was assumed to be equal to 0.8 based on the results presented by Mu *et al.* and assuming a porous medium void fraction of 0.85 [88]. Similarly, the relative effective diffusive permeability of species i in the biofilm, $D_{i,b}^*$, was calculated as [40],

$$D_{i,b}^* = 1 - \frac{0.43X^{0.92}}{11.19 + 0.27X^{0.99}} \tag{3.11}$$

where X is the microorganism concentration, given in kg DW/m^3.

3.3.2.4 Initial conditions

The initial conditions corresponded to the biofilm and porous medium being in equilibrium with the gas phase and nutrient medium in the dark. The initial dissolved inorganic carbon concentration in the system, $C_{i,T}$, can therefore be written as [87],

$$C_{i,T}(x, y, t = 0) = p_{CO_2} K_{H,CO_2} \left(1 + K_{a1} \left[H^+ \right]^{-1} + K_{a1} K_{a2} \left[H^+ \right]^{-2} \right) \tag{3.12}$$

where p_{CO_2} is the partial pressure of CO$_2$ in the gas phase, equal to 38 Pa, which corresponds to atmospheric air [86], and K_{H,CO_2} is Henry's constant for aqueous CO$_2$ in equilibrium with the gas phase, equal to 3.4×10^{-7} M/Pa

at 25^oC [87]. Moreover, K_{a1} and K_{a2} are the first and second equilibrium constants for the carbonate system, equal to $10^{-6.3}$ and $10^{-10.3}$, respectively, and $[H^+]$ is the proton concentration, equal to 10^{-pH} [87]. The three terms on the right hand side represent carbonic acid $[H_2CO_3^*]$, bicarbonate $[HCO_3^-]$, and carbonate $[CO_3^{2-}]$, respectively.

Similarly, the initial dissolved oxygen concentration was given by [87],

$$[O_2](x, y, t = 0) = p_{O_2}K_{H,O_2} \tag{3.13}$$

where p_{O_2} is the partial pressure of oxygen in the gas phase, equal to 21.3 kPa, and K_{H,O_2} is Henry's constant for aqueous oxygen in equilibrium with the gas phase, equal to 1.3×10^{-8} M/Pa at 25^oC [87]. Thus, the initial oxygen concentration at all locations in the biofilm and the porous medium was 2.7 $\times 10^{-4}$ M.

The initial concentrations of nitrate $[NO_3^-]$ and total inorganic phosphate P_T, given by the sum of $[H_2PO_4^-]$ and $[HPO_4^{2-}]$, were equal to their concentrations in fresh BG11 medium. The initial conditions for the concentrations of these nutrients can therefore be written as,

$$[NO_3^-](x, y, t = 0) = [NO_3^-]_o \tag{3.14}$$

$$P_T(x, y, t = 0) = P_{T,o} \tag{3.15}$$

where $[NO_3^-]_o$ and $P_{T,o}$ were equal to 1.8×10^{-2} M and 2.3×10^{-4} M, respectively [124].

3.3.2.5   Boundary conditions

In PSBRs, inorganic carbon and molecular oxygen are exchanged directly with the gas phase adjacent to the biofilm, whereas all other dissolved nutrients are delivered from the porous medium side by the nutrient medium. Thus, the biofilm surface was taken to be in chemical equilibrium with the gas phase at all times. Moreover, a zero flux boundary condition was imposed at the interface between the porous medium and the impermeable wall supporting it. Therefore, the boundary conditions for the total inorganic carbon concentration can be written as [87],

$$C_{i,T}(x, y = 0, t) = p_{CO_2} K_{H,CO_2} \left(1 + K_{a1} \left[H^+ \right]^{-1} + K_{a1} K_{a2} \left[H^+ \right]^{-2} \right) \quad (3.16)$$

$$\frac{\partial C_{i,T}}{\partial y}(x, y = L_b + L_p, t) = 0 \quad (3.17)$$

Similarly, the boundary conditions for the molecular oxygen concentration can be written as [87],

$$[O_2](x, y = 0, t) = p_{O_2} K_{H,O_2} \quad (3.18)$$

$$\frac{\partial [O_2]}{\partial y}(x, y = L_b + L_p, t) = 0 \quad (3.19)$$

For dissolved nitrate and phosphate, there were zero flux boundary conditions at the interface between the biofilm and the gas phase and at the interface between the porous medium and the solid supporting wall, which can be written as,

$$\frac{\partial [i]}{\partial y}(x, y = 0, t) = 0 \quad (3.20)$$

$$\frac{\partial [i]}{\partial y}(x, y = L_p + L_b, t) = 0 \tag{3.21}$$

Moreover, the concentration of each nutrient at the the nutrient medium inlet was equal to its concentration in fresh BG11, $[i]_o$, which can be written as,

$$[i](x = 0, y, t) = [i]_o \tag{3.22}$$

3.3.2.6 Biofilm performance metrics

Performance metrics were developed to investigate causes of suboptimal local growth rates and to guide development of strategies to improve these suboptimal rates. Due to consumption of nutrients in the direction of nutrient medium flow, it was expected that the growth rate would decline with increasing distance from the nutrient medium inlet. Therefore, the downstream distance at which the local thickness-averaged growth rate declined to half of its maximum value in the biofilm was defined as the half-growth length, $x_{50\%}$. The factor of one half was selected because growth rates less than half the maximum are often undesirable from a PSBR operation perspective. Moreover, to identify the specific cause of suboptimal local growth rates, the local delivery effectiveness for nutrient i, $\eta_{d,i}$, was defined as the ratio of the local growth rate to the growth rate that would exist with no limitation or inhibition by nutrient i. For oxygen, the parameter η was defined as the removal effectiveness rather than the delivery effectiveness as oxygen is inhibitory to growth. Moreover, the total nutrient delivery effectiveness η_d was defined as the product of all individual nutrient delivery effectivenesses.

3.3.2.7 Solution method and grid size independence

The transient, explicit discretization method was used to solve Equations (3.7)-(3.10) simultaneously [56]. Moreover, the pH at each location was calculated taking into account the local nutrient medium composition and the partial pressure of CO_2 using the software package Visual Minteq [50]. The system was deemed to be at steady state when the percent rate of change of the concentrations of all nutrients were less than 0.01% per second. Convergence studies were performed to ensure that the computed nutrient concentrations and growth rates were independent of spatial and temporal discretization. To do so, the discretization size in the in-plane and out-of-plane directions as well as the time step size were decreased until the relative discrepancy between the local growth rates obtained for two consecutive grid refinements did not change by more than 1%. This criterion was satisfied for a discretization scheme consisting of 10 nodes in the out-of-plane direction in each the biofilm and the porous medium, 10 nodes in the in-plane direction, and a time step of 0.05 s.

3.3.2.8 Experimental validation

To validate the model, the local biomass production rate of *Anabaena variabilis* was quantified in a custom PSBR. The schematic of the PSBR used for the validation experiment is shown in Figure 3.2a. The system featured a growth area measuring 8 mm wide by 60 mm long which was inoculated with *A. variabilis* at an initial areal biomass concentration of 1.1 g/m^2. Flow through the reactor was driven by evaporation from the terminal end of the

porous medium. The flow rate of nutrient medium was quantified by measuring the change in mass of nutrient medium in the nutrient medium reservoir. The superficial nutrient medium velocity, u_p, was calculated by dividing the flow rate by the cross sectional area of the porous medium, and was equal to 4.70 $\pm$ 0.06 μm/s over the duration of the experiment. The biofilm was illuminated with fluorescent bulbs (Philips, color temperature 4100 K) at an irradiance of 24 $\pm$ 1 W/m^2 PAR. The partial pressures of CO_2 and O_2 in the gas phase inside the reactor were measured with a gas chromatograph (Shimadzu, GC-2014a) and were 38 Pa and 21.2 kPa, respectively. The temperature throughout the duration of the experiment was 25.0 $\pm$ 0.4^{o}C. The local areal biomass concentration was periodically measured at six discretized regions along the length of the biofilm using a multispectral imaging technique. [94] The areal biomass production rate between data points, $\dot{X}_A$, was calculated by dividing the increase in areal biomass concentration by the time duration between measurements.

3.4 Results and Discussion
3.4.1 Experimental validation

Figure 3.2b compares the areal biomass production rates measured experimentally with those predicted by the model. The uncertainties in the experimental model are the result of the combined uncertainties of the image analysis method used to quantify the biomass at different time points and the linear least squares regression line used to quantify the change in biomass

concentration over time. [53, 94] The figure indicates that the experimental biomass production rate as a function of downstream location was predicted well by the model. The maximum growth rate in the biofilm occurred in the region between 0 and 1 cm from the nutrient medium inlet. The experimental maximum biomass production rate and the biomass production rate predicted by the model were 0.055 and 0.048 g/m^2-hr, respectively. Moreover, the experimental and predicted half growth lengths were about 2.0 and 2.2 cm, respectively. Thus, the growth rates and half growth lengths reported by the model can be considered accurate to within about 15% and 10%, respectively.

3.4.2   Biofilm growth rate without nutrient limitation or inhibition

First, the local growth rates in the biofilm were calculated taking into account only the local irradiance, assuming no nutrient limitation or inhibition. This maximum photon utilization case serves as a benchmark for evaluating mass transport limited growth rates.

Figure 3.3 shows the local photosynthetically active irradiance as well as the local growth rates assuming no nutrient limitation or inhibition within biofilms of thickness 20 μm, 100 μm, and 200 μm, irradiated at 20 and 200 W/m^2 PAR, as functions of local optical thickness τ. At 20 W/m^2 irradiance, the biofilm displayed a light limited regime at the illuminated surface where the maximum growth rate was 0.08 h^{-1}. On the other hand, at 200 W/m^2 irradiance, the biofilm was light inhibited from the illuminated surface up to an optical depth of 0.45 at which the maximum growth rate of 0.09 h^{-1} was

46
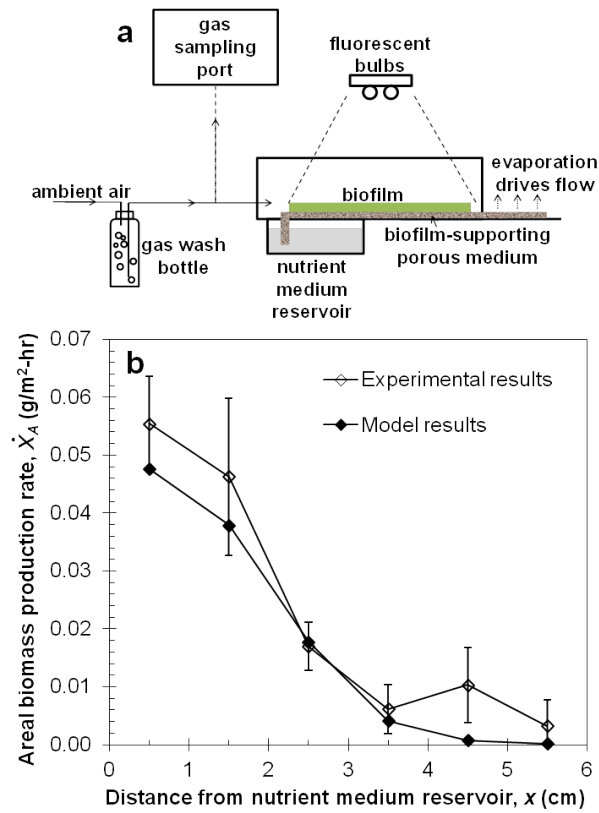
Figure 3.2: (a) The PSBR used to validate the model and (b) comparison of the areal biomass production rate predicted by the model and observed experimentally.

reached.

Additionally, Figure 3.4 shows the total biomass production rates of the biofilms of thickness 20 μm, 100 μm, and 200 μm as functions of incident irradiances ranging from 0 to 400 W/m^2 PAR, which is the range expected for systems using natural sunlight. For the 100 μm and 200 μm thick biofilms, the total biomass production rate increased monotonically with increasing incident irradiance, and maximum biomass production rates of 0.80 and 1.0 g/m^2-hr,
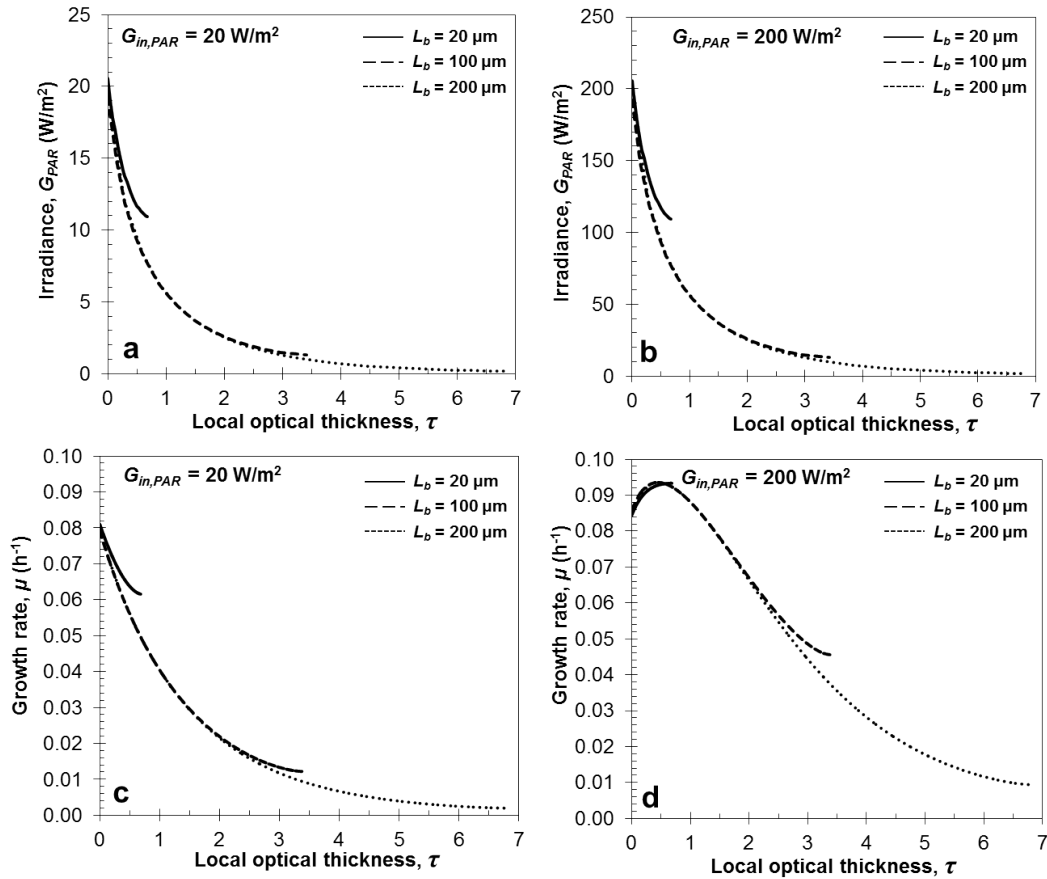
Figure 3.3: (a,b) Local photosynthetically active irradiance as a function of local optical thickness for an incident irradiance of 20 W/m² and 200 W/m² PAR, and (c,d) local growth rate with no nutrient limitation or inhibition for incident irradiances of 20 W/m² and 200 W/m² PAR.

respectively, occurred at the maximum irradiance of 400 W/m² PAR. On the other hand, the maximum total biomass production rate for the 20 μm thick biofilm of 0.19 g/m²-hr occurred at an incident irradiance of 200 W/m² PAR. At irradiances greater than 200 W/m² PAR, the entire 20 μm thick biofilm was photoinhibited, whereas photoinhibition in the 100 μm and 200 μm thick

48

biofilms was confined to a region within 25 μm of the illuminated surface even at the maximum irradiance of 400 W/m^2.
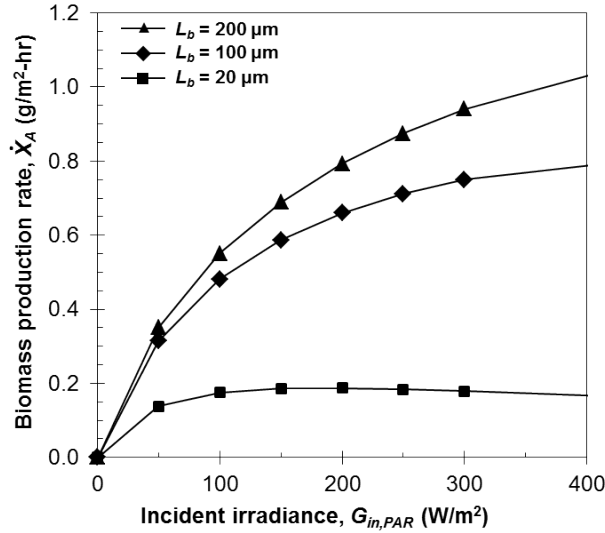
Figure 3.4: Total biomass production rate as a function of incident photosynthetically active irradiance for biofilm thicknesses of 20 μm, 100 μm and 200 μm.

The results of this case of no nutrient limitation of inhibition indicated that the most productive biofilm was a 200 μm thick one under an incident irradiance of 400 W/m^2 PAR. However, a 100 μm thick biofilm was considered for the mass transport analysis as this was the thickest cyanobacterial biofilm observed in PSBRs in our laboratory. Moreover, as shown in previous PSBR studies, multiple vertical biofilm units are often utilized in order to increase the total illuminated biofilm surface area, which in turn dilutes the irradiance onto the biofilms [71, 93, 97]. From a light transfer perspective, the overall PSBR productivity is a function of the spacing aspect ratio, which is defined

as the ratio of the spacing between vertical units to the height of the units. It was determined that the total productivity of a PSBR cultivating 100 μm thick biofilms of *A. variabilis* under full sunlight (400 W/m^2 PAR) would be maximized using a spacing aspect ratio of approximately 0.1. This aspect ratio corresponds to an average irradiance onto each biofilm of 20 W/m^2 PAR, and this irradiance was therefore simulated in the mass transport analysis.

3.4.3 Flux balancing of nutrients and photons

To demonstrate the utility of the model, this section focuses first on modeling the performance of an unoptimized base case scenario based on the system reported by Murphy *et al* [93]. Then, performance metrics are applied to determine the locations of specific nutrient limitations. Strategies are then developed to mitigate these limitations based on balancing the fluxes of nutrients with those of photons. Finally, a flux-balanced case is presented for demonstrating the improvement of total biofilm productivity.

3.4.3.1 Base case simulation

The parameters for the base case simulation were selected based on the system reported by Murphy *et al.* [93] and are marked with an asterisk (*) in Table 3.3. Figure 3.5 shows the local growth rates, pH, and concentrations of total inorganic carbon, molecular oxygen, nitrate, and phosphate within the biofilm. It indicates that for distances from the nutrient medium inlet less than 1 cm, the growth rate decreased exponentially with increasing distance

from the illuminated surface. In this region, the average growth rate was 64%
of its value for the case of no nutrient limitation or inhibition. However, the
growth rate showed a steep decline at distances greater than 1 cm from the
nutrient medium inlet. The half growth length, $x_{50\%}$, was equal to 1.5 cm in
the base case.

Table 3.3: Parameter values investigated in this study.

Parameter	Values
Irradiance, G_{PAR} (W/m^2)	20*, 40
Initial phosphate concentration, $P_{T,o}$ (mM)	0.23*, 0.46
Nutrient medium superficial velocity, u_p (μm/s)	5*, 10, 50, 100
Biofilm thickness, L_b (μm)	50, 100*
Porous medium thickness, L_p (μm)	200, 500*

*Indicates base case value

To elucidate the cause of the declining growth rate in the flow direction,
Figure 3.6 shows the local delivery/removal effectivenesses of total carbon,
oxygen, total phosphate, and nitrate for the base case. The figure indicates
that the minimum values of η_{d,C_T}, η_{r,O_2}, and η_{d,NO_3^-} in the biofilm were 0.93,
0.88, and 0.96, respectively (Figures 3.6a-c), whereas the phosphate delivery
effectiveness decreased to 0.5 at an in-plane distance of 1.4 cm (Figure 3.6d).
Thus, decreasing growth rate in the direction of nutrient medium flow can
be attributed to inadequate phosphate delivery. Moreover, the total nutrient
delivery effectiveness averaged over the entire biofilm, η_d, was 37%. Therefore,
the biofilm productivity can be enhanced by a factor of 2.7 compared to the
base case by balancing the nutrient fluxes with the photon fluxes to the cells.
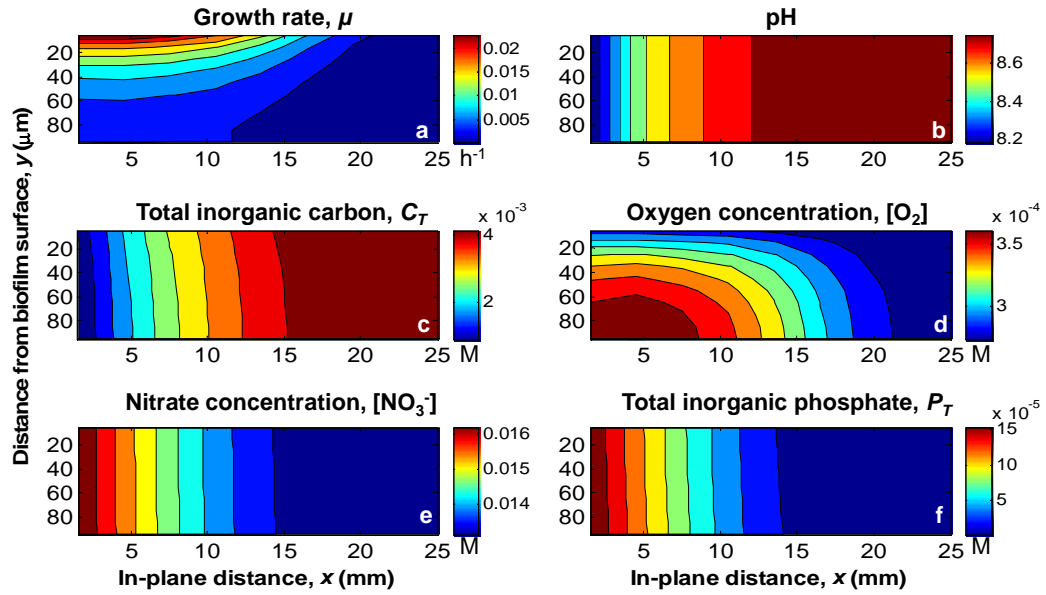
Figure 3.5: Local (a) growth rate, (b) pH, and concentrations of (c) total inorganic carbon, (d) molecular oxygen, (e) nitrate, and (f) phosphate for the base case simulation.
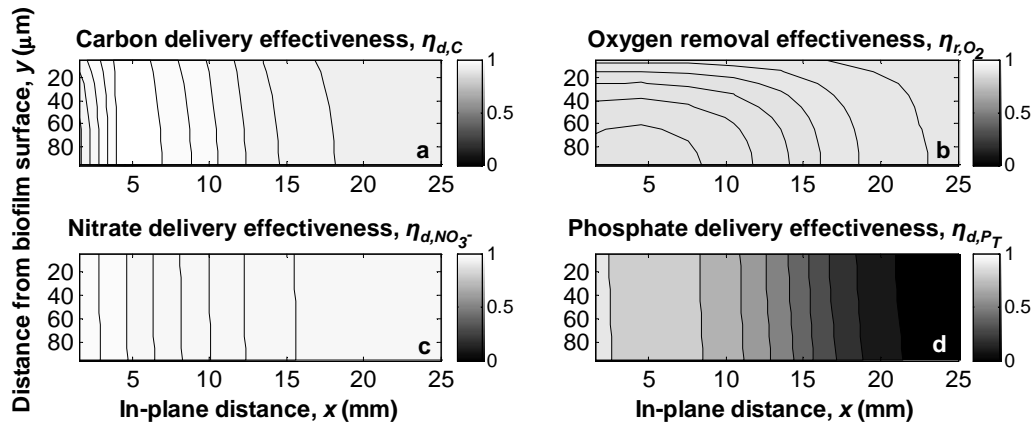
Figure 3.6: (a) Carbon delivery effectiveness, (b) oxygen removal effectiveness, and delivery effectivenesses for (c) nitrate and (d) phosphate for the base case simulation.

3.4.3.2 Scaling analysis for nutrient delivery enhancement

To develop a generalized strategy for mitigating the inadequate nutrient delivery observed in the base case, a scaling analysis was performed in which the nutrient delivery rate into the porous medium was compared to the nutrient consumption rate by the biofilm. Neglecting diffusion in the in-plane direction in the porous medium yields the relationship,

$$u_p L_p [i_L]_o \sim \frac{\mu_o X L_b}{Y_{X/i_L}} x_{50\%} \tag{3.23}$$

where the left and right hand sides represent the transport and consumption rates, respectively, of the growth-limiting nutrient i_L, which is phosphate in the current study. The parameters $[i_L]_o$ and μ_o represent the concentration of the growth-limiting nutrient and the thickness-averaged growth rate, respectively, at the nutrient medium inlet. Rearranging Equation (3.23) for the half-growth length $x_{50\%}$ yields,

$$x_{50\%} = C_{A.v.} \frac{u_p L_p [i_L]_o Y_{X/i_L}}{\mu_o X L_b} \tag{3.24}$$

where $C_{A.v.}$ is a microorganism-specific constant which is dependent on the Monod growth kinetics.

Using the values indicated in Table 3.3, a parameter sweep was performed to validate the form of Equation (3.24) and to recover the constant $C_{A.v.}$. Figure 3.7 shows that the relationship between the half-growth length and the scaling length was indeed linear. A least squares linear regression indicated that the slope of the line, equal to the constant $C_{A.v.}$, was 0.187, with

a coefficient of determination R^2 of 0.998. Knowledge of the constant $C_{A.v.}$ enables designers to properly size PSBRs in the direction of nutrient medium flow.
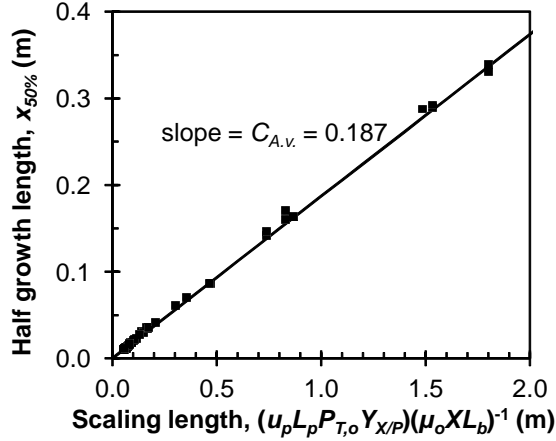
Figure 3.7: Results of the parameter sweep. The slope of the line is equal to the microorganism-specific constant $C_{A.v.}$.

To demonstrate the utility of Equation (3.24) in PSBR design, a flux balanced case was simulated using the exemplary biofilm from the base case. In the flux balanced case, the half growth length $x_{50\%}$ was matched to the physical length of the system of 2.5 cm by increasing the nutrient medium velocity u_p from 5 μm/s to 8.3 μm/s. Figure 3.8a shows the local growth rates for the flux balanced case. Furthermore, Figures 3.8b-e show the individual delivery/removal effectivenesses for carbon, oxygen, nitrate, and phosphate, respectively. The minimum phosphate delivery effectiveness in the biofilm increased from 0.8% in the base case to 71% in the flux balanced case, indicating the mitigation of phosphate limited growth. Moreover, the average total nu-

54

trient delivery effectiveness increased from 37% to 59%, corresponding to an increase in biofilm productivity from 0.048 to 0.077 grams per square meter of biofilm area per hour. Considering the spacing aspect ratio of 0.1, this corresponds to an increase in overall PSBR productivity from 0.96 to 1.54 grams per square meter of footprint area per hour. The flux balanced PSBR system is therefore competitive with raceway ponds and planktonic photobioreactors, which have characteristic productivities ranging from 11 to 27 g/m^2-day.
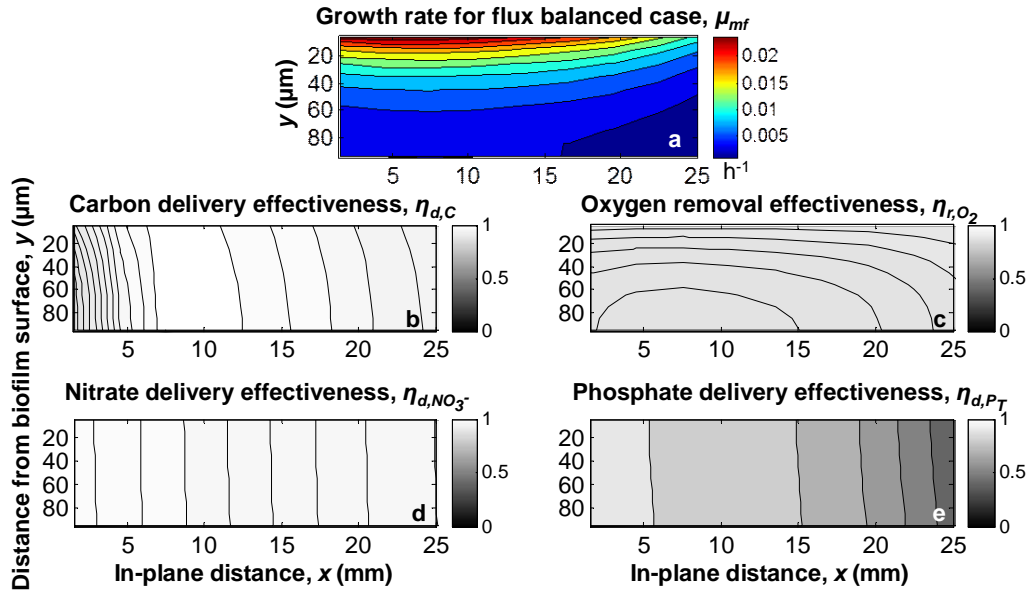
Figure 3.8: Local (a) growth rate, (b) carbon delivery effectiveness, (c) oxygen removal effectiveness, and delivery effectivenesses for (d) nitrate and (e) phosphate for the flux balanced case.

Equation (3.24) indicates that the half growth length can be increased indefinitely by increasing the nutrient medium velocity through the porous medium. However, there are practical limitations on the nutrient medium

velocity. For example, if flow through the porous medium is driven by a pump, as was the case for the PSBRs presented by Naumann *et al.* [97] and Liu *et al.* [71], then the pumping power required per square meter of PSBR footprint area can be written as,

$$P_p'' = \frac{u_p L_p}{s} \left(\frac{\mu_w u_p}{k_p} + \rho_w g \right) \tag{3.25}$$

where μ_w is the dynamic viscosity of water, k_p is the hydraulic permeability of the porous medium, and s is the spacing aspect ratio. The first parenthetical term represents viscous losses through the porous medium and the second represents losses due to gravity. From a biofuels perspective, it is impractical to expend more pumping power than is available from the solar irradiance. It was estimated that a flow speed of 1.5 cm/s makes the pumping power per unit area equal to the incident solar power. This flow speed corresponds to a half growth length of 42 m. At system heights greater than 42 m, the pumping power alone is equal to the total incident solar power, and the amount of energy produced by the reactor is necessarily less than the input energy.

Moreover, in the PSBR presented by Murphy *et al.* [93], flow through the porous medium was driven by evaporation from a terminal membrane rather than by a pump. In this system, the maximum flow rate is dictated by the temperature, relative humidity, and velocity of the gas phase surrounding the evaporator membrane. It was estimated that the maximum flow velocity through the porous medium for a system driven by evaporation was approximately 50 μm/s, corresponding to a half growth length of about 10 cm.

Therefore, evaporation driven PSBRs should be designed such that the porous medium is supplied with fresh nutrient medium at increments of no more than 10 cm in the direction of flow.

Another way to increase the half growth length is to increase the concentration of the growth-limiting nutrient in fresh nutrient medium. However, this concentration can only be increased to a critical value, at which point another nutrient will become growth-limiting. For the example of cultivating cyanobacteria with BG11, when the phosphate concentration in fresh medium is doubled, calcium becomes limiting to growth (Table 3.1). To address this challenge, custom nutrient medium can be engineered that matches the elemental composition of the organism being cultivated, a strategy which has been successfully applied to suspended cultivation of green algae [32, 74]. Moreover, such an engineered nutrient medium can be used in concentrated form to increase the half growth length while maintaining a constant flow velocity. However, solid precipitation within the porous medium as well as adverse effects of altered pH on microorganism productivity must carefully be taken into account.

3.5 Conclusions

This paper reported a comprehensive model integrating light transport, mass transport, and algal growth kinetics for understanding the effects of nutrient and photon delivery on the productivity of photosynthetic biofilms. The model was validated against experimental data and an exemplary Porous

Substrate Bioreactor cultivating *Anabaena variabilis* with the BG11 nutrient medium was simulated. In an unoptimized base case, the ratio of the total productivity to the productivity under no nutrient limitation or inhibition was 37%. The half growth length was then matched to the physical length of the system, and using this strategy the productivity ratio was increased to 59%. The model reported serves as a numerical tool for designing and optimizing the operating parameters of photosynthetic biofilm based cultivation systems.

Nomenclature

A_{abs} mass absorption cross section, m^2/kg

$C_{i,T}$ total dissolved inorganic carbon, mol/L

$D_{i,j}$ diffusion coefficient or diffusive permeability of species i in species j, m^2/s

$D_{i,j}^*$ relative diffusion coefficient or diffusive permeability of species i in species j

De delivery number

E_{ext} mass extinction cross section, m^2/kg

G irradiance, W/m^2

I_λ spectral radiant intensity, W/m^2-nm-sr

$[i]$ concentration of species i, mol/L

K constant for Monod model, W/m^2 or mol/L

K_a equilibrium constant for carbonate system, mol/L

$K_{H,i}$ Henry's constant for species i in water, mol/L-Pa

k absorption index

L thickness, m

l length of the system, m

p pressure, Pa

P_T total dissolved inorganic phosphate, mol/L

r reflectance

S_{sca} mass scattering cross section, m^2/kg

T temperature, ^{o}C

t time, s

u_p superficial in-plane velocity, m/s

X microorganism concentration, kg dry weight (DW)/m^3

$\dot{X}_A$ rate of areal biomass concentration increase, kg/m^2-s

x dimension in the direction of nutrient medium flow, m

$x_{50\%}$ half-growth length, m

$Y_{X/i}$ biomass yield based on amount of i consumed, kg DW/kmol i

y dimension perpendicular to nutrient medium flow, m

Nomenclature (cont.)

Greek symbols

γ	consumption rate, mol/L-s
$\eta_{d/r}$	delivery/removal effectiveness
θ	zenith angle, rad
κ	absorption coefficient, m^{-1}
λ	wavelength, nm
μ	growth rate, s^{-1}
ν	specific volume, m^3/kg
σ	scattering coefficient, m^{-1}
τ	local optical thickness
Φ	scattering phase function
Ω	solid angle, sr

Subscripts

b	refers to biofilm
I	refers to inhibition
i	refers to nutrient species i
in	refers to incident
m	refers to medium
max	refers to maximum
o	refers to the nutrient medium inlet
p	refers to porous medium
S	refers to half-saturation

Abbreviations

PAR	photosynthetically active radiation
RTE	radiative transport equation

Chapter 4

Design of the vascular structure of an evaporation driven Porous Substrate Bioreactor

4.1 Introduction

This chapter focuses on the physics governing the liquid flow rate through an evaporation driven Porous Substrate Bioreactor (PSBR). Evaporation driven PSBRs eliminate the energetic and monetary requirements of a pump for nutrient delivery to the cells. However, the flow rate is dependent on the evaporation rate from the terminal porous medium region, which is in turn dependent on environmental conditions. This analysis aims to model the flow rate through an evaporation driven PSBR as a function of environmental conditions and mechanical properties of the porous material.

4.2 Analysis

Figure 4.1 shows a single porous rib of an evaporation driven Porous Substrate Bioreactor (PSBR). The exterior rib section has a height h_e, but the liquid only wets a critical wetting length of x_c as a result of the balance between capillary, viscous, and gravitational forces. The flow rate through the

interior rib section, which has height h_i and hosts microbial growth, is then equal to the evaporation rate from the exterior rib section. The rib has a thickness t, an average pore radius r and void fraction ϵ. The contact angle between the solid material of the rib and the liquid nutrient medium is θ. The gas surrounding the exterior section has temperature T, relative humidity RH, and velocity v_w in the direction into the page. The rib is irradiated with an irradiance G_r.
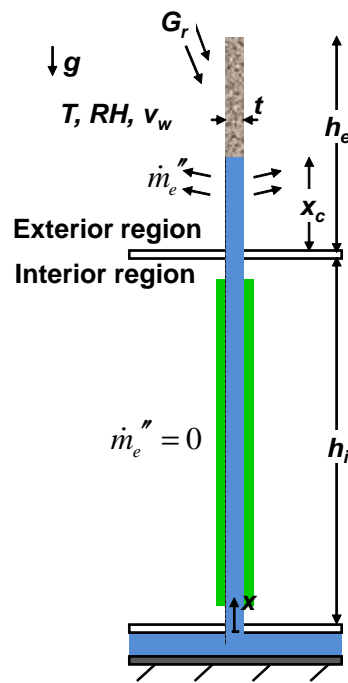
Figure 4.1: Schematic of a single rib of an evaporation driven PSBR.

4.2.1 Assumptions

It is assumed that (1) the system is at steady state, (2) the irradiance onto the rib is uniform, (3) the gas surrounding the interior rib section is saturated with water vapor at the biofilm surface temperature T_s, resulting in zero evaporation from the inerior surface, (4) the gas in both the interior and exterior regions is at atmospheric pressure (101 kPa), (5) the viscosity, density, surface tension, and contact angle with the porous material for the liquid medium flowing through the rib are equal to the respective properties for pure water, and (6) the pore size is uniform in the rib and equal to the average pore size.

4.2.2 Governing equations

To determine the critical wetting length, first the steady state momentum balance in the rib is written as,

$$\frac{dP}{dx} = -\frac{\mu}{tk\rho}\dot{m}'(x) - \rho g \tag{4.1}$$

where μ and ρ are the dynamic viscosity and density of water, respectively, k and t are the permeability and thickness of the porous material, respectively, and g is the gravitational acceleration. The first term on the right hand side represents the pressure drop due to viscous losses and the second term represents the losses due to gravity. The local mass flow rate along the length

of the rib per unit width into the page, $\dot{m}'(x)$, can be written as,

$$\dot{m}'(x) \;=\; 2\dot{m}_e{}''x_c \quad \text{for} \quad 0 \le x \le h_i \tag{4.2}$$

$$\dot{m}'(x) \;=\; 2\dot{m}_e{}''(x_c - (x - h_i)) \quad \text{for} \quad h_i \le x \le h_i + x_c \tag{4.3}$$

where $\dot{m}_e{}''$ is the evaporative flux from the exterior rib. The boundary conditions are that (i) the pressure at the base of the interior region is equal to the maximum capillary pressure P_c, and (ii) the pressure as a function of height is continuous at the interface between the interior and exterior regions. These boundary conditions can be written as,

$$P(x = 0) \;=\; P_c \tag{4.4}$$

$$P_{int}(x = h_i) \;=\; P_{ext}(x = h_i) \tag{4.5}$$

Substituting Equations (4.2) into Equation (4.1) and applying the boundary conditions yields the following expressions for the interior and exterior pressures:

$$P(x) \;=\; P_c - \frac{2\mu\dot{m}_e{}''}{tk\rho}x_c x - \rho g x \quad \text{for } 0 \le x \le h \tag{4.6}$$

$$P(x) \;=\; P_c - \frac{2\mu\dot{m}_e{}''}{tk\rho}\left(x_c x - \frac{1}{2}(x - h)^2\right) - \rho g x \quad \text{for } h \le x \le h + x_c \tag{4.7}$$

At the critical wetting length, the pressure is equal to zero. Using this condition yields a quadratic relation for x_c. The expression for x_c can therefore be written as,

$$x_c = \frac{-b \pm \sqrt{b^2 - 4ac}}{2a} \tag{4.8}$$

64

where $a = -\mu \dot{m}_e'' / tk\rho$, $b = -\rho g - 2\dot{m}_e'' \mu h_i / tk\rho$, and $c = P_c - \rho g h_i$. The critical length can then be substituted into Equation (4.2) to calculate the flow rate through the rib.

Moreover, the capillary pressure exerted by the porous material is given by the Laplace equation [34]:

$$P_c = \frac{2\sigma \cos\theta}{r} \tag{4.9}$$

where σ is the surface tension of the liquid medium and θ is the contact angle between the nutrient medium and the bulk solid membrane material, which were estimated using values from the literature [1, 103, 128]. Moreover, the hydraulic permeability k was estimated as a function of the average pore radius r and void fraction ϵ, as these properties are conventionally reported by membrane manufacturers. The Millington model was used to estimate the hydraulic permeability, and is given by [81],

$$k = 1/8\epsilon^{4/3} r^2 \tag{4.10}$$

Finally, for all simulations, the height of the interior region h_i was 10 cm.

4.2.3 Evaporative flux from the exterior region

The evaporative flux from the membrane in the exterior region, $\dot{m}_e''$, is a function of the temperature of the membrane, which is in turn dependent on the evaporative flux. Therefore, the following energy balance was utilized to determine the steady state rib surface temperature T_r as a function of

environmental conditions:

$$\alpha G_r + h_c(T_\infty - T_r) - k_\omega \left(\omega_r(T_r) - \omega_\infty(T_\infty)\right) h_{fg} = 0 \qquad (4.11)$$

where α is the total absorptivity of the rib with respect to the incident radiation G_r, h and k_ω are the heat and mass transfer coefficients between the rib surface and the surrounding air, ω_r and ω_∞ are the mass fractions of water vapor at the rib surface and in the ambient air, respectively, and h_{fg} is the heat of vaporization of water. Equation (4.11) can be solved iteratively for the rib surface temperature T_r. The evaporative flux $\dot{m}_e''$ is then calculated as,

$$\dot{m}_e'' = k_\omega \left(\omega_r(T_r) - \omega_\infty(T_\infty)\right) \qquad (4.12)$$

The mass transfer coefficient k_ω was calculated from the Sherwood number as [18, 82],

$$Sh = \frac{k_\omega x_c}{\rho_a D_{w,a}} = \left(Sh_n^{7/2} + Sh_f^{7/2}\right)^{2/7} \qquad (4.13)$$

where ρ_a and $D_{w,a}$ are the density of air and the diffusivity of water vapor in air, respectively. The natural convection Sherwood number, Sh_n, was calculated using the correlation proposed by Incropera et $al.$ [56],

$$Sh_n = \frac{0.68 + 0.67 Sc^{1/4} Gr^{1/4}}{(1 + (0.492/Sc)^{9/16})^{4/9}} \qquad (4.14)$$

where Sc and Gr are the Schmidt and Grashof numbers, respectively. Moreover, the Sherwood number for forced convection, Sh_f, was calculated taking into account both laminar and turbulent flow by using the correlation [56],

$$Sh_f = \left(0.037 Re^{4/5} - 871\right) Sc^{1/3} \qquad (4.15)$$

66

where Re is the Reynolds number based on the wind speed and the characteristic length of the system. The characteristic length for forced convection was 10 m, based on the size of a scaled up PSBR. The heat transfer coefficient h_c was calculated using the heat and mass transfer analogy. Equations (4.13-4.15) were used, substituting the Nusselt number for the Sherwood number and the Prandtl number for the Schmidt number [56].

4.2.4   Closure laws

A case study was performed in which the flow rate through typical membranes were investigated for typical environmental conditions. This section describes the mechanical properties of the three membranes as well as the environmental conditions investigated.

4.2.5   Mechanical properties of three porous materials

Three commercially available porous media were investigated for use as the rib material. The three media investigated were made from surface-modified hydrophilic polyvinylidene fluoride (PVDF), glass fiber, and cellulose. Table 4.1 summarizes the material properties of these three membranes. The table indicates that the PVDF membrane exerts the greatest capillary pressure, but also has the lowest permeability of the three membranes as a result of it having the smallest pore size. On the other hand, the cellulose paper has the greatest permeability but the least maximum capillary pressure.

Table 4.1: Material properties, permeability, and maximum available capillary pressure for the three rib materials investigated.

	PVDF	Glass fiber	Cellulose
Brand	Millipore	Whatman	Fisher
Product code	DVP00010	GF/AH	P8
Thickness, t (mm)	0.13	0.33	0.20
Pore radius, r (μm)	0.6	1.5	20
Void fraction, ϵ	0.70	0.85	0.87
Contact angle, θ (deg)	55	20	39
Permeability, k (m^2 $\times$ 10^{12})	0.028	0.23	42
Capillary pressure, P_c (kPa)	128	91	5.7

4.2.5.1 Weather parameters for typical operating conditions

Four 24-hour simulations using weather parameters from representative days of spring, summer, fall, and winter were performed for Memphis, TN, USA. Memphis was selected as the location because of its moderately high annual insolation, proximity to water sources, and moderate temperatures that make it a good location for algae cultivation. The spring, summer, fall, and winter days were May 14, July 9, September 30, and November 29, respectively. The values for hourly air temperature, irradiance, relative humidity, and wind speed were obtained from the National Renewable Energy Laboratory's Typical Meteorological Year 3 Data, which reports real weather data that is deemed typical of the time span 1991 to 2005 [135]. The weather parameters used are shown in Figure 4.2. It was assumed that the irradiance onto the rib was equal to 10% of the global horizontal irradiance, which takes into account the projected area of the incident sunlight onto the vertical rib.
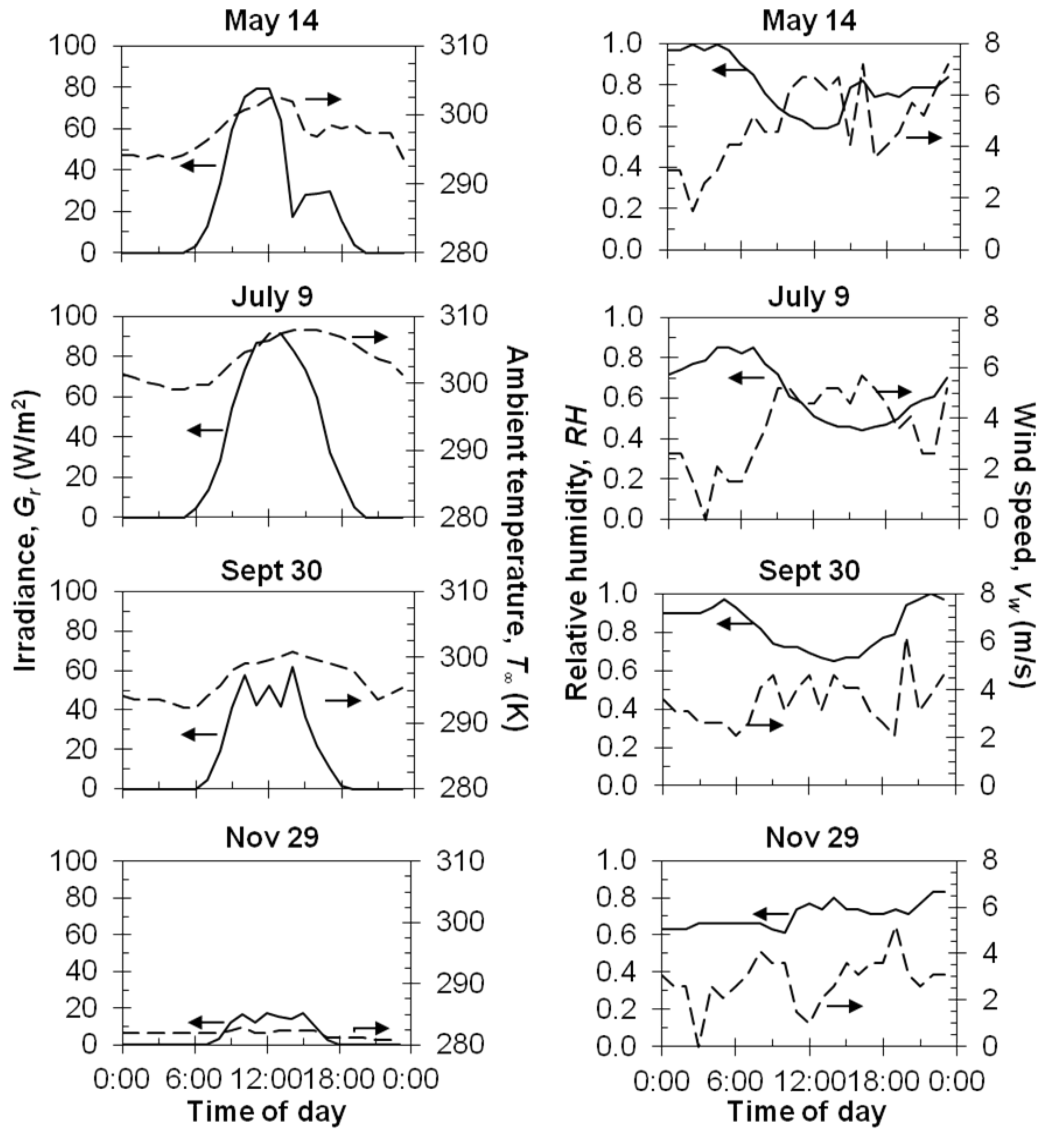
Figure 4.2: Irradiance per rib, air temperature, relative humidity, and wind speed for 24 hour periods in spring (May 14), summer (July 9), fall (September 30), and winter (November 29) for Memphis, TN, USA [135].

69

4.3 Results and Discussion

4.3.1 Range of expected evaporative fluxes

A parameter sweep was performed to determine the expected range of evaporative fluxes under typical outdoor operating conditions. Table 4.2 shows the parameter values investigated for irradiance onto the rib, ambient temperature, relative humidity, and wind speed. Figure 4.3 shows the effect of varying each parameter on the evaporative flux, $\dot{m}_e{}''$ on the evaporative flux from the rib. The figure indicates that the evaporative flux in the base case scenario was 36 mg/m^2-s. Moreover, the evaporative flux decreased from 65 mg/m^2-s to 14 mg/m^2-s as the relative humidity increased from 0% to 80%. Increasing the wind speed from 0 m/s to 8 m/s caused the evaporative flux to increase from 14 to 66 mg/m^2-s as a result of forced convection. Increasing the air temperature from 285 K to 305 K caused the flux to increase from 27 to 45 mg/m^2-s as a result of the increase in water vapor pressure at the rib surface. Finally, increasing the irradiance from 0 to 80 W/m^2 increased the flux from 34 to 40 mg/m^2-s.

Table 4.2: Environmental parameters used in the sensitivity analysis.

	Very low	Low	Base	High	Very high
Air temperature, T_∞ (K)	285	290	295	300	305
Relative humidity, RH (%)	0	20	40	60	80
Wind speed, v_w (m/s)	0	2	4	6	8
Irradiance, G_r (W/m^2)	0	20	40	60	80
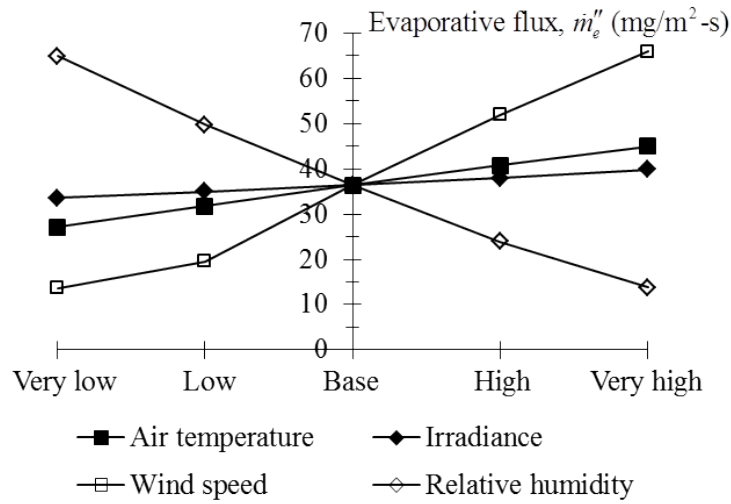
Figure 4.3: Effect of varying the irradiance onto the rib, air temperature, relative humidity, and wind speed on the evaporative flux from the rib.

4.3.2 Effect of porous medium properties on critical wetting length and total flow rate

To investigate the effects of the rib mechanical properties on system performance, the critical wetting length and the total system flow rate were calculated for hypothetical porous ribs with different pore radii r and contact angle θ. The pore radius varied between 100 nm and 1 mm and the contact angle varied between 0°, which represents the material capable of providing the maximum possible capillary pressure, and 85°. The void fraction and membrane thickness were held constant at 0.8 and 0.5 mm, respectively, typical of many commercially available porous substrates. Finally, evaporative fluxes investigated were 14 and 66 mg/m²-s, which represented the range of fluxes observed in the heat and mass transfer analysis.

Figure 4.4 shows the effect of pore radius and wetting angle on the critical wetting length. The flow rate through the rib can be calculated by multiplying the wetting length by twice the evaporative flux. For the slow evaporation (14 mg/m^2-s) and fast evaporation (66 mg/m^2-s) cases, the maximum wetting lengths were 1.1 m and 0.54 m, respectively, which correspond to flow rates of 31 mg/m-s and 36 mg/m-s, respectively. These maximum flow rates occurred for contact angles of zero, as would be expected as these materials provide the greatest possible capillary pressure. The wetting length approached zero as the contact angle approached 90°, indicating the change of the material from hydrophilic to hydrophobic. Therefore, only hydrophilic materials can be used in evaporation driven PSBRs.
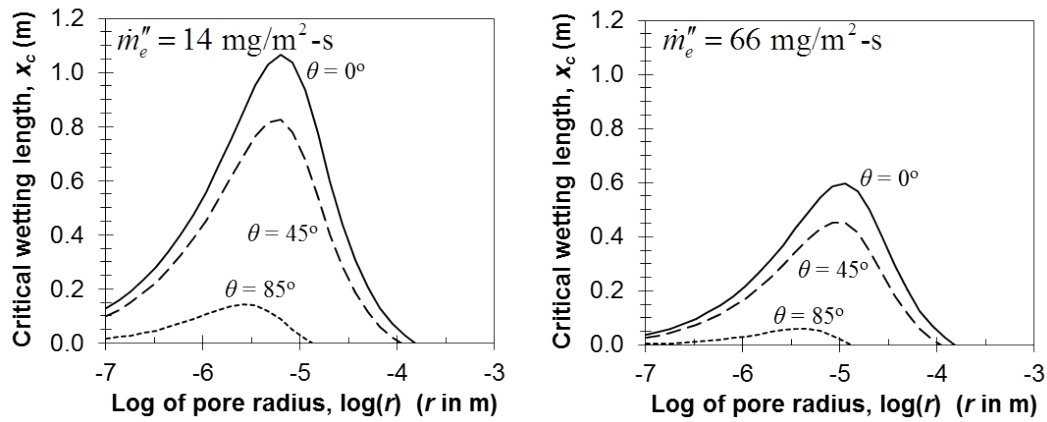
Figure 4.4: Effect of pore radius and contact angle between the solid material and liquid medium on the critical wetting length for an interior height of 10 cm.

Moreover, all cases featured a pore radius that maximized the wetting length. This occurred because the capillary pressure is inversely related to

pore radius, whereas the permeability is proportional to the square of the pore radius. For the slow evaporation case, the optimal pore radii for materials with contact angles of 0°, 45°, and 85° were 7 μm, 6 μm, and 3 μm, respectively. Increasing the contact angle decreased the capillary pressure, thereby reducing the wetting length and therefore the total flow rate, reducing viscous losses and allowing for smaller pore diameters. For the fast evaporation case, the optimal pore diameters for the contact angles of 0°, 45°, and 85° were 11 μm, 9 μm, and 5 μm, respectively. Therefore, for maximum flow rates, PSBRs should use porous ribs with pore diameters in the range of 1 to 10 μm.

4.3.3 Pressure distribution in the rib

Figure 4.5 shows the local pressure in the three membranes investigated as a function of height when exposed to the base case weather parameters (Table 4.2). For the PVDF, glass fiber, and cellulose membranes, the pressure at the base of the rib was equal to the maximum capillary pressure of 130 kPa, 92 kPa, and 5.7 kPa, respectively. Moreover, as a result of the constant mass flow rate in the interior region, the pressure gradients were constant at -10.8, -2.5, and -0.12 kPa/m, respectively. However, in the exterior region, the magnitude of the pressure gradient decreased with increasing height as a result of the declining mass flow rate due to evaporation. The critical wetting lengths for the PVDF, glass fiber, and cellulose membranes were 5.2, 31, and 37 cm, respectively. These critical wetting lengths correspond to total flow rates of 3.7, 22, and 27 mg/m-s, respectively, which represent the maximum

possible flow rates through these ribs for these environmental conditions. If the PSBR is designed such that the exposed rib section h_e is smaller than the critical length, the flow rate through the rib for this set of conditions will approximately scale by the ratio h_e/x_c.
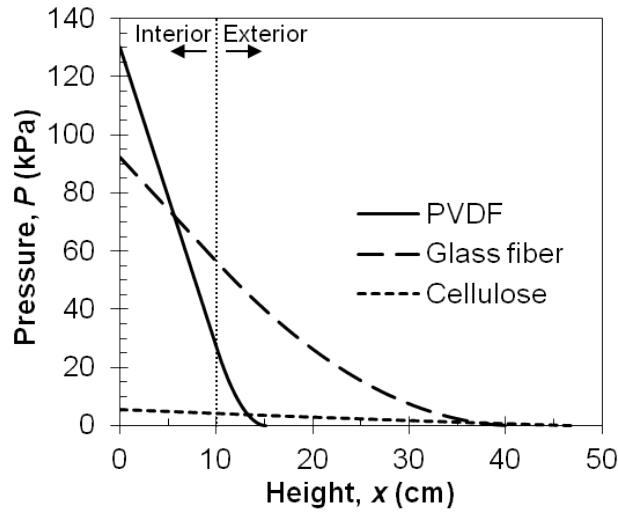
Figure 4.5: Pressure distributions within ribs made of PVDF, glass fiber, and cellulose for the base case environmental parameters.

4.3.4 Case study results: Daily and annual variations in critical wetting length and total flow rate

Figure 4.6 shows the critical wetting length and total flow rate for the PVDF membrane for spring, summer, fall, and winter simulations. Increasing evaporative flux decreased the critical wetting length while increasing the total flow rate. On May 14, this effect was highly pronounced at 2:00 AM and 4:00 AM, as the evaporative flux approached zero and the critical wetting length approached 13 m, which is the height at which the capillary pressure balances

74

the hydrostatic pressure in the absence of viscous losses. For the 24 hour simulations of spring, summer, fall, and winter, the daily evaporative flow rates were 0.14, 0.16, 0.12, and 0.10 liters per meter of rib length per day, respectively.
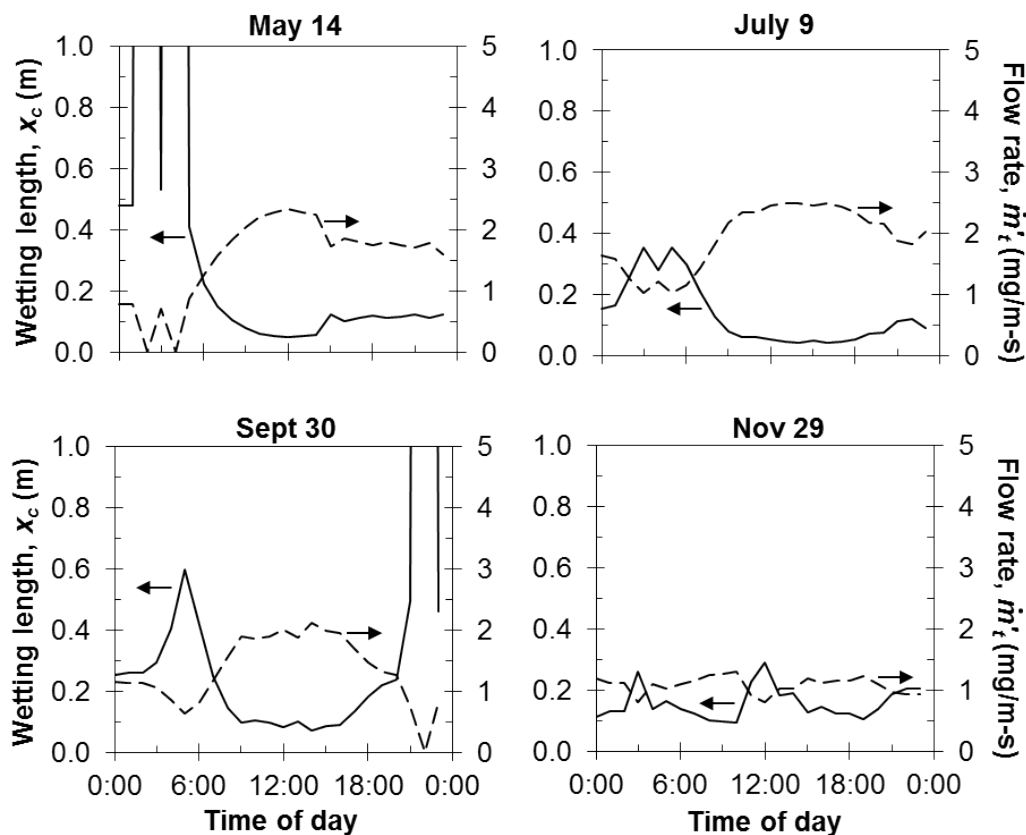
Figure 4.6: Critical wetting length and total flow rate through the PVDF rib throughout the 24 hour simulations for the spring, summer, fall, and winter.

Moreover, Figure 4.7 indicates that the behaviors of the critical wetting length and flow rate for the glass fiber rib were qualitatively similar as they were for the PVDF rib, although their magnitudes were about 4.5 times

greater for the glass fiber rib. Therefore, although the PVDF membrane can exert a capillary pressure 1.4 times greater than the glass fiber membrane, the effect of increased capillary pressure on flow rate is negated by the hydraulic permeability for the glass fiber membrane being about 8 times greater than that of the PVDF membrane.
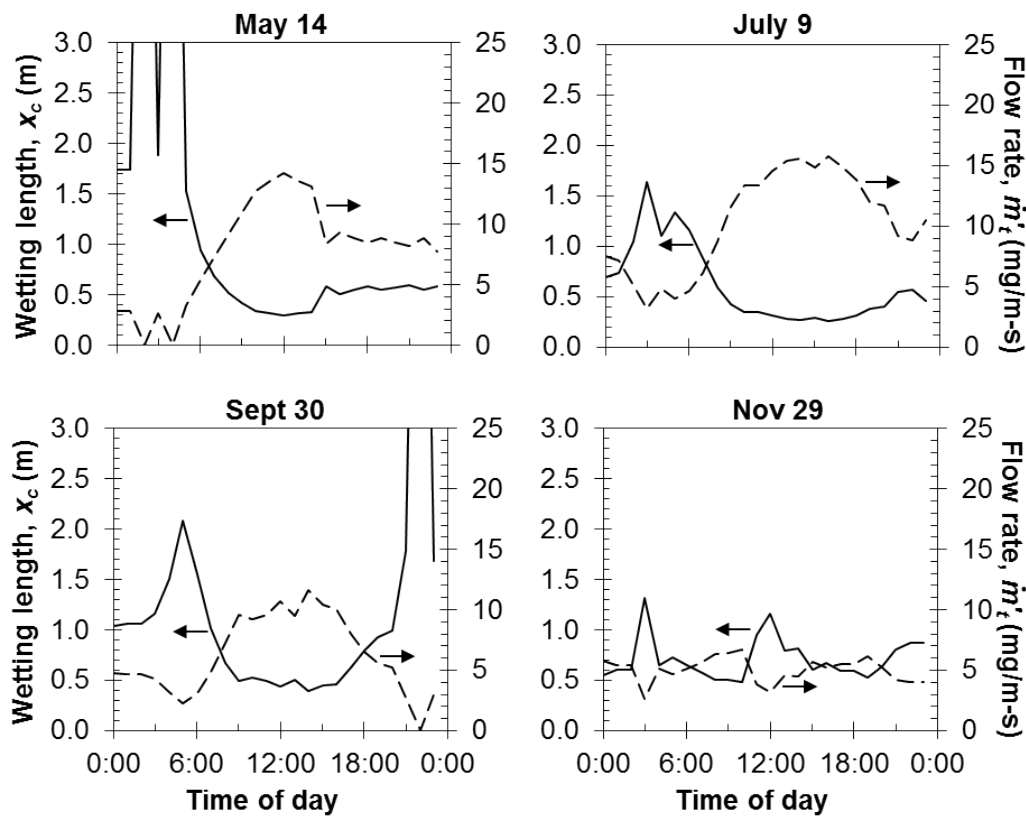
Figure 4.7: Critical wetting length and total flow rate through the glass fiber rib throughout the 24 hour simulations for the spring, summer, fall, and winter.

Moreover, Figure 4.8 indicates that the critical wetting length for the cellulose rib for all 24 hour simulations remained within 27% of its maximum

value of 47 cm, which corresponds to the balance of capillary and hydrostatic pressures. As a result of the relatively constant critical wetting length, the total flow rate was more sensitive to environmental changes than the other two rib types. For example, for July 9, the total flow rate deviated from the average by as much as 106% for the cellulose membrane, whereas the deviation from the average was only 46% and 69% for the PVDF and glass fiber ribs, respectively. Averaged over the four 24 hour simulations, the flow rates through the ribs made of PVDF, glass fiber, and cellulose were 1.5, 7.4, and 6.3 mg/m-s, respectively.

The total evaporative loss rate per footprint area can be a critical parameter for designing and siting PSBRs. Assuming the flow rates through each rib are independent, the water loss rate per footprint area can be calculated by multiplying the evaporative loss rate per rib by the number of ribs per meter. Therefore, decreasing the rib spacing increases the evaporative loss rate per unit area. If a spacing of 10 ribs per meter is assumed, the evaporative loss rate per unit footprint area for the PVDF, glass fiber, and cellulose membranes would be 1.3, 6.4, and 5.4 L/m²-day, respectively. These evaporation rates are comparable to losses from an open biofilm photobioreactor [92].

4.3.5 Reducing evaporative losses without sacrificing productivity

A fortuitous aspect of evaporation driven PSBRs is that the flow rate through the reactor closely follows the daily variation in irradiance. This phenomenon expedites nutrient delivery to the biofilm during the day when
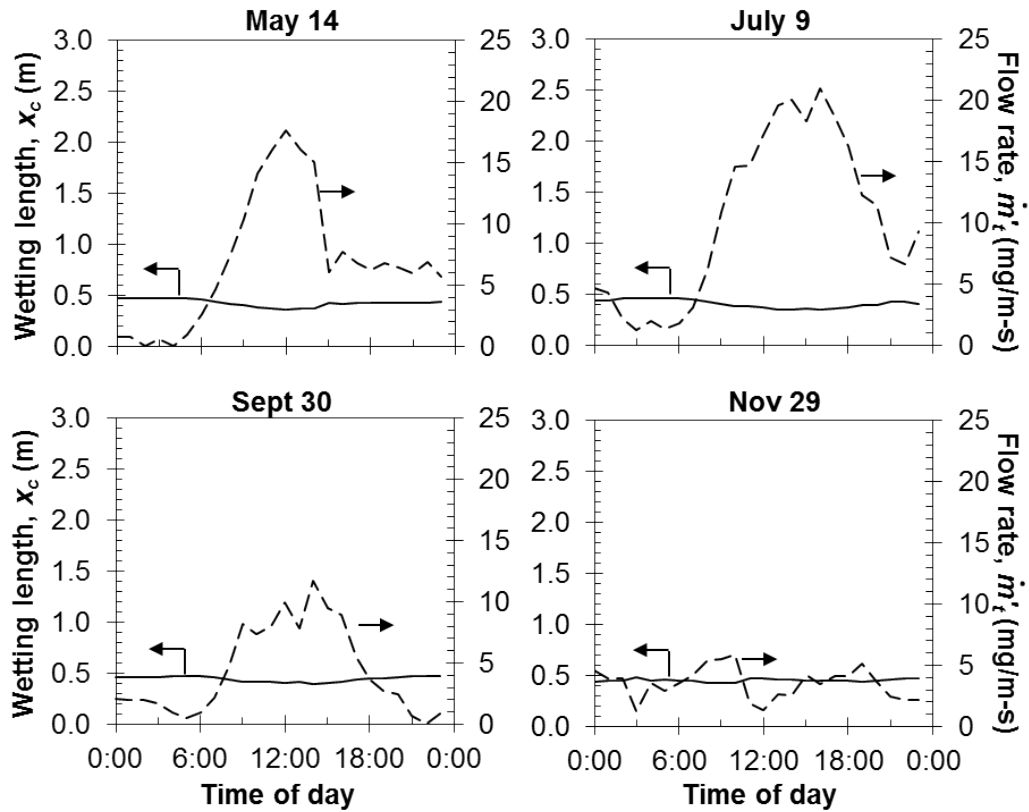
Figure 4.8: Critical wetting length and total flow rate through the cellulose rib throughout the 24 hour simulations for the spring, summer, fall, and winter.

the photon flux is high, while mitigating evaporative losses at night when the photon flux approaches zero. Moreover, the time of day corresponding to the maximum flow rate is the same as the time of day corresponding to the minimum wetting length. Therefore, to enable maximum nutrient fluxes during the day while mitigating evaporative losses at night, the exposed rib length h_e should be equal to the minimum daily critical wetting length.

To demonstrate the effectiveness of this strategy, the flow rate through
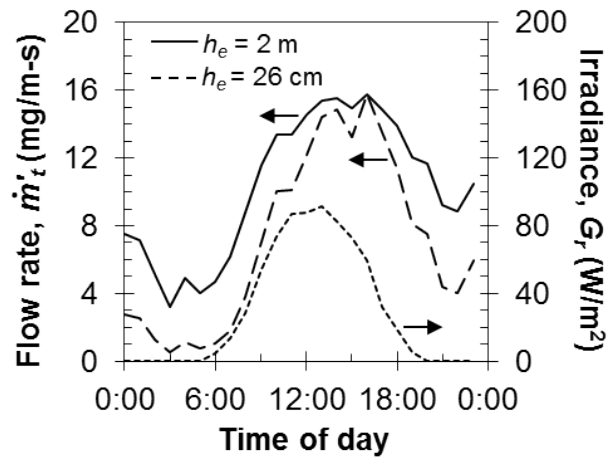
Figure 4.9: Flow rates through glass fiber ribs with exterior heights of 26 cm and 2 m, as well as the irradiance, throughout the day of July 9.

a glass fiber rib with an exterior length equal to 26 cm was calculated for July 9. The length of 26 cm was chosen as it was the minimum wetting length for July 9. Figure 4.9 shows the irradiance and the flow rate over the course of the day. The flow rate through a rib with h_e equal to 2 m, which is greater than the maximum daily critical wetting length, is also shown for comparison. The figure indicates that the flow rate through the short rib was as much as 84% less than the flow rate through the long rib at night when the irradiance was zero. However, between the hours of 10:00 AM to 4:00 PM, the flow rate through the short rib within 25% of the flow rate through the long rib. Thus, the diurnal pattern in nutrient delivery rate closely followed the diurnal patter in photon delivery rate. Finally, the daily evaporative water loss for the long and short ribs were 0.89 L/m-day and 0.61 L/m-day, respectively.

79

4.3.6 Implications for algae cultivation

It was shown in Chapter 3 that the local biofilm growth rate in a PSBR rib declines in the direction of nutrient medium flow as a result of upstream nutrient consumption by the microorganisms. The half growth length $x_{50\%}$, defined as the distance from the nutrient medium reservoir at which the growth rate decreases to half its maximum value, was given in terms of the other system parameters as,

$$x_{50\%} = C \frac{(\dot{m}'_t/\rho)[i_L]_o}{\dot{X}''/Y_{X/i_L}} \tag{4.16}$$

where $\dot{m}'_t$ is the flow rate per unit length (into the page in Figure 4.1), ρ is the mass density of the nutrient medium, assumed to be equal to that of water, $[i_L]_o$ is the concentration of the growth limiting nutrient in fresh nutrient medium, $\dot{X}''_o$ is the areal biomass production rate at the nutrient medium inlet, and Y_{X/i_L} is the biomass yield of the organisms being cultivated with respect to the growth limiting nutrient. Finally, C is a microorganism specific constant.

As an exemplary case, the half growth length was calculated for a glass fiber rib of exposed length 26 cm cultivating the cyanobacterium *Anabaena variabilis* throughout the day of July 9. The areal biomass production rate at the nutrient medium inlet was assumed to be equal to its light-limited value, which was calculated in Chapter 3. It was assumed that the nutrient medium was BG11, in which case the limiting nutrient is phosphate. The phosphate concentration in fresh BG11 and the biomass yield of *A. variabilis* with respect to phosphate are 0.23 mM and 3570 g/mol, respectively. The half

growth length was also calcualted for twice concentrated BG11, in which the phosphate concentration was 0.46 mM.

Figure 4.10 shows the half growth length over the course of the day. For standard BG11, the half growth length using standard BG11 was between 2.8 cm and 5.8 cm at all times except between 5:00 PM and 7:00 PM. Between 5:00 PM and 7:00 PM, the half growth length increased to an average of 12 cm as a result of the relatively high flow rate (about 13 mg/m-s) and low photosynthetic rate as a result of low irradiance (less than 20 W/m^2). For the case of twice concentrated BG11, the half growth lengths doubled and were within the range of 5.6 cm and 11.6 cm at all times except between 5:00 PM and 7:00 PM. The results of this analysis can be used to design PSBRs with half growth lengths that match the physical height of the interior region. In the example of the present case, twice concentrated BG11 should be used as a nutrient medium because it causes the half growth length to be approximately 10 cm, which is the physical height of the interior region.

It is worth noting that the half growth length at all times was less than the exterior rib length. This presents a light transfer problem as the exposed sections can shade the interior biofilm regions in a multi rib system. Concentrated nutrient medium can help to mitigate this issue by increasing the half growth length for a given flow rate. However, concentrated nutrient medium raises concerns regarding (i) changes in fluid surface tension, viscosity, and density, (ii) salt precipitation in the rib, decreasing its permeability, and (iii) adverse effects on biofilm performance resulting from changes in the ionic
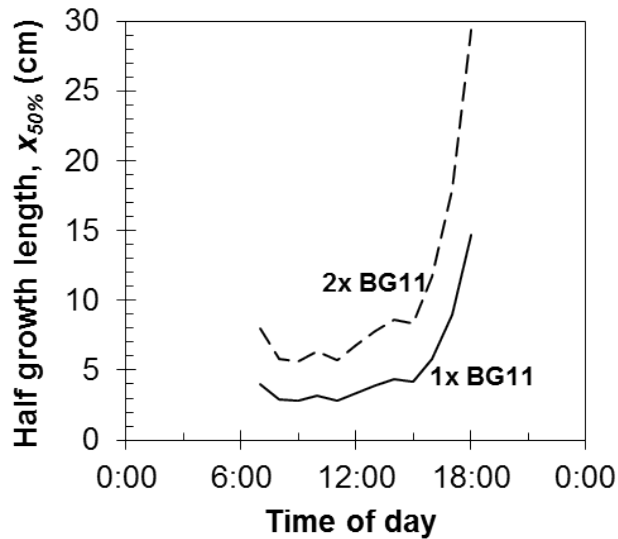
Figure 4.10: Half growth length for a glass fiber rib with a 26 cm exposed length cultivating *A. variabilis* using standard BG11 and twice concentrated BG11 over the course of July 9.

strength and pH of the nutrient medium. Future research should focus on biotic and abiotic effects of using concentrated nutrient media.

Additionally, one criterion that made Memphis a candidate for siting the PSBR was its high annual humidity, which reduces the evaporative losses compared to less humid climates, which can be desirable for operation of conventional open bioreactors. However, because the productivity of evaporation driven PSBRs scales with the evaporation rate, PSBRs are probably better suited for less humid climates, which would increase the flow rate through the ribs while decreasing the critical wetting length. However, less humid climates tend to have fewer water resources than more humid ones, so the relative scarcity of water between different sites should carefully be taken into account.

82

4.4 Conclusions

The flow rate through a rib of an evaporation driven Porous Substrate Bioreactor (PSBR) was calculated as a function of porous material properties and environmental conditions. First, a coupled heat and mass transfer analysis was performed to calculate the expected evaporative fluxes from the rib for a range of expected environmental conditions. Using this range of evaporative fluxes, it was determined that the optimal pore radius in the porous membrane to enable maximum flow rates was between 1 and 10 μm. This optimal size resulted from the competition between increased capillary pressure and decreased permeability with decreasing pore radius. Then, a case study was performed in which the flow rates through three commercially available porous materials were calculated. Four 24 hour simulations were performed for the spring, summer, fall, and winter in Memphis, TN. Averaged over the four 24 hour simulations, the flow rates through the ribs made of PVDF, glass fiber, and cellulose were 1.5, 7.4, and 6.3 mg/m-s, respectively. The glass fiber rib had the greatest flow rate because it was able to provide high capillary pressure (92 kPa) while having relatively high permeability (0.23×10^{-12} m^2). On the other hand, the PVDF and cellulose materials suffered from low permeability and low capillary pressure, respectively. Future studies will focus on the design and construction of an optimal rib with regard to high capillarity and permeability, biocompatibility, as well as ease of manufacturing and durability.

Nomenclature

$D_{w,a}$ diffusivity of water vapor in air, m^2/s
G irradiance, W/m^2
Gr Grashof number
h height, m
h_c convection heat transfer coefficient, W/m^2-K
h_{fg} heat of vaporization, J/kg
k hydraulic permeability of the rib material, m^2
k_ω mass transfer coefficient, kg/m^2-s
$\dot{m}'$ mass flow rate per unit length, kg/s-m
$\dot{m}_e''$ evaporative flux, kg/s-m^2
P pressure, Pa
P_c maximum available capillary pressure, Pa
r pore radius
Re Reynolds number
Sc Schmidt number
Sh Sherwood number
T temperature, K
t rib thickness, m
x distance in the direction of flow, m
x_c critical wetting length, m

Greek symbols
α absorptivity
ϵ void fraction
μ dynamic viscosity, Pa-s
ω mass fraction
ρ mass density, kg/m^3
σ surface tension, N/m
θ contact angle, deg

Subscripts
∞ refers to ambient
a refers to air
e refers to exterior region
f refers to forced convection
i refers to interior region
n refers to natural convection
r refers to rib

Chapter 5

Multispectral Image Analysis for Algal Biomass Quantification

5.1 Introduction

[1]This chapter presents a rapid, non-invasive, and inexpensive multispectral imaging technique for measuring the biomass concentration of algae cultures. The technique uses a conventional RGB camera and a computer code for multispectral image analysis to quantify the areal biomass concentration of both attached and suspended cultivation systems. The large view field of image acquisition enables the technique to be applied for monitoring large scale systems and algae cultivation farms. Moreover, implementation of time lapse quantification of biomass concentration enables real-time productivity monitoring of synthetic leaf biofilms without disturbing the algae.

5.2 Current State of Knowledge

5.2.1 Biomass quantification in suspended cultures

The biomass concentration of suspended cultures is conventionally measured either by direct biomass weighing of a culture sample, or by measure-

---

[1]This is a preprint of an article published in *Biotechnology Progress*, vol. 29, no. 3, pp. 808-816, 2013.

ment of a proxy for biomass, typically optical density or chlorophyll concentration [3]. Dry biomass weighing entails weighing an empty, dry filter, filtering a liquid sample through the filter, drying the sample, and re-weighing it [140]. This method is very simple, but it requires an oven, filter paper, a filtering apparatus, and a scale. Further, the dry biomass concentration of the sample is dependent on the sampling location. Moreover, non-algal microorganisms and salts can be retained in the filtering process and counted as dry biomass, resulting in over-estimation of the algal biomass concentration [140]. Finally, the drying time is usually several hours, thus precluding the possibility of real-time biomass quantification.

Direct measurement of monochromatic optical density is often used as a proxy for biomass concentration [3]. Optical density of a culture is measured at a specific wavelength in a spectrophotometer and correlated to biomass concentration using published calibration curves. However, the accuracy of said correlations is dependent on measurement specifications such as the spectral bandwidth and acceptance angle of the measuring instrument as well as the spectral distribution of the light source [122]. Furthermore, the optical density of the sample can be dependent on sampling location.

Chlorophyll extraction entails centrifuging a sample, resuspending the concentrated sample in a solvent (usually ethanol or methanol), and measuring the optical density of the resulting chlorophyll suspension at specific wavelengths in a spectrophotometer [3]. The chlorophyll concentration is calculated from the optical density using published correlations [79]. This process

can be performed in less than an hour, but it requires solvents, a centrifuge, and a spectrophotometer. Moreover, the accuracy of the results depends on the similarity between the spectral content of the light source and the spectral bandwidth of the measuring instrument and the instrument used in obtaining the published correlations [122].

More recently, Jung and Lee reported a method for using image analysis to measure the biomass concentration of a vertical tubular bioreactor [59]. In their method, a red-green-blue image taken from the top of the reactor was converted to a grayscale image. The average gray value of the grayscale image was then correlated to the biomass concentration. However, in their study, the vertical tubular photobioreactor was illuminated from the sides and imaged from the top. Therefore, the average gray value was dependent on tube diameter, as a culture in a larger diameter tube will appear darker than the same culture in a smaller diameter tube. Additionally, the correlation is also dependent on the spectral content of the light source, as an algae culture illuminated with green light will have a higher average gray value than one illuminated by red or blue light due to selective absorption by the photosynthetic pigments [15]. Moreover, on a large scale, illumination from the top of a culture is logistically more feasible than uniform illumination from all sides.

5.2.2 Biomass quantification of biofilms

Norrman *et al.* presented an electromechanical method for measuring the thickness of a biofilm growing on a metal surface [99]. In this method, the

authors incrementally lowered a needle cathode toward the biofilm surface, and the locations of the air-biofilm interface and biofilm-substrate interface were determined by abrupt changes in the current through the cathode. Although this method is reliable and accurate for laboratory applications, its practicality at photobioreactor scales is a concern.

Additionally, several non-invasive optical methods for measurement of non-photosynthetic biofilm thickness and biomass concentration have been reported [7, 8, 109]. Bakke and Olson presented a method in which a light microscope was focused first on the biofilm-substratum interface and then on the biofilm-liquid interface [8]. The biofilm thickness was recovered from the distance between the two focal planes. Moreover, the same group presented a monochromatic imaging method for measuring biofilms' total organic carbon content per unit area [7]. They grew a biofilm of the non-photosynthetic bacteria *Pseudomonas aeruginosa* in a rectangular duct bioreactor. They then found a linear correlation between the biofilm's total organic carbon per unit area and its optical density at 420 nm. The aforementioned methods can be used to quickly measure biofilm thickness, but they require a transparent substratum and either a microscope or a monochromatic, collimated light source and photometer. Furthermore, photosynthetic biofilms challenge the applicability of these methods because absorption by pigments impedes light transmission through the biofilm.

Kazemipour *et al.* measured the spectral reflectance and transmittance of microphytobenthic biofilms in an effort to determine their biomass concen-

tration using remote hyperspectral imaging [60]. The inherent reflectance and transmittance of simulated biofilms of the diatom *Entomoneis paludosa* were calculated by measuring the apparent reflectances of the biofilms on two backgrounds with different known reflectances. The absorption coefficient at 673 nm, corresponding to absorption by chlorophyll a, was calculated from these parameters and correlated with biomass concentration. The biomass concentration of an independently prepared set of biofilms was predicted with a coefficient of determination R^2 value of 0.93 by measuring the biofilms' apparent reflectance at 673 nm. This method enables non-invasive biomass quantification and is independent of the intensity and spectrum of the light used to illuminate the biofilm. However, the method requires the use of a hyperspectral camera, which can be cost-prohibitive in many applications.

As demonstrated by Jung and Lee, it is possible to recover the biomass concentration of suspended cultures using an inexpensive camera. However, their correlation was specific to the lighting conditions and the geometry of the photobioreactor used, limiting the applicability of this method and the reported correlation in other systems. Thus, imaging methods that can quantify biomass concentration and are independent of the geometry of the photobioreactor and the light source used are needed. Moreover, individually analyzing the red, green, and blue intensities of an algae culture image and comparing them to those of a white reference can eliminate the dependence of the image analysis technique on the spectral content of the light source. This chapter reports a rapid, non-invasive, inexpensive method for determining the biomass

89

concentration of both suspended and attached cultures using wide-band multispectral imaging of reflected and backscattered light.

5.3 Materials and Methods

5.3.1 Stock culture cultivation

The cyanobacteria *Anabaena variabilis* (ATCC 29413-U) was used as an exemplary microorganism due to its widespread use in experimental studies on photobiological CO_2 mitigation and biohydrogen production [14, 43, 131]. *A. variabilis* is a cyanobacteria composed of cells of approximately 5 μm in diameter forming filaments more than 100 μm long [15]. Its cultivation as both suspended and attached cultures have been shown [14, 43]. Also, the pigmentation as well as the optical properties of *A. variabils* have been reported [15, 41]. Optically, the organisms have absorption peaks at 440 nm and 680 nm, corresponding to chlorophyll a, as well as an absorption peak at 620 nm, corresponding to phycocyanin, a light-harvesting phycobiliprotein [15, 41]. In lesser amounts, *A. variabilis* also contains carotenoids, with broad absorption between 400 and 500 nm, and the phycobiliproteins phycoerythrin and allophycocyanin, with absorption peaks at 565 nm and 650 nm, respectively [41]. The stock suspended culture for the experiments was cultivated in BG11 nutrient medium [3], sparged with air containing 2% by volume carbon dioxide, and continuously illuminated with 16 $\pm$ 2 W/m² irradiation (74 $\pm$ 8 μE/m²-s) in the photosynthetically active region (PAR) using cool white fluorescent bulbs (Philips, F32T8).

90

5.3.2 Biofilm preparation and imaging

Two suspended stock cultures, one 5 days old and the other 7 days old, were used to generate the biofilms to evaluate the effect of culture age on image analysis results. For each culture, biofilms of varying thickness were simulated by filtering a known volume of microorganism suspension from the stock culture onto glass fiber filter paper with an average pore diameter of 0.7 μm (Whatman, GF/F) using a vacuum filtration apparatus (Kimax, 27070). The resulting biofilm had a diameter of 3.8 cm. Then, the biofilm was placed into a custom-made illuminated box (photobox) to ensure that each image acquired was subject to the same background and lighting conditions (Figure 5.1). Inside the photobox, the biofilm was illuminated with diffuse light provided by a fluorescent bulb (Underwriters Laboratories, Portable Luminaire) at an irradiance of 4.5 W/m^2 (21 μE/m^2-s). A digital camera with 8 megapixel resolution (Logitech, Pro 9000) was then placed into the camera port of the photobox. The automatic exposure and white balance features were disabled to avoid automatic increases in image brightness as the culture became darker upon addition of microorganisms. The exposure and white balance were set to their minimum values and the gain was set to its maximum value. These settings were selected because they produced the greatest color contrast possible in the image.

After each image acquisition, an incremental volume of suspended stock culture was added to the biofilm by vacuum filtration. This process was repeated until there was no noticeable change in biofilm appearance. It was
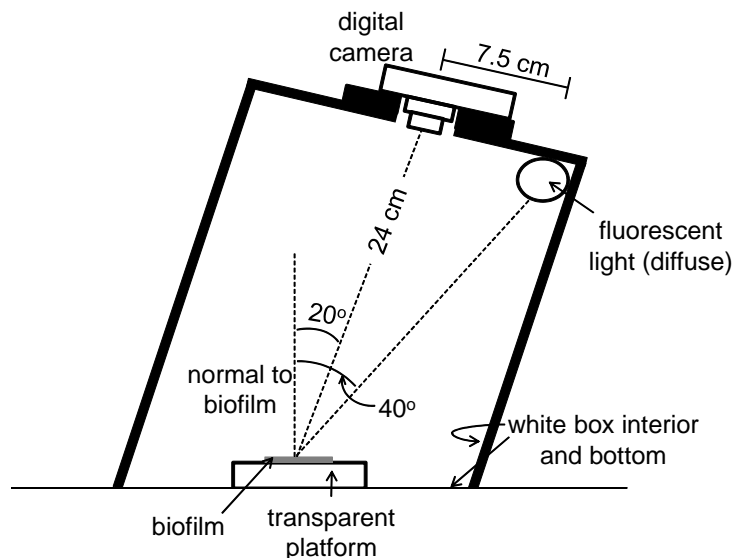
Figure 5.1: Cross-section schematic of the photobox.

ensured that each volume of suspended stock culture filtered onto the paper had the same microorganism concentration by stirring the stock culture prior to each filtration. Given the short duration of the experiments (less than 5 minutes per sample) and the low light levels used (less than 21 μE/m^2-s), no appreciable variations in either the biomass concentration or the optical properties of the cells were expected.

5.3.3 Biofilm thickness and areal biomass concentration

To measure biofilm thickness t, a modified version of the method presented by Norrman $et\ al.$ was used [99]. In this method, a needle electrode was maintained at 2 V bias with respect to the biofilm-supporting filter paper using a SourceMeter (Keithley, 2400) (Figure 5.2a). With the needle electrode

in air, the current through the circuit was at its noise level of approximately 20 pA. The needle electrode was lowered toward the biofilm surface at a rate of 1 μm/s using a 3-axis differential translation stage (Thorlabs, PT3A) and a computer-controlled actuator (Thorlabs, ZST25B and TST001). The needle was lowered until the current through the circuit abruptly increased by four orders of magnitude to approximately 0.1 μA. This signalled the completion of the circuit, and the vertical needle position corresponded to the top of the biofilm. This process was repeated for the non-biofilm-supporting region of filter paper. In this case, the vertical needle position at which the circuit was completed marked the bottom of the biofilm. For a given biofilm, this process was repeated at five biofilm locations to enable calculation of the spatial variance of the biofilm thickness.

Finally, the areal biomass concentration X_A of the biofilms was calculated as the ratio of the dry algal biomass to the biofilm area. For this, the volumetric biomass concentration of the stock culture used in the experiments was determined according the standard methods reported [140]. This was done simultaneously while preparing the biofilms to eliminate the effects of growth. The dry biomass of each biofilm was then calculated by multiplying the volumetric biomass concentration of the suspended stock culture with the volume of culture used to make the biofilm.
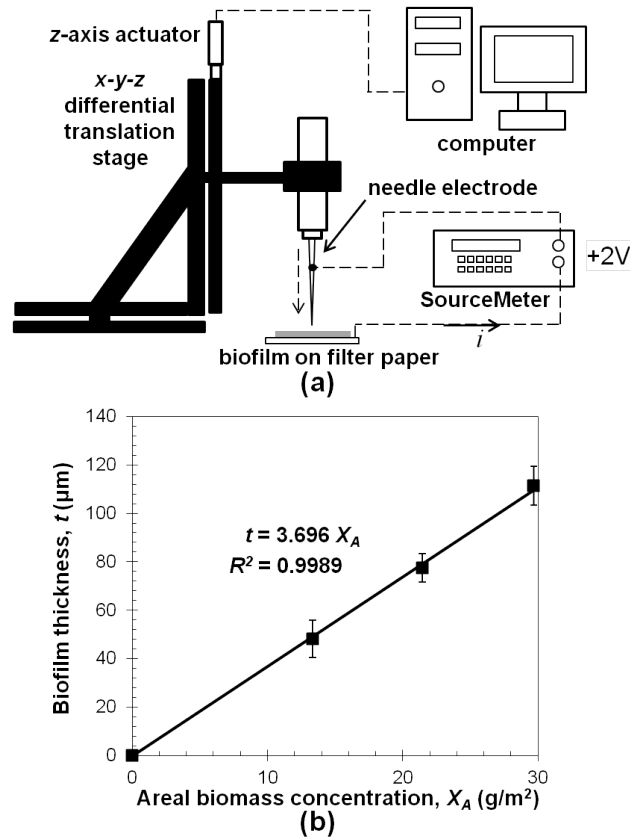
Figure 5.2: (a) Schematic of the experimental setup used for measuring biofilm thickness and (b) biofilm thickness versus areal biomass concentration.

5.3.4 Suspended culture preparation and imaging

The chamber for holding suspended cultures was a custom built acrylic box that measured 10.0 cm x 6.4 cm x 8.1 cm in length, width, and height, respectively. The top of the box was open to create a top-irradiated illumination scheme typical of scaled-up open raceway ponds and the sides were covered with white paper to impose symmetry boundary conditions. Cultures of different biomass concentrations having a total volume of 400 mL were placed in

94

the acrylic box and imaged. The concentration of the culture in the acrylic box was measured by filtering a known volume onto filter paper, drying, and weighing.

5.3.5 Image analysis

A custom Matlab code was developed to analyze the images of the algal cultures. Each pixel of a digital image acquired by the camera is represented by the color vector $\vec{c_p}$ equal to $[r_p,g_p,b_p]$, corresponding to the pixel's red (560 to 700 nm), green (490 to 590 nm), and blue (410 to 500 nm) intensities, respectively [107]. Each element of the vector $[r_p,g_p,b_p]$ has an integer value between 0 and 255, inclusive. First, a region of the image containing only the algal culture (green region) was identified. The raw color vector of the green region $\vec{c_o}$ equal to $[r_o,g_o,b_o]$ was then calculated as the average of the red, green, and blue intensities of all the pixels in the region. Then, a region of the image that contained a white reference background was identified. The biofilm-supporting filter paper and the white sides covering the acrylic box were used as the white reference regions for the images of the attached and suspended cultures, respectively. The color vector of the white reference region $\vec{c_w}$ equal to $[r_w,g_w,b_w]$ was calculated as the average of the red, green, and blue intensities of all the pixels in the region. The elements of the normalized color vector $\vec{c}$ used in the analysis were calculated by dividing each raw color intensity by the intensity of that color in the white region to account for differences in the intensity and spectral content of the light source:

$$\vec{c}(i) = \vec{c_o}(i)/\vec{c_w}(i) \quad \text{for } i = 1, 2, 3 \tag{5.1}$$

5.4 Results and Discussion

5.4.1 Relationship between biofilm thickness and areal biomass concentration

Figure 5.2b shows the relationship between the areal biomass concentration and the biofilm thickness. A linear relationship was recovered using the electromechanical method. The thickness t is given in terms of areal concentration X_A as, $t = 3.696 \ X_A$, where t is in μm and X_A is in g/m^2. The coefficient of determination R^2 for this fit was 0.9989. Using these results, it was established that the volumetric microorganism concentration in the biofilm was 271 kilograms dry biomass per cubic meter (kg DW/m^3).

5.4.2 Attenuation of red, green, and blue light in the algal cultures

Figure 5.3 shows the normalized red, green, and blue intensities (r, g, and b) of attached and suspended cultures as a function of areal biomass concentration. The magnitude of each color intensity of a given image is a result of the combined effects of reflection from the culture surface and back-scattering from within the culture. The intensity of the back-scattered light is governed by the radiative transport equation (RTE), which takes into account absorption and anisotropic scattering by the microorganisms and the medium [16, 118]. Solving the RTE for the backscattered intensity from dense cultures poses a challenge as scattering phenomena gets into dependent regime

where the radiative properties of the culture can no longer be described as linear functions of microorganism concentration [16]. Therefore, this analysis seeks an empirical correlation between areal biomass concentration and color intensity, taking into account reflected and back-scattered light from the culture. The equation form for the empirical model has been formulated by modeling light transfer through the algae culture with ray tracing analysis [60] and is given by,

$$\vec{c}(i) = \vec{\alpha}(i) + \vec{\beta}(i)e^{-2X_A E_{p,ext}(i)} \tag{5.2}$$

where the vector $\vec{\alpha}$ represents the reflected intensity from the surface of the culture, and is assumed to be independent of biomass concentration based on the results presented by Kazemipour et al [60]. Moreover, the vector $\vec{\beta}$ represents the reflectance of the bottom surface of the algae culture. The vector $\overrightarrow{E_{p,ext}}$ contains the pseudo-mass extinction cross sections for red (i=1), green (i=2), and blue (i=3) light, which control the attenuation of irradiance of each color along the ray path.
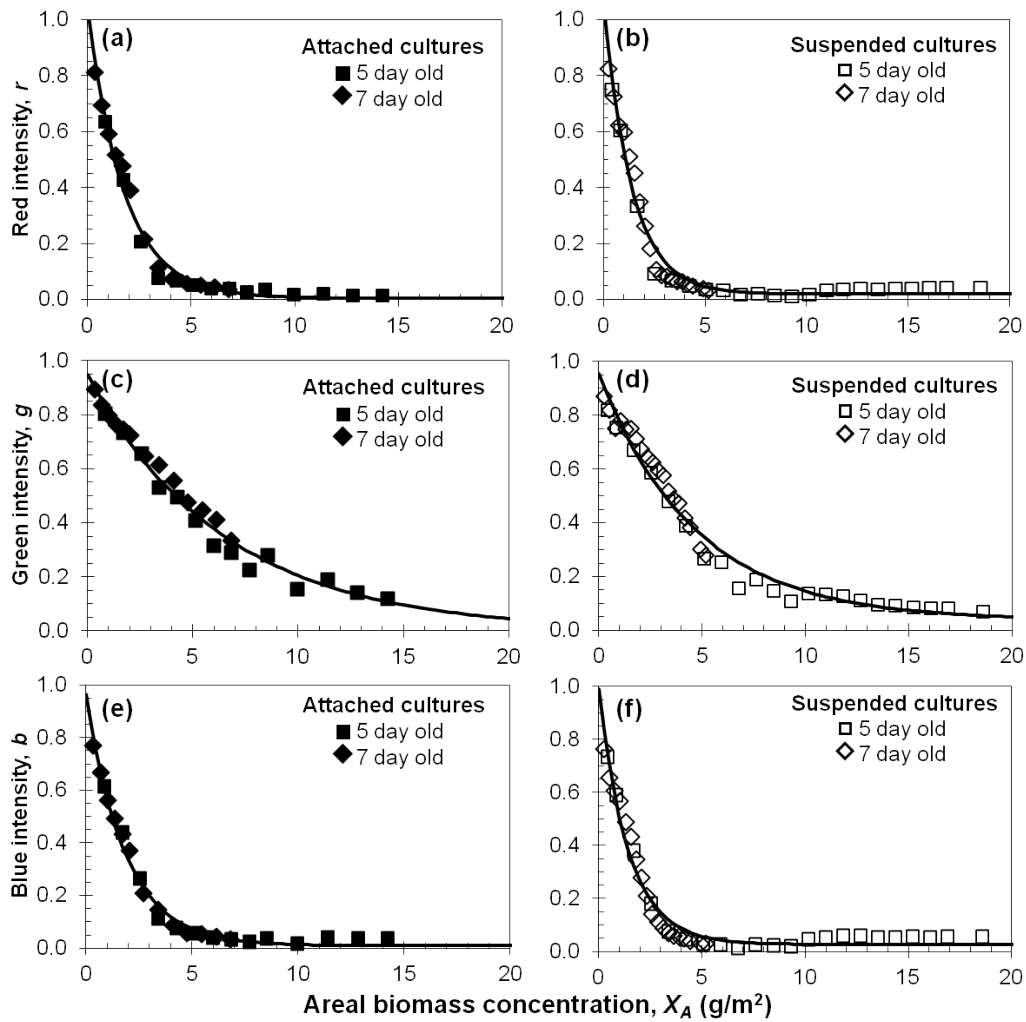
Figure 5.3: Normalized color intensity as a function of areal biomass concentration for attached and suspended cultures at two culture ages for (a,b) red, (c,d) green, and (e,f) blue.

The experimental data shown in Figure 5.3 was fitted with Equation (5.2) using the linear least squares method [53]. Table 5.1 summarizes the values of $\vec{\alpha}$, $\vec{\beta}$, and $\overrightarrow{E_{p,ext}}$, as well as the R^2 value for each fit. All R^2 values

obtained were greater than 0.97. The wide-band pseudo-extinction cross sections of the red and blue bands were approximately equal to each other and greater than that for the green band by a factor of about 3.5. The more gradual attenuation of backscattered green light compared to red and blue light is a result of the relatively low absorptivity of *A. variabilis* at wavelengths between 490 and 590 nm, which is in turn a result of the organisms' lack of photosynthetic pigments that absorb light in that wavelength range [15, 41]. Moreover, the pseudo-extinction cross sections for the suspended cultures were greater than those for the attached ones by an average of 35%. This can be attributed to (i) light absorption by the liquid medium of the suspended culture and (ii) dependent scattering in the biofilm, decreasing its absorptivity compared to an independent scattering medium [118].

Table 5.1: The curve fit parameters α and β, wide-band pseudo-mass extinction cross sections $E_{p,ext}$, and coefficient of determination R^2 for fitting Equation (5.2) to the experimental data.

	Red band 560-700 nm		Green band 490-590 nm		Blue band 410-500 nm	
	Attached	Suspended	Attached	Suspended	Attached	Suspended
α	0.0046	0.019	0.0016	0.038	0.0094	0.026
β	1.03	1.05	0.919	0.915	0.956	0.963
$E_{p,ext}$ (m^2/g)	0.281	0.365	0.077	0.107	0.2688	0.346
R^2	0.984	0.974	0.981	0.977	0.989	0.972

Furthermore, in both cultures, the color intensities at areal biomass concentrations greater than 10 g/m^2 were greater than their respective intensities at areal biomass concentrations between 8 and 10 g/m^2 by approximately 0.02. This trend is especially clear for the red and blue intensities of the suspended

cultures. This trend can be attributed to the increase in back-scattering that resulted from multiple scattering by organisms in a thin layer below the illuminated surface at higher concentrations. Finally, the components of the vector $\vec{\alpha}$ were greater for the suspended cultures than for the attached ones by a factor of about 5, indicative of the greater surface reflectivity of water compared to a microorganism film layer [60, 118].

The rate at which light energy is converted to chemical energy in photosynthetic systems is a function of the wavelength, known as the photosynthetic action spectrum, as well as the local irradiance [78]. Thus, knowledge of spectral light attenuation within a culture can provide valuable information about the overall productivity of that system. Particularly, the local productivity in *A. variabilis* cultures is highly dependent on the availability of red light as its photosynthetic action spectrum indicates one predominant peak at a center wavelength of 633 nm and a half width at half maximum of 37 nm [78, 84]. Therefore, using the wide-band red pseudo-extinction cross section obtained in this study, we can illustrate the areal biomass concentration, $X_{A,f}$, for *A. variabilis* at which the local red irradiance drops to 10%, 1%, and 0.1% of its value incident on the culture as,

$$X_{A,f} = -ln(f)/E_{p,ext}(red) \tag{5.3}$$

where f represents the attenuation fraction. In this analysis, it is assumed that the culture density is such that all red irradiance is absorbed before reaching

the back surface. Table 5.2 presents the areal biomass concentrations at which the wide-band red irradiance is attenuated to 10%, 1%, and 0.1% of its incident value within attached and suspended cultures of *A. variabilis*. The table also shows the associated biofilm thicknesses and suspended photobioreactor depths that correspond to these concentrations, assuming attached and suspended volumetric microorganism concentrations of 271 kg/m^3 and 500 g/m^3, respectively [21].

Table 5.2: Areal biomass concentration ($X_{A,f}$), biofilm thickness (z_a), and suspended culture physical depth (z_s) at which the wide-band red irradiance is attenuated to 10%, 1%, and 0.1% of its value at the light-facing side of the culture, assuming attached and suspended volumetric microorganism concentrations of 271 kg/m^3 and 500 g/m^3, respectively.

| | Attached cultures | | Suspended cultures | |
f	$X_{A,f}$ (g/m^2)	z_a (m)	$X_{A,f}$ (g/m^2)	z_s (m)
10%	8.2	3.0×10^{-5}	6.3	0.013
1%	16.4	6.1×10^{-5}	12.6	0.025
0.1%	24.6	9.1×10^{-5}	18.9	0.038

5.4.3 Correlation between normalized green intensity and areal biomass concentration

The normalized green intensity displayed more gradual attenuation with increasing biomass concentration than the red and blue intensities. Therefore, the normalized green intensity was identified as the appropriate value to correlate to areal biomass concentration because such a correlation would be accurate within a larger range of concentrations. For attached cultures, rearranging Equation (5.2) and using the coefficient values from Table 5.1 yields,

$$X_A = -6.49 ln \left(\frac{g - 0.0016}{0.947} \right) \qquad (5.4)$$

Equation (5.4) is recommended for areal biomass concentrations between 0.34 and 14 g/m^2, which was the range of areal biomass concentrations examined in this study. Similarly, for suspended cultures:

$$X_A = -4.69 ln \left(\frac{g - 0.0375}{0.915} \right) \qquad (5.5)$$

Equation (5.5) is recommended for areal biomass concentrations between 0.25 and 21 g/m^2.

It is worth noting that the coefficients in Equations (5.4) and (5.5) are dependent on the cellular pigment concentrations. It is well known that cells can up- or down-regulate their pigment contents depending on cultivation conditions [42]. However, it is possible to re-establish the pigment-biomass correlation as necessary to account for these effects.

5.4.4 Validity of the correlation under different lighting conditions and backgrounds

To take full advantage of this biomass quantification method, it must be insensitive to the magnitude, spectral content, and angle of incidence of the irradiance onto the culture, as well as to the spectral reflectance of the background surrounding the culture. Therefore, the accuracies of Equations (5.4) and (5.5) were measured on independently prepared sets of attached and

suspended culture images acquired using combinations of three different light sources and two different backgrounds. The three light sources used were the fluorescent lamp of the photobox, fluorescent room lighting, and shaded diffuse solar illumination. The hemispherical photosynthetically active radiation (PAR; from 400 to 700 nm) for the photobox, room, and sunlight were measured with a quantum sensor (Li-Cor, LH-100) to be 4.5 W/m^2 (21 μE/m^2-s), 1.3 W/m^2 (6.0 μE/m^2-s), and 1.6 W/m^2 (7.4 μE/m^2-s), respectively. The normalized spectral intensities of the three light sources are shown in Figure 5.4. The spectra of the two fluorescent bulbs were measured using a monochromator (Newport, Cornerstone 260) with 3.7 nm spectral resolution, while the diffuse solar spectrum was reported by Gueymard *et al.* [49]. The two backgrounds were white paper (OfficeMax, Copy Paper) and black epoxy resin lab bench surface (VWR). Black and white materials were selected as backgrounds because the total reflectance in the visible range of any other color material will be between those of these two extremes.

Figure 5.5a shows digital images acquired of the benthic cultures at an areal biomass concentration of 7.8 g/m^2. The color and brightness of each biofilm appears different to the naked eye due to the variations in the magnitude and spectral content of the incident irradiance. Figure 5.5b indicates that the benthic culture areal biomass concentration was predicted well by Equation (5.4) under all six lighting conditions. Moreover, Table 5.3 shows the RMSD between the areal biomass density predicted by Equation (5.4) and the actual biomass density for each of the six conditions. For the case of photobox

103
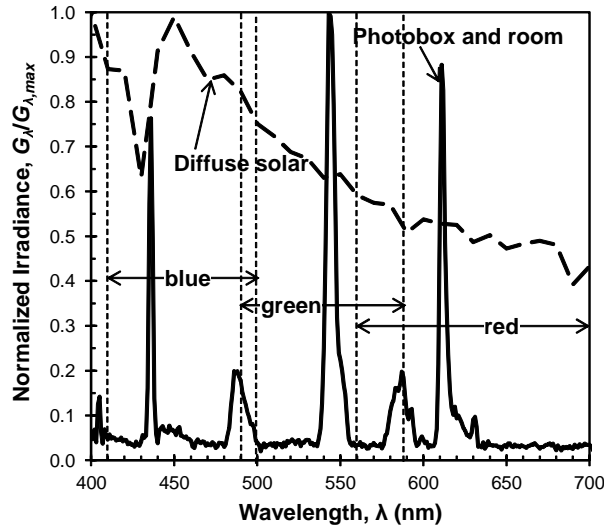
Figure 5.4: Normalized spectral intensities of the three light sources used for image acquisition, along with the wavelength bands of the color filters of the RGB camera [49, 107].

lighting with white background, which served as the validation data set, the RMSD was 0.67 g/m^2, which corresponds to an average error of 6.5%. The RMSD was highest for solar illumination with black background and room illumination with black background. The average percent error incurred in using Equation (5.4) to predict areal biomass density across all six lighting and background scenarios was 25%. Similarly, Figure 5.5c shows the digital images acquired of the planktonic cultures at areal biomass concentration of 6.1 g/m^2. Figure 5.5d shows the areal biomass concentration as a function of normalized green intensity for these cultres, as well as the areal biomass concentration predicted by Equation (5.5). Moreover, Table 5.4 shows the RMSD between the areal biomass density predicted by Equation (5.5) and the actual biomass

density for each of the six conditions. For the case of photobox lighting with white background, which serves as the validation data set, the RMSD was 1.64 g/m^2, which corresponds to an average error of 15%. The RMSD was highest for solar illumination with both white and black backgrounds. The average percent error incurred in using Equation (5.5) to predict areal biomass density across all lighting and background combinations was 21%.

Table 5.3: Root mean square deviation (RMSD) between the areal biomass concentration predicted by Equation (5.4) and the actual areal biomass concentration for the six lighting and background scenarios for the attached cultures.

Light source	Background	RMSD for X_A less than 10 g/m^2 (g/m^2)	RMSD for X_A greater than 10 g/m^2 (g/m^2)
Photobox	White	0.62	0.80
Photobox	Black	0.30	2.10
Room	White	0.72	0.34
Room	Black	2.10	3.39
Solar	White	0.58	1.98
Solar	Black	2.57	2.78

Table 5.4: Root mean square deviation (RMSD) between the areal biomass concentration predicted by Equation (5.5) and the actual areal biomass concentration for the six lighting and background scenarios for the suspended cultures.

Light source	Background	RMSD for X_A less than 10 g/m^2 (g/m^2)	RMSD for X_A greater than 10 g/m^2 (g/m^2)
Photobox	White	0.73	2.21
Photobox	Black	1.47	4.09
Room	White	0.92	1.09
Room	Black	0.32	1.26
Solar	White	2.41	3.21
Solar	Black	2.00	2.91

Although the traditional methods can provide more accurate results,
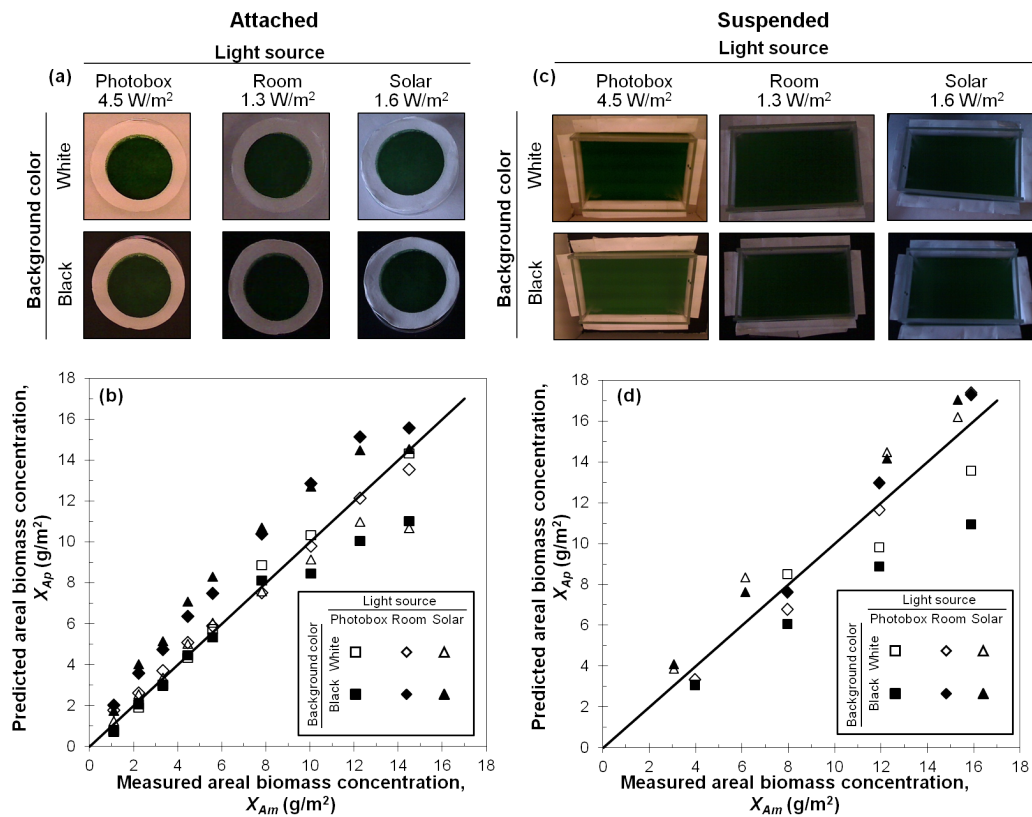
Figure 5.5: Top: digital images of an (a) attached culture at 7.8 g/m^2 and (c) suspended culture at 6.1 g/m^2 under the six lighting and background combinations. Bottom: predicted areal biomass concentration plotted against measured areal biomass concentration for (b) attached and (d) suspended cultures under the six background and lighting combinations.

they can take long analysis time and/or be highly sampling location-specific as explained previously. Thus, the temporal and spatial variations in biomass concentration in cultivation systems can blur the accuracy advantage of these more traditional methods with respect to the method presented here. Moreover, in this study, the lighting and background conditions have been identified

that minimize the prediction errors. Thus, in practical implementation of the presented method care can be taken to stay in these higher accuracy regimes.

5.5 Conclusions

This chapter reported a rapid, non-invasive method of biomass quantification in suspended and attached algae cultures using only a simple RGB camera and custom image analysis software. By parsing images of *Anabaena variabilis* cultures into their red, green, and blue components and correlating the green intensity with biomass concentration, the biomass concentrations of independently prepared cultures imaged under a variety of lighting and background conditions were predicted with an average error of 23%. Future work will focus on evaluating the performance of this technique in outdoor photobioreactors, as well as performing time lapse image acquisition for productivity monitoring.

Nomenclature

b	blue intensity of an image
$\vec{c}$	color vector containing the elements r, g, and b
$\overrightarrow{E_{p,ext}}$	vector containing wide-band pseudo-mass extinction cross sections, m^2/g
f	fraction of local irradiance to incident irradiance
G	irradiance, W/m^2
g	green intensity of an image
r	red intensity of an image
R^2	coefficient of determination
t	biofilm thickness, μm
X_A	areal biomass concentration, grams dry weight (g DW)/m^2
z	culture depth, m

Greek symbols

α	coefficient for curve fit in Equation (5.2)
β	coefficients for curve fit in Equation (5.2)
λ	wavelength, nm

Subscripts

o	refers to raw color vector
p	refers to pixel
w	refers to white region

Abbreviations

PAR	photosynthetically active radiation
$RMSD$	root mean square deviation

Chapter 6

Designing synthetic leaves for algal biomass generation and secreted product harvesting

6.1 Introduction

This chapter presents an experimental study on the performance of synthetic leaves with respect to nutrient medium flow rate, biomass production rate, photosynthetic health, and secreted product harvesting. The biotic leaves consisted of a mutant strain of *Synechococcus* sp. that has been engineered to secrete lauric acid. Cultivating these organisms and passively harvesting the desired bioproducts is critical for producing energy positive, next generation biofuels.

6.2 Materials and Methods

6.2.1 Microorganism and nutrient medium

The cyanobacterium *Synechococcus* sp. $\Delta fadD^{C12}$ was obtained from Victoria Work at the laboratory of Dr. Matthew Posewitz at the Colorado School of Mines. *Synechococcus* sp. $\Delta fadD^{C12}$ is a genetic mutant of the planktonic marine *Synechococcus* sp. (PCC 7002) which has been engineered to secrete the free fatty acid (FFA) lauric acid, which can be used as a biofuel feedstock. Figure 6.1 shows a transmission electron microscope (TEM)

image of the organism, which has a spheroid shape with major and minor diameters of about 1.6 μm and 1.1 μm, respectively. The organisms were cultivated autotrophically in the A+ nutrient medium as planktonic cultures before inoculation of the biofilms. [125]
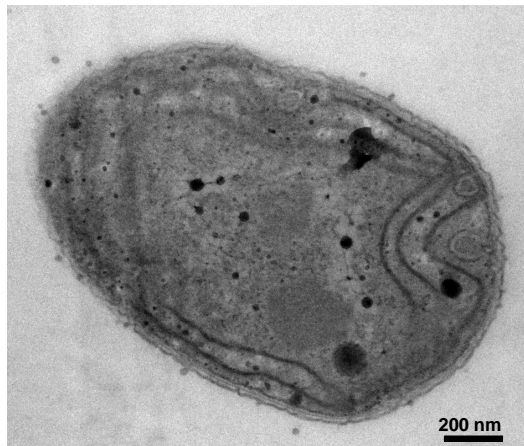
Figure 6.1: Transmission electron microscope (TEM) image of the mutant *Synechococcus* sp. $\Delta fadD^{C12}$.

6.2.2 Cultivation platform

Figure 6.2 shows the schematic of the experimental setup used in this study. *Synechococcus* sp. $\Delta fadD^{C12}$ was cultivated as a biofilm on the porous medium. One end of the porous medium was in contact with the nutrient medium reservoir and the other end was in contact with a terminal end. Evaporation from the terminal end drove nutrient medium flow through the porous medium. The terminal evaporative end served as a collector and concentrator for the secreted products and unused salts from the nutrient medium.
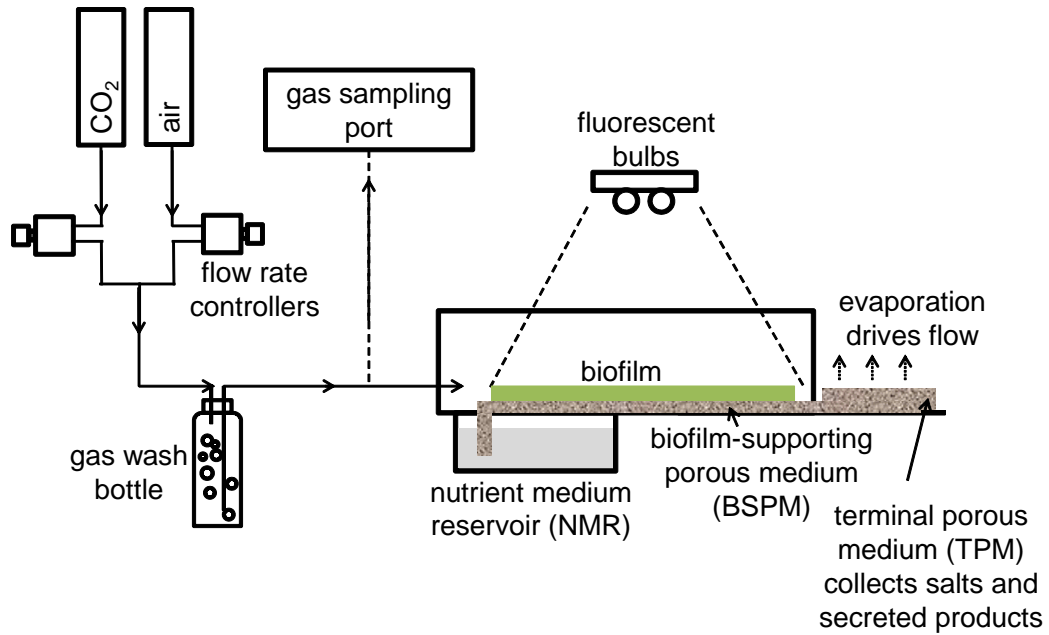
Figure 6.2: Schematic of the experimental setup.

In the current study, hydrophilic polyvinylidene fluoride (PVDF) membrane with a particle retention size of 0.65 μm and thickness of 80 μm was used as the material for porous medium and terminal end (Millipore, DVP00010). Figure 6.3 shows a scanning electron microscope (SEM) image of the membrane material. The porous medium was 6.4 cm long and 1.3 cm wide and was inoculated at an areal biomass concetration of 2.3 mg/m^2 over an area of 1.5 by 1.3 cm. The terminal end was 1.5 cm long and 1.3 cm wide. Air at 23.5 $\pm$ 1°C saturated with water vapor was delivered to the chamber. The CO_2 concentration of the inlet gas was measured with a gas chromatograph (Shimadzu, GC-2014A) to be 0.35 $\pm$ 0.05% by volume. Light was provided by two cool white fluorescent bulbs (Philips, color temperature 4100 K). The

111

irradiance onto the biofilms was measured with a quantum sensor (Li-Cor, LI-190) to be 110 ± 5 μE/m^2-s in the photosynthetically active region (PAR).
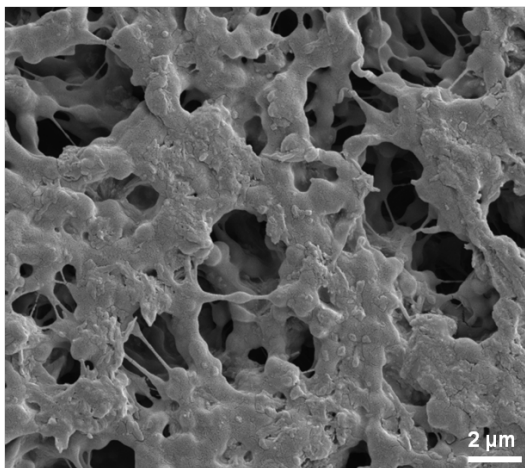
Figure 6.3: Scanning electron microscope (SEM) image of the PVDF membrane used as the porous substrate.

6.2.3   Performance monitoring

The performance of the synthetic leaf was quantified by measuring the photosynthetic yield, growth rate, and free fatty acid (FFA) production rate. These performance parameters were further reported as funcitons of nutrient delivery rate.

6.2.3.1   Nutrient medium delivery rate

The rate at which nutrient medium flowed through the reactor was measured by quantifying the change in the weight of the nutrient medium reservoir as a function of time. This was accomplished by weighing the nutrient

medium reservoir on an analytical mass balance (Mettler-Toledo, AB204/S-FACT) at the beginning and at the end of a known time period.

6.2.3.2 Photosynthetic yield

The quantum yield of photosystem II (YII) was measured using a pulse-amplitude-modulated (PAM) fluorometer (Walz, JUNIOR-PAM). The quantum yield of photosystem II was calculated as [24, 44],

$$Y(II) = \frac{F_m - F_o}{F_m} \qquad (6.1)$$

where F_o is the baseline fluorescence from the culture and F_m is its maximum fluorescence after being exposed to a saturating pulse. The photosynthetic yield signifies the efficiency of energy conversion from the incident light energy to the generation of short term energy carriers ATP and NADPH.

6.2.3.3 Biomass production rate

The areal biomass concentration was measured remotely using the technique presented by Murphy *et al.* [94]. According to this technique, a calibration data set was generated by imaging biofilms of known areal biomass density with a conventional RGB camera. The images were then parsed into their red, green, and blue components. Each component was then normalized against its respective value in a region of the image containing only the white porous medium. The calibration data set was generated using the same lighting and background conditions as the experimental setup. It should be noted that

this technique neglects changes in pigmentation between the cells used for the calibration data set and those in the experimental setup. However, because the nutrient medium composition and average culture irradiance were approximately equal for both data sets, errors incurred using this method are assumed to be small.

Figure 6.4 shows the areal biomass density X_A as a function of the normalized green value g for the calibration data set. A linear least squares regression line was fitted to the data with an R^2 value of 0.97, resulting in the correlation,

$$X_A = 35.10 - 39.53g \tag{6.2}$$
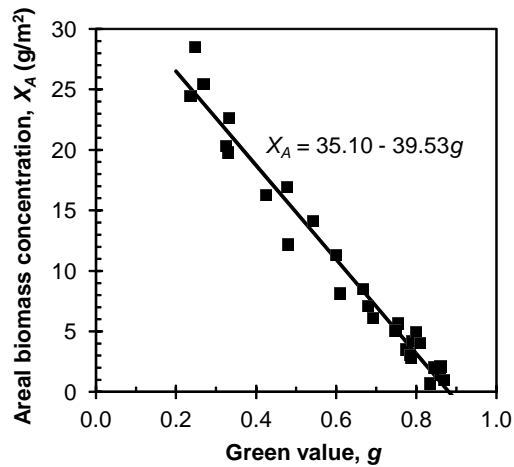
Figure 6.4: Calibration data set for measuring the biomass density remotely using the multispectral imaging method.

Digital images of the actively growing biofilms were then recorded at intervals

of approximately 24 hours. The areal biomass production rate $\dot{X}_A$ between times t_1 and t_2 was defined as,

$$\dot{X}_A = \frac{X_A(t_2) - X_A(t_1)}{\Delta t} \tag{6.3}$$

6.2.4 Free fatty acid (FFA) harvesting rate

A Bligh-Dyer extraction [20] was performed to extract the free fatty acid from (i) the terminal ends, (ii) the porous medium that supported biofilm growth, and (iii) the biofilm itself. The resultant sample containing the FFA was then analyzed using thin layer chromatography (TLC). The TLC plate measured 8 cm long and 6 cm wide with a silica gel layer 15 μm thick and a medium pore diameter of 6 nm, and an 80:20:1 hexane:diethyl ether:acetic acid mixture was used as the carrier phase. A chloroform sample containing 1 μg/μl lauric acid was used as a calibration standard. To visualize the lipids, phosphomolybdic acid was sprayed onto the TLC plate, followed by heating at 240°C for 5 minutes. Lipids were visualized as gray streaks on a green background. The gray scale values of the streaks were measured using a custom image processing code, and the gray scale value was correlated to the FFA content using the calibration standard.

6.3 Results

6.3.1 Nutrient medium flow rate

Figures 6.5a and 6.5b show the nutrient medium flow rate Q through the three reactors and relative humidity surrounding the terminal ends, respectively, over the cultivation period. The temperature of the air surrounding the terminal end was maintained at 23 ± 1°C. The figure indicates first that the nutrient medium flow rates through the reactors were inversely related to the ambient relative humidity, and second that the flow rates decreased over time. The dependence on relative humidity was expected as flow through the reactor is driven by evaporation from the terminal end. In future experiments, forced convection can be used to increase the evaporation rate from the terminal end, thereby increasing the flow rate through the reactor.

Furthermore, a least squares regression line was fitted to the flow rates over time, resulting in the relationship $Q = 28.7 - 0.034t$, where Q is in μl/h and t is in hours. This relationship predicts that the flow rate will be zero at a time of 865 hours, or about 36 days. The temporal decline in the flow rates is attributed to microorganism growth within the porous substrate, providing additional resistance to flow. The PVDF membrane featured some pore diameters larger than the major diameters of the microorganisms, thus enabling colonization of the void space of the membrane. This issue can be mitigated in future experiments by using a porous substrate with a maximum pore diameter smaller than the minimum microorganism diameter. Alternatively, as demonstrated by Naumann *et al.*, a fine porous substrate can be placed be-

116
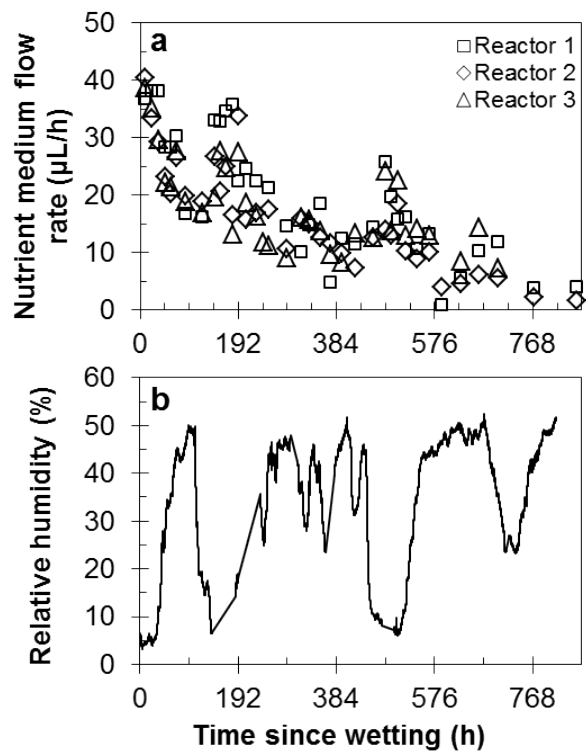
Figure 6.5: (a) Nutrient medium flow rates through the three reactors and (b) relative humidity of the air surrounding the terminal end.

tween a coarse porous substrate and the biofilm. The fine porous substrate can enable nutrient diffusion and microorganism growth, while the bulk nutrient medium flow occurs in the coarse, hydraulically permeable membrane.

6.3.2 Biofilm growth

Figure 6.6 shows a time sequence of biofilm images and the local biomass density in Reactor 3 at times of 103 hours, 216 hours, and 500 hours from inoculation. It indicates that the growth rate was inversely proportional to the

117

distance from the nutrient medium reservoir, which is primarily a result of the consumption of nutrients along the nutrient medium flow path. Moreover, the biofilm expanded toward the nutrient medium reservoir, but not in the other direction, which can also be attributed to the gradient in nutrient concentrations. Similar behavior was observed in Reactors 1 and 2.
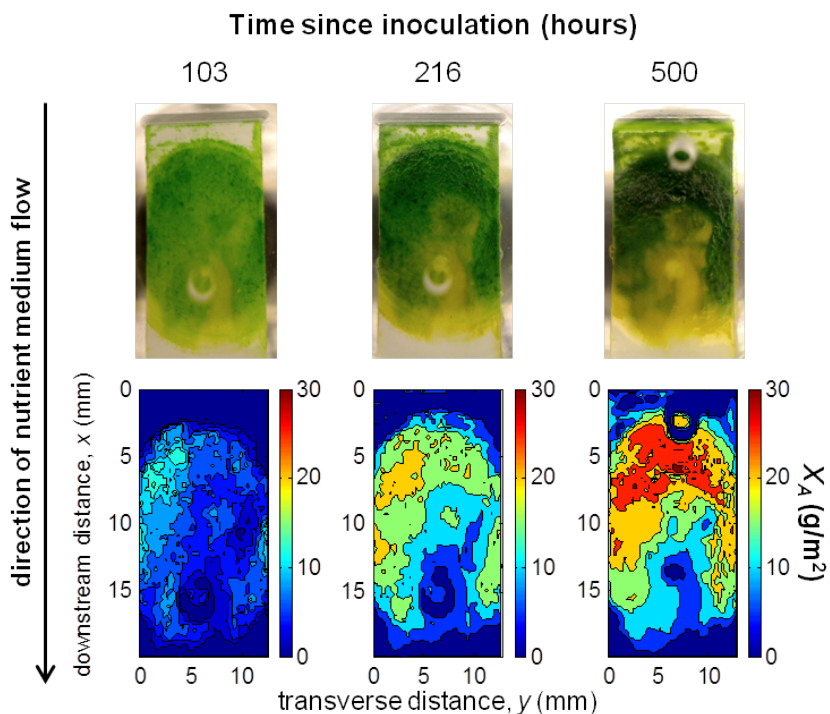
Figure 6.6: Images and local biomass density of the biofilm in Reactor 3 at three different times.

Additionally, Figure 6.7 shows the average areal biomass density in each of the three reactors over the cultivation period. The maximum areal biomass production rate was approximately 0.07 g/m^2-h and it occurred between hours 44 and 144. At a time of approximately 300 hours, the biomass production

118

rate approached zero, which is attributed to inadequate nutrient delivery. This inadequate delivery was caused by two factors. First, the nutrient medium flow rate declined at a rate of approximately 0.034 μl/h^2 over the course of the cultivation period. Second, at times greater than 300 hours, a microorganism colony was observed on the vertical porous medium region between the original horizontal growth region and the nutrient medium reservoir. As this new colony consumed nutrients, it decreased the nutrient concentrations of the medium flowing past the cells in the original growth region. Growth in the new colony was not detectable as it was not in view of the camera. In future experiments, this colonization can be avoided by placing a molecular sieve with a pore size much smaller than the organism diameter between the growth region and the region where colonization is undesirable.

The maximum biomass production rate of 0.07 g/m^2-h enables estimates of the productivity of a scaled up system. As demonstrated in previous Porous Substrate Bioreactor studies, it is often advantageous to dilute the incident irradiance by employing multiple parallel vertical units rather than a single horizontal unit [71, 93, 97]. In the present study, an irradiance of 110 μE/m^2-s was used. Between the months of June through September in Austin, TX, the average photosynthetically active global horizontal irradiance during daylight hours is approximately 707 μE/m^2-s. Therefore, an irradiance of 110 μE/m^2-s corresponds to a light dilution ratio of 6.4, and 6.4 m^2 of biofilm surface area can be placed on a 1 m^2 footprint. Assuming an average day length of 13 hours during this span of months, the scaled up system can produce

119
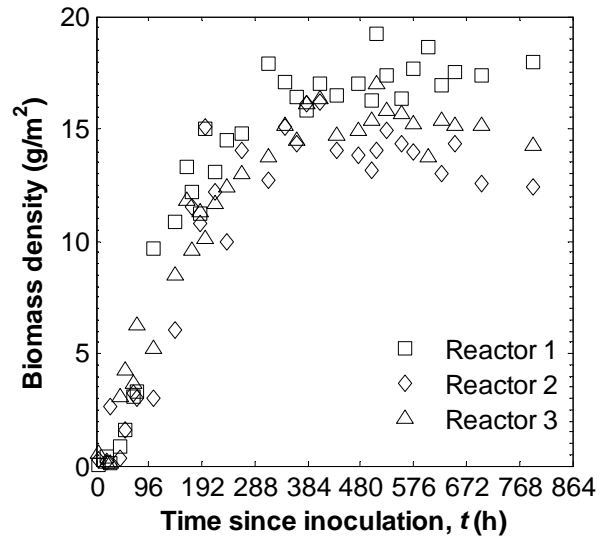
Figure 6.7: Areal biomass density of the three biofilms over the cultivation period.

about 5.8 grams of biomass per square meter of footprint area per day. By comparison, raceway ponds and planktonic photobioreactors have characteristic productivities ranging from 11 to 27 g/m^2-day [58]. Enhanced nutrient delivery is key to optimizing Porous Substrate Bioreactors to approach productivities of conventional systems.

Figure 6.8 shows the yield of photosystem II (YII) of the three biofilms over the cultivation period. The yield decreased from an initial value of about 0.35 to about 0.2 after the 864 hour cultivation period. The temporal decline in Y(II) was qualitatively similar to the temporal decline in the nutrient medium flow rate, which corroborates the hypothesis of inadequate nutrient delivery.
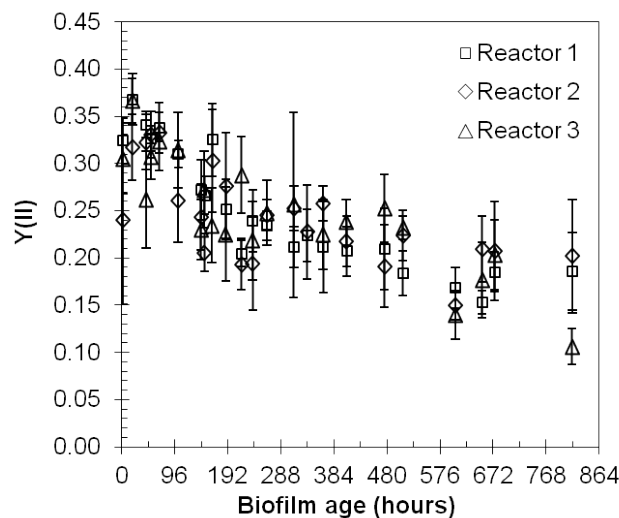
Figure 6.8: Yield of photosystem II (YII) of the biofilms over the duration of the cultivation period.

6.3.3 Free fatty acid harvesting

The amount of free fatty acid was measured in the biofilm itself, the biofilm supporting porous substrate, and the terminal ends. The results indicated that the biofilm itself contained 0.65 μg of FFA. These results were obtained for a biofilm with an age of 145 hours, during which time the average amount of total biomass was 0.46 mg. Therefore, the FFA production rate in the biofilm was approximately 2.7×10^{-9} grams of FFA per gram of biomass per second. It is important to note that approximately linear increase in biomass was observed during this time period. Therefore, the energy intensive process of growth detracted from the process of fatty acid synthesis. One strategy for improving the FFA production rate is to expose the cells to conditions that suppress growth and promote FFA synthesis.

121

Moreover, no appreciable amount of FFA was transported from the biofilm to the terminal end. The mechanism of this tranport process is primarily characterized as diffusion of FFA from the biofilm into the porous medium, followed by advective transport to the terminal end. This transport is opposed by adsorption of the packets onto the cells in the biofilm as well as to the solid material of the porous medium. Therefore, the surface interactions between the cells, the secreted material, and the porous medium material must be understood to design systems that effectively concentrate secreted products in the terminal ends.

6.4   Conclusions

Synthetic leaves were constructed and operated for efficient algal biomass generation. The leaves consisted of an algal biofilm growing on a porous substrate. Evaporation from a terminal end of the porous substrate drove nutrient medium flow through the substrate, thereby delivering water and nutrients to the microorganisms. In this study, a mutant strain of *Synechococcus* sp. that secretes lauric acid was cultivated as the biofilm. The biofilm was exposed to a constant photon flux of 110 μE/m^2-s for a cultivation period of 33 days, during which time the maximum biomass generation rate in the leaves was 0.07 g/m^2-h. Moreover, the nutrient medium transport rate through the leaves as well as the fluorometrically measured yield of photosystem II declined throughout the duration of the experiments at relative rates of 0.1%/h and 0.07%/h, respectively, suggesting that the health of the biofilm was adversely affected by the

decline in nutrient medium flow rate. The decline in the nutrient medium flow rate is attributed to clogging of the porous substrate by the microorganisms themselves. This clogging can be abated by using a porous medium with a smaller maximum pore size than the minimum diameter of the organisms, effectively forming a net that the organisms cannot penetrate. Finally, in future studies, the surface interactions between the secreted products, the microorganisms, and the porous medium material will be studied to enable efficient transport of the secreted products from the biofilm to the terminal ends, where they can be harvested.

Chapter 7

Performance analysis of a scaled up Porous Substrate Bioreactor

This chapter provides design guidelines for a scaled up evaporation driven Porous Substrate Bioreactor (PSBR) by integrating the results of the previous chapters. First, the general shape of a scaled up PSBR is determined. Then, the specific physical values for rib spacing and height are determined taking into account bioreactor productivity and water loss rate. The performance characteristics of the scaled up PSBR are then compared to open pond and closed photobioreactor systems. Finally, opportunities for improvement of the PSBR design are identified.

7.1 Analysis

It was first necessary to design the shape of a scaled up PSBR system. A scaled up system should consist of multiple parallel vertical ribs, as opposed to flat horizontal plates. The multiple vertical rib design allows for significantly larger surface area to volume ratios than a flat plate design, thereby enhancing both gas exchange between the gas phase and the microorganisms and light transfer to the microorganisms. Moreover, the vertical unit design decreases

the irradiance onto a single rib compared to a single horizontal rib, mitigating photoinhibition.

For a vertical rib system, it is possible to feed nutrient medium into a rib either at a single location at the bottom of the rib, or at multiple locations along the height of the rib. The main advantage of feeding at multiple locations is to more evenly distribute fresh nutrient medium. However, the total nutrient medium flow rate into the reactor is limited by the evaporative flux from the exposed region. As an exemplary case, consider a rib with two nutrient medium feed lines, one running along the bottom of the reactor and one running along a line halfway up the interior rib region. In this case, fresh nutrient medium will be delivered to both locations. However, because the total flow rate is controlled by the evaporation rate from the exterior region, the flow rate through each feed port is a fraction of what it would be if there were a single feed port. The half growth length will in turn be equal to a fraction of what it would be if there were a single feed port, and the total growth rate in the rib will be unaffected. Therefore, the multiple nutrient medium inlet concept complicates the design and adds cost without significantly affecting reactor productivity. Consequently, the following analysis focuses on a system in which nutrient medium is fed into the rib along a single contact line at the bottom of the porous rib.

7.1.1 Physical dimensions of the scaled up PSBR

The productivity of evaporation driven PSBRs scales with the evaporative loss rate because evaporation drives nutrient delivery through the system. For most applications, the productivity and water loss rate must be simultaneously taken into account. Consider the multiple vertical rib PSBR shown in Figure 7.1, which is symmetric in the dimension into the page. The aim of this section is to estimate the reactor productivity and evaporative loss rate, per unit footprint area, as a function of the interior height h_i, the exterior height h_e, and the spacing between adjacent ribs d. The distance into the page is assumed to be 1 meter. It was also assumed that the exterior height h_e was less than the minimum critical wetting length under normal operating conditions. It was shown in Chapter 4 that this strategy decreases evaporative loss at night while not sacrificing nutrient delivery during the day. Using this assumption, the exterior region remains completely wet during operation. Finally, the cyanobacterium *Anabaena variabilis* was modeled as an exemplary organism.

7.1.1.1 Areal productivity

The reactor productivity was defined as the biomass production rate per footprint area, reported in grams of biomass per square meter of footprint area per day (g/m²-d). For later PSBR design iterations, productivity can be measured by the amount of secreted product per footprint area. However, calculating the productivity as the biomass production rate enables comparison
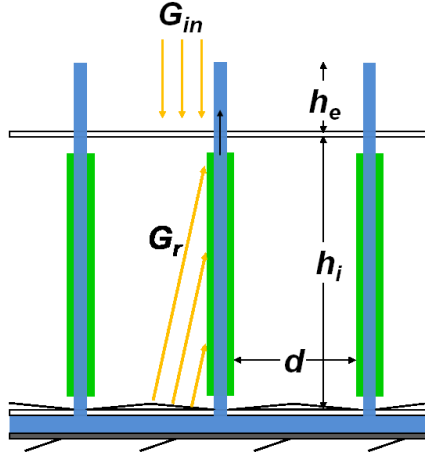
Figure 7.1: Schematic of the scaled up evaporation driven Porous Substrate Bioreactor.

of reactor productivity with conventional reactors.

The PSBR productivity per unit footprint area, $\dot{X}_A$, can be written as,

$$\dot{X}_A = \frac{2h_i}{d}\dot{X}_{A,r} \tag{7.1}$$

d is the spacing between ribs, and h_i is the height of the interior region, and the factor of two results from there being one biofilm on each side of the rib. The productivity per unit biofilm area, $\dot{X}_{A,r}$, can be written as,

$$\dot{X}_{A,r} = \eta_{nd} \int_0^{L_b} \mu(G) X \, dy \tag{7.2}$$

where $\mu(G)$ is the local light limited growth rate, X is the biomass concentration, and L_b is the biofilm thickness. The parameter η_{nd} is the total nutrient delivery effectiveness, which is the ratio of the biofilm growth rate to the growth rate that would exist with no nutrient limitation or inhibition. It was shown in

127

the flux balancing analysis in Chapter 3 that matching the half growth length to the physical length of the system results in a nutrient delivery effectiveness of 0.59.

The local light limited growth rate in the biofilm was calculated using the Monod function,

$$\mu(G) = \mu_{max} \frac{G}{K_{SG} + G + G^2/K_{IG}} - Me \qquad (7.3)$$

where the maintenance term Me has been introduced, which accounts for respiration in the dark. It was assumed in this analysis that Me was equal to 10% of the maximum growth rate in the light [136]. The kinetic parameters μ_{max}, K_{SG}, and K_{IG} for *Anabaena variabilis* were 4.2×10^{-5} s^{-1}, 38 W/m^2 PAR, and 400 W/m^2 PAR, respectively [13, 73].

The local irradiance in the biofilm was calculated by solving the radiative transport equation using the discrete ordinates method, which is described in detail elsewhere [16]. The incident irradiance onto each biofilm, G_r, was calculated using the assumption that the irradiance incident onto the reactor was uniformly diffused onto the biofilm surface area. This uniform diffusion can be accomplished using specular reflecting mirrors along the bottom surface of the reactor. However, as specular reflecters can increase system cost, diffuse reflecters can be used for nearly uniform light diffusion. The irradiance incident onto each rib can then be written as $G_r = G_{in}d/2h$, where G_{in} is the irradiance incident onto the top surface of the reactor. Finally, it has been shown that the optical thickness is the appropriate parameter for scaling photobioreactors.

128

As such, the biofilm optical thickness τ_b was defined as [91],

$$\tau_b = L_b X E \tag{7.4}$$

where L_b is the physical biofilm thickness, X is the microorganism concentration, and E is the mass extinction cross section, reported by Berberoglu and Pilon to be 355 m^2/kg in the photosynthetically active region.

7.1.1.2 Areal evaporative water loss

The total evaporation rate per footprint area is written as,

$$Q_A = \frac{2\dot{Q}_{A,r}h_e}{d} \tag{7.5}$$

where $\dot{Q}_{A,r}$ is the evaporative flux from the exposed region of a single rib, h_e is the length of the exposed region, and d is the spacing between ribs. Furthermore, the flow rate through the interior region of each rib, which can be written as $2\dot{Q}_{A,r}h_e$, was designed to match the half growth length $x_{50\%}$ to the height of the interior region h_i. It was shown in Chapter 3 that the half growth length can be written as,

$$x_{50\%} = h_i = C_{A.v.}\frac{\dot{Q}_{A,r}h_e[i_L]_oY_{X/i_L}}{\mu_o X L_b} \tag{7.6}$$

where Y_{X/i_L} is the biomass yield with respect to the limiting nutrient i_L, and $[i_L]_o$ is the concentration of the limiting nutrient in the fresh nutrient medium, equal to 3570 g/mol and 0.23 mM, respectively. The microorganism specific constant $C_{A.v.}$ was determined to be 0.187 for *A. variabilis*. Substitution of

Equation (7.6) into Equation (7.5) followed by some algebraic manipulation yields the expression for total evaporative loss per footprint area:

$$Q_A = \frac{2h_i \dot{X}_{A,r}/Y_{X/i_L}}{dC_{A.v.}[i_L]_o} \tag{7.7}$$

Equations (7.1) and (7.7) indicate that both the biomass productivity and the evaporative loss rate are dependent on the ratio of the rib spacing d to the interior height h_i. Therefore, the spacing aspect ratio is introduced as $s=d/h$. Finally, the ratio of the interior length to the exterior length is an important parameter as an exterior length that is significantly longer than the interior length can interfere with light delivery to the microorganisms. This ratio can be written as,

$$\frac{h_i}{h_e} = \frac{C_{A.v.}\dot{Q}_{A,r}/[i_L]_o}{\dot{X}_{A,r}/Y_{X/i_L}} \tag{7.8}$$

7.2   Results and Discussion

7.2.1   Areal productivity

During operation of a scaled up PSBR, the biofilms should be maintained within a narrow range of thicknesses in order to maintain the half growth length nearly equal to the interior height. It is therefore of interest to determine the biofilm thickness that maximizes the total system productivity. Figure 7.2 shows the total reactor productivity as a function of the spacing aspect ratio s for systems employing biofilms with thicknesses of 20, 50, 100, and 200 μm, which correspond to optical thicknesses of 0.71, 1.8, 3.6, and 7.1, respectively. The figure indicates that the maximum areal productivities

130

for the systems employing biofilms of optical thicknesses 0.71, 1.8, 3.6, and 7.1, were 8.2, 11.5, 11.9, and 9.8 g/m^2-d, respectively. Moreover, the optimal spacing aspect ratios for reactors employing biofilms of these thicknesses were 0.087, 0.152, 0.242, and 0.423, respectively. Thicker biofilms require sparser rib spacing to enable larger irradiances onto the biofilm surface, thereby increasing the penetration depth of the light into the biofilm. The system with biofilms of optical thickness 7.1 was less productive than the one with optical thickness 3.6 because more cells were in dark regions of the biofilm performing cellular respiration. Because the 3.6 optical thickness biofilm system had the highest productivity of 11.9 g/m^2-d,a system with biofilms of this thickness was modeled in the following evaporative water loss analysis.

7.2.2 Evaporative water loss rate

Figure 7.3a shows the evaporation rate per unit footprint area, as well as the ratio of interior to exterior heights for the 100 μm thick biofilm system. For this analysis, the nutrient medium had the composition of standard BG11 medium and the evaporative flux from the exterior rib region was 130 ml/m^2-hr, equal to the base case flux in the analysis of Chapter 4. The evaporation rate was directly related to the total productivity, which was expected as evaporation drives nutrient flow through the reactor. For a spacing aspect ratio of 0.24, which corresponded to the maximum areal productivity of 12 g/m^2-d, the areal evaporative loss rate was 114 L/m^2-d. By comparison, the water loss rate from open ponds is about 5 L/m^2-d [51, 92]. An evaporative
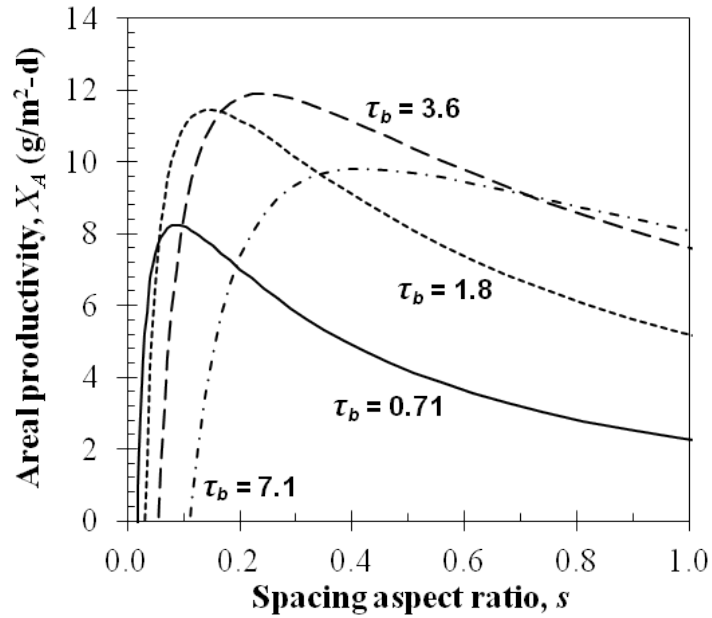
Figure 7.2: Biomass productivity per unit footprint area as a function of spacing aspect ratio and biofilm optical thickness.

loss rate of 114 L/m^2-d is likely infeasible for large scale operation. Moreover, to match the half growth length to the interior height, an exterior length 6.3 times longer than the interior length would be required. Excessive shading of the biofilms by the exterior regions would likely be an issue.

Both the excessive water loss rate and the high ratio of exterior to interior lengths can be mitigated using concentrated nutrient media. Concentrated nutrient medium enables shortening of the exposed region, thereby decreasing the evaporative loss without changing the flow rate of nutrients into the reactor. As a demonstration of this strategy, we modeled a reactor that used 3 times concentrated BG11 with a limiting nutrient (phosphate) concentration

132
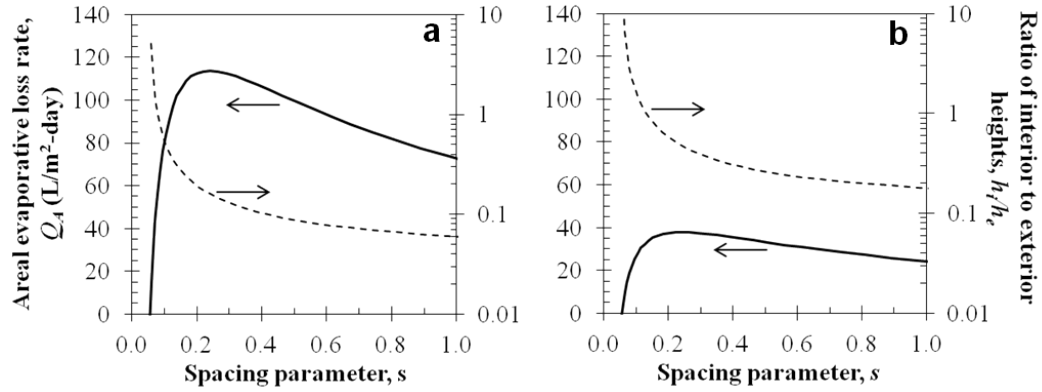
Figure 7.3: Evaporative water loss rate and ratio of interior to exterior rib length for a reactor (a) using standard BG11 nutrient medium and (b) using 3 times concentrated BG11.

of 0.69 mM. Figure 7.3b shows the evaporative loss rate and ratio of interior to exterior heights for the case of concentrated nutrient medium. For the spacing aspect ratio of 0.24, which corresponds to the maximum productivity of 12 g/m^2-d, the evaporative loss rate was 38 L/m^2-d and the ratio of h_i to h_e was 0.5. Thus, using concentrated nutrient media in these systems is advantageous. However, further studies on nutrient inhibition and clogging are necessary to ensure using concentrated nutrient meida does not have adverse effects on both the microorganisms as well as the abiotic system.

7.2.3 Porous medium design constraints

It has been demonstrated that the areal productivity and evaporation rate are dependent on the ratio of d to h_i to h_e and not on the absolute values of any of the three parameters. However, the performance of the vascular

fluid delivery structure is dependent on physical dimensions. It was shown in Chapter 4 that due to the balance between capillary, viscous and gravitational forces, there exists a critical wetting length of the exterior region. This wetting length is a function of the evaporative flux from the membrane as well as the mechanical properties of the porous substrate itself. Assuming an evaporative flux from the membrane surface of 130 ml/m^2-hr, a h_i to h_e ratio of 1 to 2, and a porous material bulk contact angle of 20°, it was determined that the maximum total system height, h_i+h_e, was about 85 cm, which was achieved using a porous substrate pore radius of 8 μm. Therefore, scaled up PSBRs should be designed to have a total height less than 85 cm. For 3 times concentrated BG11 nutrient medium, the ratio d to h_i to h_e should be approximately 1 to 4 to 8. Such a system would have a biomass productivity and evaporative water loss rate of about 12 g/m^2-d and 38 L/m^2-d, respectively. It is important to note that the aspect ratio of the reactor can be varied to reduce the evaporative loss rate, but these water savings come at the expense of biomass productivity.

7.3   Comparison to conventional cultivation systems

Table 7.1 compares the performance of evaporation driven PSBRs (EDPS-BRs) to conventional algae cultivation technologies, namely open ponds and closed photobioreactors. The biomass productivity is about equal to that of open ponds and about half of the productivity of closed photobioreactors. The mixing energy requirement is eliminated in EDPSBRs because nutrient delivery is accomplished by the evaporation driven flow through the reactor.

However, the savings in mixing energy are paid for by the evaporative water loss, which is about 8 times higher than for open ponds. Finally, the culture densities in EDPSBRs are about 100 times greater than those for conventional reactors, thus decreasing the energy intensiveness of concentrating and dewatering the resultant biomass.

Table 7.1: Performance comparison between conventional algae cultivation systems and evaporation driven PSBRs (EDPSBRs).

	Open ponds [51, 58]	Closed photobioreactors [58]	EDPSBR
Productivity (g/m^2-d)	11	25	12
Water loss rate (L/m^2-d)	5	0	40
Mixing Energy (kJ/m^2-d)	100	1700	0
Biomass conc. (kg/m^3)	0.5	5	100

Because of the high water consumption rate and negligible mixing power requirement characteristic of EDPSBRs, they are suited well for applications in which water is plentiful but electricity is scarce. One example of such an application is in littoral off-grid habitations in which enriched seawater can be used as a nutrient medium. Moreover, the low working water volume as well as the independence of inertial forces make EDPSBRs an ideal candidate for microorganism cultivation in space for biological gas recycling and food production.

Chapter 8

Summary and Recommendations

8.1 Summary

This dissertation focused on the design, construction, operation, modeling, and optimization of a synthetic leaf for sustainable biofuel production. Also known as an evaporation driven Porous Substrate Bioreactor, the system uses an artificial transpiration mechanism to passively deliver water and nutrients to attached algal cultures growing on a porous substrate. This cultivation strategy significantly reduces the amount of energy required for nutrient delivery as well as downstream biomass harvesting. The summary below provides the major conclusions and contributions of each chapter of the dissertation.

- In Chapter 2, a scaled down multiple rib synthetic leaf prototype was constructed and operated alongside a conventional planktonic photobioreactor. The working water volume of the synthetic leaf prototype was about 25 times less than that of the planktonic photobioreactor. Moreover, the artificial transpiration mechanism used to deliver nutrients in the synthetic leaf prototype required no power, whereas culture mixing in the planktonic prototype required about 320 W/m^3. Certain locations within the synthetic leaf prototype exhibited growth rates four

times greater than the growth rate in the planktonic photobioreactor. However, growth was spatially non-uniform in the synthetic leaf system, which was attributed to difference in light and nutrient availability in the reactor.

- Chapter 3 focused on an integrated light transfer, mass transfer, and growth kinetic model for understanding energy transport and conversion in the synthetic leaf environment. The numerical model was used as a tool for testing strategies to balance the nutrient flux to photosynthetic microorganisms with the photon flux, which ensures efficient photon utilization. The half growth length was defined as the distance from the nutrient medium reservoir in the direction of flow at which the growth rate declined to half its maximum value in the biofilm as a result of nutrient depletion. In the case of cultivating cyanobacteria with the nutrient medium BG11, inadequate phosphate delivery was identified as the primary reason for the decline in growth rate. A scaling analysis was performed to predict the half growth length as a function of microbial growth kinetics, nutrient medium composition, and nutrient medium flow rate through the reactor. This chapter is useful for Porous Substrate Bioreactor designers as it enables matching of the physical length of the porous rib to the half growth length for optimal productivity and nutrient utilization.

- Chapter 4 provided a coupled heat, mass, and momentum transport analysis for modeling the nutrient medium flow through the synthetic leaf

as a function of environmental parameters surrounding the evaporator region and mechanical properties of the porous substrate. The vertical system was divided into an interior region, from which evaporation was negligible, and an exterior region with a decreasing mass flow rate in the direction of flow as a result of evaporation. The critical wetting length was defined as the wetted length of the exterior region for which the capillary pressure balanced the sum of the viscous and gravitational pressure drops. The critical wetting length, and thus the maximum allowable flow through the rib, was maximized for a porous substrate pore radius of about 10 μm. For this pore radius, under a range of typical operating conditions, the maximum critical wetting length and total flow rate through the reactor ranged from 0.5 to 0.9 m and from 0.14 to 0.05 L/m-h, respectively. These flow rates enable calculation of the half growth distance, which in turn provides design guidelines for sizing Porous Substrate Bioreactors such that the half growth length matches the physical length of the growth region.

- Chapter 5 presented a novel wide band spectral imaging method for remotely measuring the local biomass concentrations of the synthetic leaf biofilms in real time. In this method, a calibration data set was prepared in which red-green-blue images were acquired of biofilms of known biomass densities. The green intensity of the images declined more gradually than the red and blue as a result of selective absorption by the photosynthetic pigments. Thus, a correlation was then generated between

the green value of the image and the areal biomass density of the biofilm. The generated correlation predicted the biomass density of an independently prepared set of biofilms to within 7% under equal lighting and background conditions. This method provides a remote, non-invasive technique for monitoring the productivity of biofilm photobioreactors in real time.

- Chapter 6 presented the results of an experimental characterization of single rib synthetic leaf photobioreactors. In this study, surface-modified polyvinylidene fluoride (PVDF) was used as the porous rib and *Synechococcus* sp. $\Delta fadD^{C12}$, a cyanobacterium that was engineered to secrete lauric acid, was used for the biofilm. Under an irradiance of 24 W/m^2 PAR, the biofilms demonstrated a maximum biomass production rate of 0.07 g/m^2-hr, which corresponds to an overall photosynthetic efficiency of about 1.4%. By extrapolating these results to multiple rib scaled up systems, an areal biomass production rate of about 6 grams per square meter of footprint area per day was predicted. Faster nutrient delivery was identified as an opportunity for increased productivity.

- Chapter 7 provided design guidelines on the size and shape of scaled up Porous Substrate Bioreactors from the perspective of overall biomass productivity and evaporative loss rate. The evaporative loss rate scaled with the biomass productivity because evaporative flow provides nutrients for growth. Using the vascular system modeling results of Chapter 4, it was determined that the height of Porous Substrate Bioreactors

should not exceed about 80 cm. At heights below this critical height, the evaporative loss and biomass productivity are dependent on the relative values of the rib spacing, the length of the interior growth region, and the length of the exterior evaporator region. A system designed for maximum productivity should have a ratio of these lengths of about 1:4:8, and would have a biomass productivity and evaporative loss rate of about 12 g/m^2-d and 38 L/m^2-d, respectively. Due to the high evaporative loss rate compared to conventional reactors, as well as the elimination of required input energy for pumping and mixing, evaporation driven Porous Substrate Bioreactors are best suited for applications in which water is plentiful but electricity is scarce.

Overall, this dissertation contributed a novel photobioreactor type for terrestrial biofuel and high value product generation, life support of humans in space, and carbon sequestration. Moreover, design guidelines were provided for these reactors from both biological and engineering perspectives.

8.2 Recommendations for future research

8.2.1 Secreted product harvesting

Ultimately, we envision the synthetic leaf as a system for passively harvesting bioproducts secreted by the microorganisms in addition to passively delivering nutrients. Theoretically, this will occur as secreted products diffuse down their concentration gradient from the biofilm into the porous medium. Once in the porous medium, the products are carried with the advective flow

toward the terminal end, where they become concentrated. It will then be necessary to extract the products from the terminal end to prevent clogging in the terminal end and also to utilize the secreted products for their intended purpose.

For the length scales characteristic in the interstitial spaces of the biofilm and porous medium (less than 1 μm), surface interactions will play a major role in the transport of the secreted products. Moreover, biofuel feedstock secretions will most likely be non-polar, as was the case for the lauric acid secreted by the mutant *Synechococcus* strain. Therefore, a thorough understanding of the surface interactions between the secreted products, the microorganisms, the extracellular polymeric substances, the aqueous nutrient medium, and the porous medium material will be necessary for modeling the transport of the secreted products. Additionally, biocompatible surfactants and/or solvents can be used to alter the surface tension of the aqueous phase and the solubility of the secreted products, respectively. A thorough study from the perspective of surface interaction and water chemistry is necessary to design strategies for harvesting secreted products from the synthetic leaf biofilm. Another important study lies in designing a strategy to extract the products once they have concentrated in the terminal end.

8.2.2 Advanced biofilm productivity modeling

Chapter 3 presented the results of an integrated light transfer, mass transfer, and growth kinetic model for photosynthetic biofilms. While the

model showed satisfactory agreement with experimental results, it also had several limitations constraining its use as a robust modeling tool.

The first major limitation of the model was that it could only handle biofilms with simple geometries. Specifically, the thickness was uniform in the direction of nutrient medium flow. However, it was also observed that the growth rate decreased in the direction of nutrient medium flow due to consumption by the microorganisms. Therefore, in reality, the spatial heterogeneity in growth rate precludes the possibility of experimentally cultivating a constant thickness biofilm, as the thickness will decrease with increasing downstream distance. Moreover, the model was unable to automatically update the biofilm thickness using the local growth rate. With these limitations in mind, future modeling efforts should focus on transient models that allow for spatially heterogeneous increases in biofilm thickness. In this way, the user can input an initial uniform biofilm thickness and the model would automatically increase the local thickness using the local growth rate. This capability would significantly increase the utility of the model for predicting synthetic leaf biomass production rates.

Moreover, in the modeling effort presented in this document, the microorganism concentration, elemental composition, and pigmentation were assumed to be uniform. However, it has been shown that in real biofilms, microorganism concentration can vary significantly, generally increasing in density with increasing distance from the free surface [66]. However, most of the biofilms that have been observed to have this spatial non-uniformity are ex-

posed to different mechanical loading conditions than synthetic leaf biofilms. The traditional biofilm model consists of a solid surface on one side of the film and a nutrient-containing liquid layer on the other, whereas synthetic leaf biofilms have a nutrient-containing porous surface on one side and a gas phase on the other. The effect of this inherent difference in loading conditions on the spatial heterogeneity in microorganism concentration must be understood for accurate modeling as it affects all three of the light transport, the mass diffusivity of nutrients, and the nutrient consumption rate.

The elemental composition of the organisms was also assumed to be constant, but in reality, elemental composition can vary considerably based on the concentrations of the available nutrients [31, 105]. While assuming constant elemental composition was useful in identifying the limiting nutrient for a given nutrient medium as well as predicting the location of its exhaustion, it will be important in future studies to understand biological responses to spatially dependent nutrient limitations. Changes in elemental composition of the cells can provide better accuracy in nutrient consumption rates and therefore locations of nutrient exhaustion. Furthermore, effects of nutrient limitation on biofilm metabolism can potentially be exploited to induce changes in production rates of valuable products.

The total pigment content per cell as well as the distribution of different pigments within the organisms was also assumed to be constant. However, it is well known that photosynthetic organisms can regulate their pigmentation based on the intensity and spectral content of the light available [42]. It is

therefore plausible that the pigmentation of the organisms would increase with increasing distance from the illuminated surface due to the decrease in available irradiance and the change in spectral quality. This non-uniform pigmentation would affect both the light distribution in the biofilm and the photosynthetic rate per cell as a function of irradiance [16, 90]. Moreover, the photosynthetic rate was assumed to be dependent on the local irradiance, but not the spectral quality of the irradiance. In future studies, the radiative transport equation solver, the spectral scoring method (Appendix A), and the photosynthetic response of spatially heterogeneously pigmented cells can be used to more fully understand and optimize the irradiance onto the biofilm.

Appendices

Appendix A

A method for evaluation of light sources in illuminating algal cultures

A.1   Introduction

In some applications, it is necessary to illuminate the synthetic leaf system with artificial lighting. As such, this appendix focuses on the dependence of algal productivity on the spectral content of the light used to illuminate the organisms. Traditionally, experimental studies have reported the local photon flux as the photosynthetically active radiation (PAR), which is the total photon flux at wavelengths between 400 and 700 nm [3]. However, the photosynthetic action spectrum, defined as the photosynthetic rate as a function of wavelength, is highly variable within the PAR range due to selective absorption of photosynthetic pigments. Therefore, wide variation can be observed between the photosynthetic productivities of two identical cultures under equal PAR irradiance with different spectral contents. This study aims to quantify the effect of the spectral content of the light source on the photosynthetic productivity of the algal culture using a novel spectral scoring method.

A.2 Materials and Methods

A.2.1 Microorganisms and nutrient media

The photosynthetic rates of the green alga *Chlorella vulgaris*, as well as the cyanobacteria *Anabaena variabilis* and *Spirulina platensis* were investigated in this study. Batch cultures were cultivated on a shake table under an irradiance of 45 ± 10 μE/m^2-s using cool white fluorescent bulbs. The green algae and cyanobacteria were cultivated using the ATCC 487 medium and BG11 medium, respectively [3].

A.2.2 Experimental setup

During the batch culture exponential growth phase, culture samples were placed into a custom air-tight and water-tight acrylic testing chamber measuring 3 cm on a side and 2 cm tall. Figure A.1 shows the experimental setup. An optical dissolved oxygen sensor with a needle tip (Firesting, OXR50) was placed at the center of the testing chamber by piercing through a rubber septum on the side of the chamber. Moreover, a magnetic stir bar was used to ensure adequate mixing.

The testing chamber was illuminated using a tunable light-emitting diode (LED) bank containing LEDs with 16 different wavelengths between 400 and 700 nm (Telelumen, Light Replicator). The photon flux density incident onto the chamber was measured using a PAR quantum sensor (Li-Cor, 190A), and was equal to 24.3 ± 0.8 μE/m^2-s for all experiments. The photosynthetic rate was measured as the rate of increase in the dissolved oxygen concentration
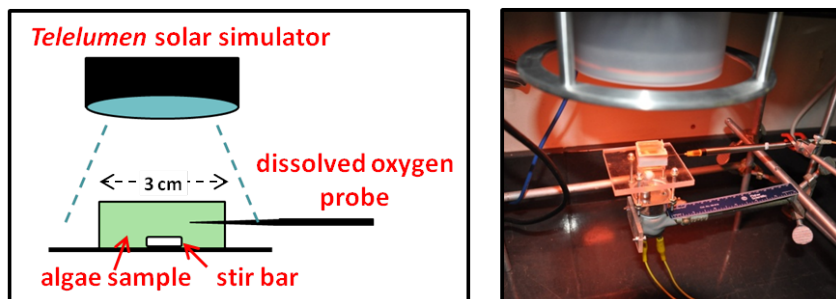
Figure A.1: Experimental setup used to measure the photosynthetic rate of the algal cultures.

in the chamber. This rate of increase was determined by fitting a least squares regression line to the dissolved oxygen concentration versus time data recorded by the oxygen sensor.

A.2.3 Spectral content of the light sources

The spectral content of the light source was controlled by controlling the voltage to each wavelength LED individually using the Telelumen software. Figure A.2 shows the spectral content of the simulated solar spectrum, spectrum I, and spectrum II used to illuminate the algae. The action spectra of representative green algae and cyanobacteria reported by McLeod are also shown [78]. Spectrum I was designed to overlap with the action spectra of the algae and spectrum II was designed not to overlap.

A.2.4 Spectral score

To quantify the effectiveness with which the light source excited the reaction centers of the photosynthetic machinery, the spectral score S was
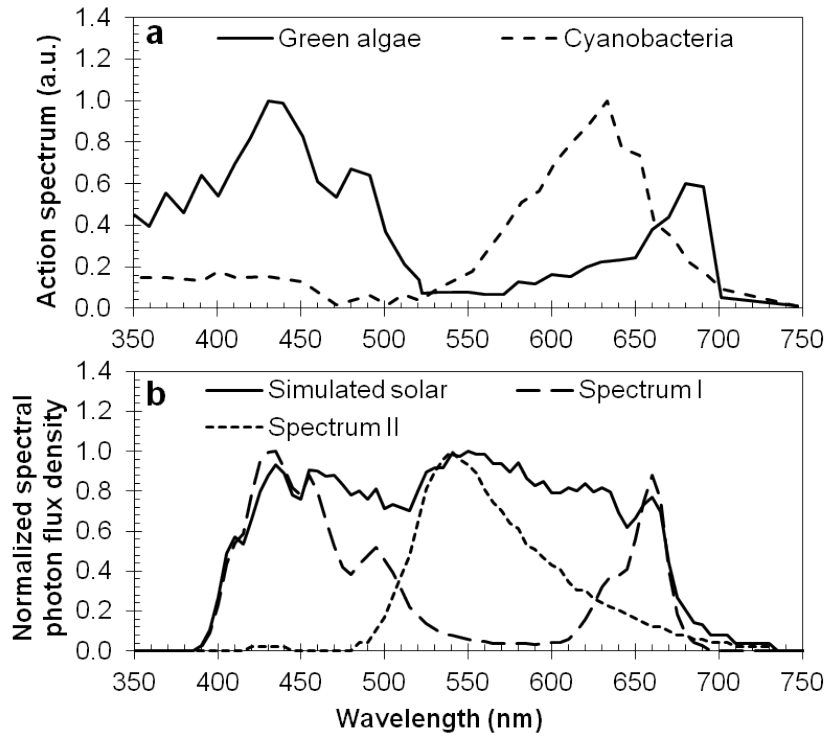
Figure A.2: Three spectra used to illuminate the algal cultures.

defined as,

$$S = \frac{\int_{\lambda=0}^{\infty} G_\lambda \overline{A_\lambda} d\lambda}{\int_{\lambda=0}^{\infty} G_\lambda d\lambda} \qquad (A.1)$$

where G_λ is the spectral irradiance and $\overline{A_\lambda}$ is the spectral photosynthetic rate at wavelength λ, normalized by the maximum spectral photosynthetic rate. Therefore, the spectral score is essentially the degree of overlap between the light source spectrum and the action spectrum.

A.3 Results and Discussion

Figure A.3 shows the photosynthetic rate for each strain, normalized by the maximum photosynthetic rate for that strain, as a function of the spectral score. A strong direct relationship was observed between the photosynthetic rate and the spectral score. Therefore, the spectral score can be used as a metric for evaluating the effectiveness with which a light source illuminates an algal culture. Moreover, outdoor solar lighting can be simulated using indoor artificial lighting by matching the product of the spectral score and the irradiance between the two scenarios.
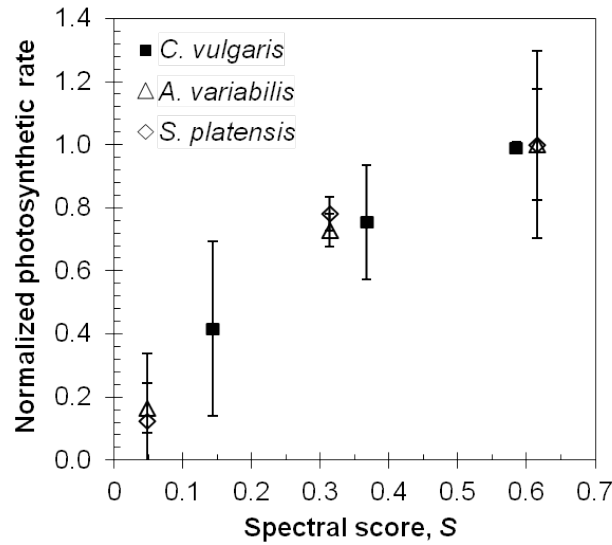
Figure A.3: Photosynthetic rate as a function of spectral score of the light source.

In this study, the action spectra of the green algae and cyanobacteria were assumed to be equal to those of representative species as these action spectra were reported in the literature [78]. To improve the spectral scoring

method, the action spectrum for a given strain can be measured experimentally using fluorescent or oxygen evolution techniques. Future studies can also investigate the dependence of spectral score on culture depth within an algal culture, as it will decrease in the direction of light travel due to selective absorption by the microorganisms.

A.4 Conclusions

In this study, a spectral scoring method was designed to evaluate the effectiveness with which a light source illuminates the photosynthetic reaction centers of microalgae. The spectral score was defined as the degree of overlap between the action spectrum of a strain and the spectral content of the light source. The photosynthetic rates of *Chlorella vulgaris*, *Anabaena variabilis*, and *Spirulina platensis* were measured for spectra with different spectral scores. A strong linear relationship was observed between the photosynthetic rate and the spectral score. The spectral score can be used to simulate outdoor lighting conditions using artificial lighting.

Appendix B

Procedure for Bligh-Dyer total lipid extraction

This appendix describes the procedure for performing a Bligh-Dyer extraction, which extracts lipids from an aqueous phase into a chloroform phase. The lipid content of the chloroform phase can then be analyzed using thin layer chromatography or another method.

1. Place 0.8 volume of aqueous phase in a glass container. The aqueous phase can be an algae culture or supernatant.

2. Add 2 volumes of methanol and vortex well.

3. Add 1 volume of chloroform and mix by inversion.

4. Add 1 volume of chloroform, do not mix.

5. Add 1 volume of deionized water. Separation of the chloroform phase (bottom) should be clearly visible. If it is not, continue adding water.

6. Wait until the phases are clearly separated, which is marked by clear, rather than cloudy appearance in the bottom chloroform phase.

7. Discard the aqueous (top) phase.

8. Dry down the chloroform phase until the chloroform evaporates completely. Resuspend the sample in a desirable volume of chloroform (usually about 10 to 20 μl). This chloroform phase is ready for analysis.

Appendix C

Procedure for Thin Layer Chromatography (TLC) for lipid analysis

This appendix describes the procedure for performing a thin layer chromatography (TLC) experiment, which is used to determine the concentrations of different types of lipids in a liquid sample.

1. Cut a TLC plate to the desired height and width. The height should be at least 8 cm for good separation, and the separation increases with increasing height. The width is dependent on the number of samples to be analyzed. Approximately, about 1.5 cm are required per sample.

2. Place a small amount of 80:20:1 hexane:diethyl ether:acetic acid solution into a beaker with an inner diameter at least as wide as the TLC plate width. Fill to a height of about 0.5 cm. Cover the beaker tightly with aluminum foil.

3. With a pencil, mark the locations where the samples will be pipetted. Two lanes should be reserved for the calibration standard. The marks should be evenly spaced along a line about 1 cm above the bottom edge of the plate. It is important that the samples will not be submerged in liquid once the plate is placed in the beaker.

153

4. Pipette the calibration standard, as well as the samples onto their respective marks. Allow them to dry completely.

5. Carefully place the bottom edge (the edge closest to the samples) into the beaker.

6. Allow the liquid to infiltrate the plate till about 1 cm below the top edge.

7. Remove the plate and allow it to dry completely.

8. In the fume hood, spray a uniform light green coat onto the plate using the spray bottle of phosphomolybdic acid (PMA).

9. Place the plate in the oven until gray streaks appear, about 5 minutes. The intensity of the gray streak is directly related to the lipid content of the sample. Figure C.1 shows the locations of different types of lipids.
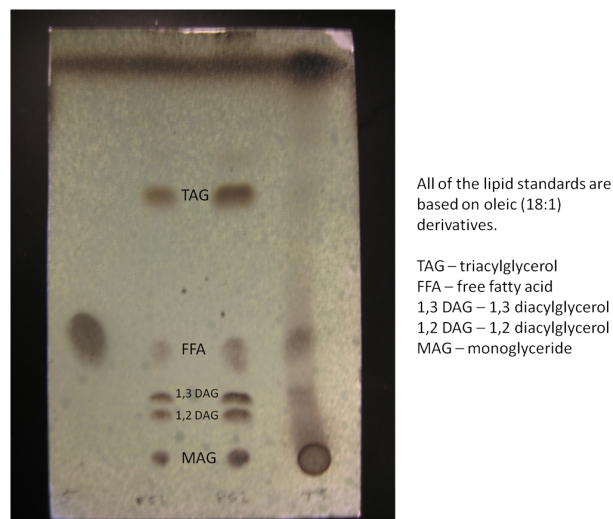
Figure C.1: Locations of the different types of lipids using the 80:20:1 hexane:diethyl ether:acetic acid carrier phase.

154

Appendix D

Scaling analysis for the mass transport model presented in Chapter 3

This appendix compares the magnitudes of diffusion and advection terms in the in-plane and out-of-plane directions for the mass transfer model presented in Chapter 3. Figure D.1 shows the schematic of the porous substrate bioreactor, as well as the control volumes used to investigate transport in each biofilm and the porous medium. First, the magnitudes of diffusive to advective transport were compared in each the biofilm and the porous medium. To do this, the Peclet number was written as [82],

$$Pe = \frac{Lv}{D} \tag{D.1}$$

where L is the thickness, v is the out-of-plane velocity, and D is the diffusion coefficient. The out-of-plane velocity through the biofilm is equal to that through the porous medium due to continuity. Moreover, this velocity is dependent on the evaporation rate from the biofilm surface and can be written as,

$$v = \frac{1}{\rho}k_\omega(\omega_s - \omega_\infty) \tag{D.2}$$

where ρ is the mass density of the liquid medium, k_ω is the mass transfer coefficient between the biofilm surface and the gas phase, and $\omega_s - \omega_\infty$ is the

difference in water vapor mass fraction between the biofilm surface and the gas phase. Using the approach presented in Chapter 4, it was determined that a reasonable value for the mass transfer coefficient k_ω was about 1 g/m^2-s. Moreover, for gas phase relative humidities greater than 90%, which is a conservative lower limit, the Peclet numbers in the biofilm and the porous medium are less than 0.001 and 0.007, respectively. Therefore, diffusion dominates over advection in the out-of-plane direction in both the biofilm and the porous medium, and advective terms in the out-of-plane direction can be neglected.
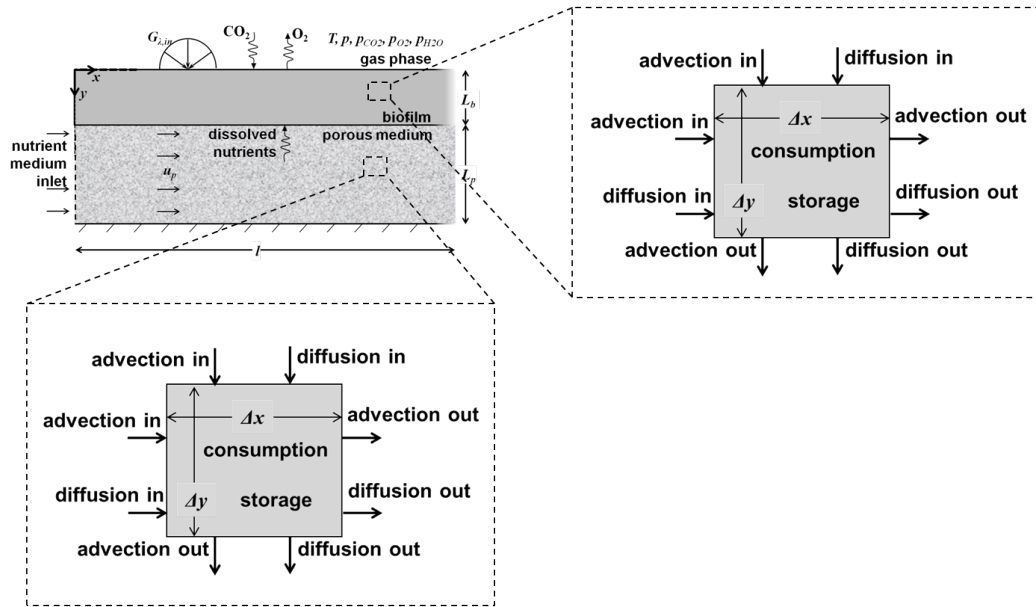
Figure D.1: Schematic and control volumes for mass transfer analysis of the PSBR.

It was assumed that no microorganisms occupied the interstices of the porous medium, and therefore consumption and production were neglected

in this region. Finally, advection in the in-plane direction in the biofilm was neglected. The presence of extracellular polymeric substances as well as the dense packing of the biofilm made it significantly less hydraulically permeable than the porous medium, causing a negligible fraction of the in-plane flow to flow through the biofilm itself.

Appendix E

Matlab script for the biofilm modeling study (Chapter 3)

This code is used for modeling transport and consumption of nutrients within a Porous Substrate Bioreactor. It is a finite element model that discretizes the biofilm and porous substrate into finite volume elements, and then marches through time to track the local growth rates, pH, as well as concentrations of nitrate, phosphate, total inorganic carbon, and molecular oxygen as a function of space and time.

E.1   Main code

```
1  clear
2
3  %indices for the parameter sweep
4  for u_index=1:1
5  for Lp_index=1:1
6  for P_index=1:1
7  for G_index=1:1
8  for Lb_index=2:2
```

```matlab
9    for f_v_index=1:1

10

11   %set

12   if G_index==1

13   G_total=20;  %W/m2

14   else

15   G_total=40;

16   end

17

18   %load light profile from RTE solver

19   if Lb_index==1

20   load('irradiance_solar_50um.mat');

21   irradiance=irradiance_solar_50um;

22   elseif Lb_index==2

23   load('irradiance_solar_100um.mat');

24   irradiance=irradiance_solar_100um;

25   end

26

27   %load pH matrix for later interpolation

28   load('pH_matrix.mat');

29

30   %constants

31   rho_w=1000;
```

```matlab
32   rho_b=1020; %kg/m3

33   K_H_CO2=10^-1.46; %M/atm, Henry's constant for CO2

34   Ka1=10^-6.3;

35   Ka2=10^-10.3;

36   K_H_O2=1.3e-3; %M/atm

37

38   %biofilm thickness

39   if Lb_index==1

40   biofilm_thickness=50e-6; %100 um thick biofilm

41   elseif Lb_index==2

42   biofilm_thickness=100e-6;

43   end

44

45   biomass_density=100; %kg/m3

46

47   %gas phase concentrations

48   p_co2_g=1*0.00038; %atm, atmospheric CO2 concentration

49   p_o2_g=1*0.21; %atm, atmospheric O2 concentration

50

51   %void fraction of porous medium

52   if f_v_index==1

53   f_v=0.85;

54   else
```

```matlab
55   f_v=0.35;
56   end
57
58   %nutrient medium velocity
59   if u_index==1
60   u_p=4.6e-6; %m/s
61   else
62   u_p=100e-6;
63   end
64
65   %porous medium thickness
66   if Lp_index==1
67   L_pm=0.4e-3;
68   else
69   L_pm=0.2e-3;
70   end
71
72   %length in the in-plane direction
73   system_length=6e-2;
74
75   %molar masses (g/mol)
76   M_HCO3=1+12+3*16;
77   M_CO2=12+2*16;
```

```matlab
78   M_NO3=14+3*16;

79   M_HPO4=1+31+4*16;

80   M_H2PO4=2*1+31+4*16;

81   M_O2=32;

82

83   %determine dominant species based on pH

84   [D_CO2_b,D_HCO3_b,D_NO3_b,D_HPO4_b,D_H2PO4_b,...

85       D_O2_b,D_CO2_pm,D_HCO3_pm,D_NO3_pm,D_HPO4_pm,...

86       D_H2PO4_pm,D_O2_pm]=diffusive_permeabilities...

87       (biomass_density,f_v);

88

89   %discretize space

90

91   %biofilm in the out-of-plane direction

92   if Lb_index==1

93   N_nodes=5;

94   else

95   N_nodes=10;

96   end

97

98   %calculate locations of node centers

99   d_node=biofilm_thickness/N_nodes;

100  z(1)=biofilm_thickness/N_nodes/2;
```

```matlab
101  for i=2:N_nodes
102  z(i,1)=z(i-1,1)+d_node;
103  end
104
105  %discretize porous medium
106  N_nodes_pm=10;
107  d_node_pm=L_pm/N_nodes_pm;
108  z_pm(1)=L_pm/N_nodes_pm/2;
109  for i=2:N_nodes_pm
110  z_pm(i,1)=z_pm(i-1,1)+d_node_pm;
111  end
112
113  %discretize system in x-direction
114  N_nodes_x=10;
115  d_node_x=system_length/N_nodes_x;
116  x(1)=system_length/N_nodes_x/2;
117  for i=2:N_nodes_x
118  x(i)=x(i-1)+d_node_x;
119  end
120
121  %set initial pH using the composition of the nutrient medium
122  total_P_cons=0;
123  pH(1,1:length(x))=interp2(pH_matrix(1,2:4),pH_matrix...
```

```matlab
124        (2:9,1),pH_matrix(2:9,2:4),total_P_cons,p_co2_g);

125

126    %set initial nutrient concentrations

127

128    %carbon

129    C_C=ones(length(z),length(x))*p_co2_g*K_H_CO2*...

130        (1+Ka1*10^pH(1)+Ka1*Ka2*10^(2*pH(1)));  %M

131    %C_C_o=C_C(1,1); %boundary condition

132    C_C_pm=ones(length(z_pm),length(x));

133    C_C_pm(:,:)=C_C(1,1);

134

135    %oxygen

136    C_O2=ones(length(z),length(x))*p_o2_g*K_H_O2;  %M

137    C_O2_o=C_O2(1,1);

138    C_O2_pm=ones(length(z_pm),length(x));

139    C_O2_pm(:,:)=C_O2_o;

140

141    %nitrate

142    C_N_o=17.65e-3;

143    C_N=ones(length(z),length(x))*C_N_o;

144    C_N_pm=ones(length(z_pm),length(x));

145    C_N_pm(:,:)=C_N_o;

146
```

```matlab
147   %phosphate
148   if P_index==1
149   C_P_o=0.23e-3; %P concentration in mol/L in BG11
150   else
151   C_P_o=0.46e-3;
152   end
153   C_P=ones(length(z),length(x))*C_P_o;
154   C_P_pm=ones(length(z_pm),length(x));
155   C_P_pm(:,:)=C_P_o;
156
157   %interpolate irradiance table to find local irradiance
158   G_use=G_total*interp1(irradiance(:,1),irradiance(:,2),z);
159
160   %load Monod growth kinetic parameters
161   mu_max=4.2e-5; %s^-1
162   K_SG=38; %W/m2
163   K_IG=400; %W/m2
164   K_SC=2e-4; %M
165   K_IC=0.0182;
166   K_SN=5e-4; %M
167   K_SP=1.7e-5; %M
168   K_O2=2.66e-3; %M
169
```

```
170   %load biomass yields (kg biomass/kmol)

171   Y_C=22.4;

172   Y_N=178.4;

173   Y_P=3568;

174

175   %set simulation time

176   %discretize time

177   max_time=15000; %s

178   time_step=0.01; %s, pay attention to Fourier number

179   %(must be <0.25 for stability)

180   Fo=D_HPO4_b*time_step/d_node^2;

181

182   %for looking at transient behavior

183   record_every=max_time/10; %10 timestamped profiles

184   record_interval=round(record_every/time_step);

185   max_time_steps=max_time/time_step;

186   save_matrix=1;

187   record_counter=record_interval-1;

188

189   %pre-allocate matrices to save time

190   [mu,biomass_gen_rate,cons_C,cons_O,cons_N,cons_P,...

191       del_omega_C,del_omega_O,del_omega_N,del_omega_P,...

192       del_omega_C_pm,del_omega_O_pm,del_omega_N_pm,...
```

```matlab
193        del_omega_P_pm,del_omega_C_x,del_omega_O_x,...
194        del_omega_N_x,del_omega_P_x,del_omega_C_pm_x,...
195        del_omega_O_pm_x,del_omega_N_pm_x,del_omega_P_pm_x,...
196        adv_C_pm,adv_O2_pm,adv_N_pm,adv_P_pm]...
197        =preallocate(length(z),length(x),length(z_pm));
198
199 %time loop
200 for tstep=2:max_time_steps
201
202 time=(tstep-1)*time_step;
203 record_counter=record_counter+1;
204
205 %inplane loop
206 for xstep=1:length(x)
207
208 %calculate pH and total carbon at x-location
209 total_P_cons=1-mean(C_P(:,xstep))/C_P_o;
210 pH(1,xstep)=interp2(pH_matrix(1,2:4),pH_matrix(2:9,1),...
211     pH_matrix(2:9,2:4),total_P_cons,p_co2_g);
212 C_C_o=p_co2_g*K_H_CO2*(1+Ka1*10^pH(1,xstep)+Ka1*Ka2...
213     *10^(2*pH(1,xstep)));
214
215 %determine dominant species based on pH
```

```matlab
216 [D_C_b,D_C_pm,M_C,D_P_b,D_P_pm,M_P]...
217     =dominant_species(pH(xstep),D_CO2_b,D_CO2_pm,...
218     M_CO2,D_HCO3_b,D_HCO3_pm,M_HCO3,D_H2PO4_b,...
219     D_H2PO4_pm,M_H2PO4,D_HPO4_b,D_HPO4_pm,M_HPO4);
220
221 %out-of-plane loop
222 for zstep=1:length(z)
223
224 %growth rate and consumption terms
225 mu(zstep,xstep)=mu_max*(G_use(zstep)/(K_SG+G_use(zstep)...
226     +G_use(zstep)^2/K_IG))*(C_C(zstep,xstep)/(K_SC+...
227     C_C(zstep,xstep)+C_C(zstep,xstep)^2/K_IC))...
228     *(C_N(zstep,xstep)/(C_N(zstep,xstep)+K_SN))...
229     *(C_P(zstep,xstep)/(C_P(zstep,xstep)+K_SP))...
230     *(1/(1+C_O2(zstep,xstep)/K_O2));
231 biomass_gen_rate(zstep,xstep)=mu(zstep,xstep)...
232     *biomass_density*d_node_x*d_node;
233 cons_C(zstep,xstep)=biomass_gen_rate(zstep,xstep)/Y_C*1000;
234 cons_O(zstep,xstep)=-cons_C(zstep,xstep);
235 cons_N(zstep,xstep)=biomass_gen_rate(zstep,xstep)/Y_N*1000;
236 cons_P(zstep,xstep)=biomass_gen_rate(zstep,xstep)/Y_P*1000;
237
238 %calculate gradients for diffusion terms
```

```matlab
239
240    if zstep==1
241
242    %constant surface condition for CO2 and O2
243    del_omega_C(1,xstep)=(-C_C_o-(C_C(1,xstep)+C_C(2,xstep))/2...
244    +2*C_C(1,xstep))/(d_node/2)*(M_C/rho_b);
245    del_omega_O(1,xstep)=(-C_O2_o-(C_O2(1,xstep)+C_O2(2,xstep))/2...
246    +2*C_O2(1,xstep))/(d_node/2)*(M_O2/rho_b);
247
248    %zero flux boundary condition for nitrates and phosphates
249    del_omega_N(1,xstep)=(0-(C_N(2,xstep)-C_N(1,xstep)))/d_node...
250        *(M_NO3/rho_b);
251    del_omega_P(1,xstep)=(0-(C_P(2,xstep)-C_P(1,xstep)))/d_node...
252        *(M_P/rho_b);
253
254    elseif zstep<length(z)
255    del_omega_C(zstep,xstep)=(-C_C(zstep-1,xstep)-C_C(zstep+1,...
256        xstep)+2*C_C(zstep,xstep))/d_node*(M_C/rho_b);
257    del_omega_O(zstep,xstep)=(-C_O2(zstep-1,xstep)-C_O2(zstep+1,...
258        xstep)+2*C_O2(zstep,xstep))/d_node*(M_O2/rho_b);
259    del_omega_N(zstep,xstep)=(-C_N(zstep-1,xstep)-C_N(zstep+1,...
260        xstep)+2*C_N(zstep,xstep))/d_node*(M_NO3/rho_b);
261    del_omega_P(zstep,xstep)=(-C_P(zstep-1,xstep)-C_P(zstep+1,...
```

```
262      xstep)+2*C_P(zstep,xstep))/d_node*(M_P/rho_b);
263  else
264  a=length(z);
265  del_omega_C(a,xstep)=((C_C(a,xstep)-C_C(a-1,xstep))/d_node...
266        -(C_C_pm(1,xstep)-C_C(a,xstep))/((d_node+d_node_pm)/2))...
267        *(M_C/rho_b);
268  del_omega_O(a,xstep)=((C_O2(a,xstep)-C_O2(a-1,xstep))/d_node...
269        -(C_O2_pm(1,xstep)-C_O2(a,xstep))/((d_node+d_node_pm)/2))...
270        *(M_O2/rho_b);
271  del_omega_N(a,xstep)=((C_N(a,xstep)-C_N(a-1,xstep))/d_node...
272        -(C_N_pm(1,xstep)-C_N(a,xstep))/((d_node+d_node_pm)/2))...
273        *(M_NO3/rho_b);
274  del_omega_P(a,xstep)=((C_P(a,xstep)-C_P(a-1,xstep))/d_node...
275        -(C_P_pm(1,xstep)-C_P(a,xstep))/((d_node+d_node_pm)/2))...
276        *(M_P/rho_b);
277  clear a
278  end
279
280  if xstep==1
281  del_omega_C_x(zstep,1)=(0-(C_C(zstep,2)-C_C(zstep,1)))...
282        /d_node_x*(M_C/rho_b);
283  del_omega_O_x(zstep,1)=(0-(C_O2(zstep,2)-C_O2(zstep,1)))...
284        /d_node_x*(M_O2/rho_b);
```

```
285  del_omega_N_x(zstep,1)=(0-(C_N(zstep,2)-C_N(zstep,1)))...
286      /d_node_x*(M_NO3/rho_b);
287  del_omega_P_x(zstep,1)=(0-(C_P(zstep,2)-C_P(zstep,1)))...
288      /d_node_x*(M_P/rho_b);
289  elseif xstep<length(x)
290  del_omega_C_x(zstep,xstep)=(-C_C(zstep,xstep-1)-C_C(zstep,...
291      xstep+1)+2*C_C(zstep,xstep))/d_node_x*(M_C/rho_b);
292  del_omega_O_x(zstep,xstep)=(-C_O2(zstep,xstep-1)-C_O2(zstep,...
293      xstep+1)+2*C_O2(zstep,xstep))/d_node_x*(M_O2/rho_b);
294  del_omega_N_x(zstep,xstep)=(-C_N(zstep,xstep-1)-C_N(zstep,...
295      xstep+1)+2*C_N(zstep,xstep))/d_node_x*(M_NO3/rho_b);
296  del_omega_P_x(zstep,xstep)=(-C_P(zstep,xstep-1)-C_P(zstep,...
297      xstep+1)+2*C_P(zstep,xstep))/d_node_x*(M_P/rho_b);
298  else
299  del_omega_C_x(zstep,xstep)=(-C_C(zstep,xstep-1)-(2*C_C...
300      (zstep,xstep)-C_C(zstep,xstep-1))+2*C_C(zstep,xstep))...
301      /d_node_x*(M_C/rho_b);
302  del_omega_O_x(zstep,xstep)=(-C_O2(zstep,xstep-1)-(2*C_O2...
303      (zstep,xstep)-C_O2(zstep,xstep-1))+2*C_O2(zstep,xstep))...
304      /d_node_x*(M_O2/rho_b);
305  del_omega_N_x(zstep,xstep)=(-C_N(zstep,xstep-1)-(2*C_N...
306      (zstep,xstep)-C_N(zstep,xstep-1))+2*C_N(zstep,xstep))...
307      /d_node_x*(M_NO3/rho_b);
```

```matlab
308  del_omega_P_x(zstep,xstep)=(-C_P(zstep,xstep-1)-(2*C_P...
309      (zstep,xstep)-C_P(zstep,xstep-1))+2*C_P(zstep,xstep))...
310      /d_node_x*(M_P/rho_b);
311  end
312
313  end
314
315  for zstep=1:length(z_pm)
316  if zstep==1
317  a=length(z);
318  del_omega_C_pm(1,xstep)=((C_C_pm(1,xstep)-C_C(a,xstep))...
319      /((d_node+d_node_pm)/2)-(C_C_pm(2,xstep)-C_C_pm(1,xstep))...
320      /d_node_pm)*(M_C/rho_w);
321  del_omega_O_pm(1,xstep)=((C_O2_pm(1,xstep)-C_O2(a,xstep))...
322      /((d_node+d_node_pm)/2)-(C_O2_pm(2,xstep)-C_O2_pm(1,xstep))...
323      /d_node_pm)*(M_O2/rho_w);
324  del_omega_N_pm(1,xstep)=((C_N_pm(1,xstep)-C_N(a,xstep))...
325      /((d_node+d_node_pm)/2)-(C_N_pm(2,xstep)-C_N_pm(1,xstep))...
326      /d_node_pm)*(M_NO3/rho_w);
327  del_omega_P_pm(1,xstep)=((C_P_pm(1,xstep)-C_P(a,xstep))...
328      /((d_node+d_node_pm)/2)-(C_P_pm(2,xstep)-C_P_pm(1,xstep))...
329      /d_node_pm)*(M_P/rho_w);
330  clear a
```

172

```matlab
331  elseif zstep<length(z_pm)
332  del_omega_C_pm(zstep,xstep)=(-C_C_pm(zstep-1,xstep)...
333      -C_C_pm(zstep+1,xstep)+2*C_C_pm(zstep,xstep))...
334      /d_node_pm*(M_C/rho_w);
335  del_omega_O_pm(zstep,xstep)=(-C_O2_pm(zstep-1,xstep)...
336      -C_O2_pm(zstep+1,xstep)+2*C_O2_pm(zstep,xstep))...
337      /d_node_pm*(M_O2/rho_w);
338  del_omega_N_pm(zstep,xstep)=(-C_N_pm(zstep-1,xstep)...
339      -C_N_pm(zstep+1,xstep)+2*C_N_pm(zstep,xstep))...
340      /d_node_pm*(M_NO3/rho_w);
341  del_omega_P_pm(zstep,xstep)=(-C_P_pm(zstep-1,xstep)...
342      -C_P_pm(zstep+1,xstep)+2*C_P_pm(zstep,xstep))...
343      /d_node_pm*(M_P/rho_w);
344  else
345  a=length(z_pm);
346  del_omega_C_pm(a,xstep)=(C_C_pm(a,xstep)-C_C_pm...
347      (a-1,xstep))/d_node_pm*M_C/rho_w;
348  del_omega_O_pm(a,xstep)=(C_O2_pm(a,xstep)-C_O2_pm...
349      (a-1,xstep))/d_node_pm*M_O2/rho_w;
350  del_omega_N_pm(a,xstep)=(C_N_pm(a,xstep)-C_N_pm...
351      (a-1,xstep))/d_node_pm*M_NO3/rho_w;
352  del_omega_P_pm(a,xstep)=(C_P_pm(a,xstep)-C_P_pm...
353      (a-1,xstep))/d_node_pm*M_P/rho_w;
```

173

```matlab
354  clear a
355  end
356
357  %diffusion in x-direction in porous medium
358  if xstep==1
359  del_omega_C_pm_x(zstep,1)=(-C_C_o-C_C_pm(zstep,xstep+1)...
360      +2*C_C_pm(zstep,xstep))/d_node_x*(M_C/rho_w);
361  del_omega_O_pm_x(zstep,1)=(-C_O2_o-C_O2_pm(zstep,xstep+1)...
362      +2*C_O2_pm(zstep,xstep))/d_node_x*(M_O2/rho_w);
363  del_omega_N_pm_x(zstep,1)=(-C_N_o-C_N_pm(zstep,xstep+1)...
364      +2*C_N_pm(zstep,xstep))/d_node_x*(M_NO3/rho_w);
365  del_omega_P_pm_x(zstep,1)=(-C_P_o-C_P_pm(zstep,xstep+1)...
366      +2*C_P_pm(zstep,xstep))/d_node_x*(M_P/rho_w);
367  elseif xstep<length(x)
368  del_omega_C_pm_x(zstep,xstep)=(-C_C_pm(zstep,xstep-1)...
369      -C_C_pm(zstep,xstep+1)+2*C_C_pm(zstep,xstep))...
370      /d_node_x*(M_C/rho_w);
371  del_omega_O_pm_x(zstep,xstep)=(-C_O2_pm(zstep,xstep-1)...
372      -C_O2_pm(zstep,xstep+1)+2*C_O2_pm(zstep,xstep))...
373      /d_node_x*(M_O2/rho_w);
374  del_omega_N_pm_x(zstep,xstep)=(-C_N_pm(zstep,xstep-1)...
375      -C_N_pm(zstep,xstep+1)+2*C_N_pm(zstep,xstep))...
376      /d_node_x*(M_NO3/rho_w);
```

```matlab
377 del_omega_P_pm_x(zstep,xstep)=(-C_P_pm(zstep,xstep-1)...
378     -C_P_pm(zstep,xstep+1)+2*C_P_pm(zstep,xstep))...
379     /d_node_x*(M_P/rho_w);
380 else
381 del_omega_C_pm_x(zstep,xstep)=(-C_C_pm(zstep,xstep-1)...
382     -(2*C_C_pm(zstep,xstep)-C_C_pm(zstep,xstep-1))...
383     +2*C_C_pm(zstep,xstep))/d_node_x*(M_C/rho_w);
384 del_omega_O_pm_x(zstep,xstep)=(-C_O2_pm(zstep,xstep-1)...
385     -(2*C_O2_pm(zstep,xstep)-C_O2_pm(zstep,xstep-1))...
386     +2*C_O2_pm(zstep,xstep))/d_node_x*(M_O2/rho_w);
387 del_omega_N_pm_x(zstep,xstep)=(-C_N_pm(zstep,xstep-1)...
388     -(2*C_N_pm(zstep,xstep)-C_N_pm(zstep,xstep-1))...
389     +2*C_N_pm(zstep,xstep))/d_node_x*(M_NO3/rho_w);
390 del_omega_P_pm_x(zstep,xstep)=(-C_P_pm(zstep,xstep-1)...
391     -(2*C_P_pm(zstep,xstep)-C_P_pm(zstep,xstep-1))...
392     +2*C_P_pm(zstep,xstep))/d_node_x*(M_P/rho_w);
393 end
394
395 %advection in porous medium
396 if xstep==1
397 adv_C_pm(zstep,1)=u_p*f_v*d_node_pm...
398     *(C_C_o-C_C_pm(zstep,1))*1000;
399 adv_O2_pm(zstep,1)=u_p*f_v*d_node_pm...
```

```matlab
400        *(C_O2_o-C_O2_pm(zstep,1))*1000;
401   adv_N_pm(zstep,1)=u_p*f_v*d_node_pm...
402        *(C_N_o-C_N_pm(zstep,1))*1000;
403   adv_P_pm(zstep,1)=u_p*f_v*d_node_pm...
404        *(C_P_o-C_P_pm(zstep,1))*1000;
405   else
406   adv_C_pm(zstep,xstep)=u_p*f_v*d_node_pm*(C_C_pm...
407        (zstep,xstep-1)-C_C_pm(zstep,xstep))*1000;
408   adv_O2_pm(zstep,xstep)=u_p*f_v*d_node_pm*(C_O2_pm...
409        (zstep,xstep-1)-C_O2_pm(zstep,xstep))*1000;
410   adv_N_pm(zstep,xstep)=u_p*f_v*d_node_pm*(C_N_pm...
411        (zstep,xstep-1)-C_N_pm(zstep,xstep))*1000;
412   adv_P_pm(zstep,xstep)=u_p*f_v*d_node_pm*(C_P_pm...
413        (zstep,xstep-1)-C_P_pm(zstep,xstep))*1000;
414   end
415
416   end %of z-loop
417
418   end %of x-loop
419
420   %calculate rates of diffusion mass transfer in biofilm (mols/s)
421   j_C=-rho_b*D_C_b.*del_omega_C*1000*d_node_x/M_C;
422   j_O2=-rho_b*D_O2_b.*del_omega_O*1000*d_node_x/M_O2;
```

```matlab
423    j_N=-rho_b*D_NO3_b.*del_omega_N*1000*d_node_x/M_NO3;

424    j_P=-rho_b*D_P_b.*del_omega_P*1000*d_node_x/M_P;

425

426    j_C_x=-rho_b*D_C_b.*del_omega_C_x*1000*d_node/M_C;

427    j_O2_x=-rho_b*D_O2_b.*del_omega_O_x*1000*d_node/M_O2;

428    j_N_x=-rho_b*D_NO3_b.*del_omega_N_x*1000*d_node/M_NO3;

429    j_P_x=-rho_b*D_P_b.*del_omega_P_x*1000*d_node/M_P;

430

431    %calculate changes in concentrations of elements

432    C_C=C_C+time_step.*(j_C+j_C_x-cons_C)...

433        /(d_node*d_node_x*1000);

434    C_O2=C_O2+time_step.*(j_O2+j_O2_x-cons_O)...

435        /(d_node*d_node_x*1000);

436    C_N=C_N+time_step.*(j_N+j_N_x-cons_N)...

437        /(d_node*d_node_x*1000);

438    C_P=C_P+time_step.*(j_P+j_P_x-cons_P)...

439        /(d_node*d_node_x*1000);

440

441    %fluxes and changes in concentrations in porous medium (mol/s)

442    j_C_pm=-rho_w*D_C_pm.*del_omega_C_pm*1000*d_node_x/M_C;

443    j_O2_pm=-rho_w*D_O2_pm.*del_omega_O_pm*1000*d_node_x/M_O2;

444    j_N_pm=-rho_w*D_NO3_pm.*del_omega_N_pm*1000*d_node_x/M_NO3;

445    j_P_pm=-rho_w*D_P_pm.*del_omega_P_pm*1000*d_node_x/M_P;
```

```matlab
446
447  j_C_pm_x=-rho_w*D_C_pm.*del_omega_C_pm_x*1000*d_node_pm/M_C;

448  j_O2_pm_x=-rho_w*D_O2_pm.*del_omega_O_pm_x*1000*d_node_pm/M_O2;

449  j_N_pm_x=-rho_w*D_NO3_pm.*del_omega_N_pm_x*1000*d_node_pm/M_NO3;

450  j_P_pm_x=-rho_w*D_P_pm.*del_omega_P_pm_x*1000*d_node_pm/M_P;

451
452  C_C_pm=C_C_pm+time_step*(j_C_pm+j_C_pm_x+adv_C_pm)...

453      /(d_node_pm*d_node_x*1000);

454  C_O2_pm=C_O2_pm+time_step*(j_O2_pm+j_O2_pm_x+adv_O2_pm)...

455      /(d_node_pm*d_node_x*1000);

456  C_N_pm=C_N_pm+time_step*(j_N_pm+j_N_pm_x+adv_N_pm)...

457      /(d_node_pm*d_node_x*1000);

458  C_P_pm=C_P_pm+time_step*(j_P_pm+j_P_pm_x+adv_P_pm)...

459      /(d_node_pm*d_node_x*1000);

460
461  %check if any concentration is less than zero.

462  %If so, set it to zero

463  [C_C,C_O2,C_N,C_P,C_C_pm,C_O2_pm,C_N_pm,C_P_pm]...

464      =checkzero(C_C,C_O2,C_N,C_P,C_C_pm,C_O2_pm,...

465      C_N_pm,C_P_pm,x,z,z_pm);

466
467  %record only at set time intervals (for transient analysis)

468  if record_counter==record_interval
```

```matlab
469   timestamp(save_matrix)=time;

470   time

471   mu_sparse(:,:,save_matrix)=mu;

472   C_C_sparse(:,:,save_matrix)=C_C;

473   C_O2_sparse(:,:,save_matrix)=C_O2;

474   C_N_sparse(:,:,save_matrix)=C_N;

475   C_P_sparse(:,:,save_matrix)=C_P;

476   record_counter=0;

477   save_matrix=save_matrix+1;

478   end

479

480   end %of time loop

481

482   %record data

483   paramlist=[u_p,L_pm,C_P_o,G_total,biofilm_thickness];

484   data_array{1,counter}=paramlist;

485   data_array{2,counter}=x;

486   data_array{3,counter}=z;

487   data_array{4,counter}=mu;

488   data_array{5,counter}=C_C;

489   data_array{6,counter}=C_O2;

490   data_array{7,counter}=C_N;

491   data_array{8,counter}=C_P;
```

179

```matlab
492  data_array{9,counter}=pH;

493

494  %save data
495  save('base_case','data_array');

496

497  %end parameter sweep loops (if necessary)
498  end
499  end
500  end
501  end
502  end
503  end
```

E.2   Diffusive permeabilities

```matlab
1  function [D_CO2_b,D_HCO3_b,D_NO3_b,D_HPO4_b,...
2      D_H2PO4_b,D_O2_b,D_CO2_pm,D_HCO3_pm,...
3      D_NO3_pm,D_HPO4_pm,D_H2PO4_pm,D_O2_pm]...
4      =diffusive_permeabilities(biomass_density,f_v)

5

6  %diffusion coefficients in water in m2/s
7  D_CO2_w=1.92e-9;
8  D_HCO3_w=1.18e-9;
```

```
 9  D_O2_w=2.0e-9;

10  D_NO3_w=1.7e-9;

11  D_H2PO4_w=0.88e-9;

12  D_HPO4_w=0.76e-9;

13  D_SO4_w=1.06e-9;

14

15  %calculate relative diffusivity

16  D_frac_CO2=1-0.43*biomass_density^0.92...

17      /(11.19+0.27*biomass_density^0.99);

18  D_frac_HCO3=D_frac_CO2;

19  D_frac_O2=D_frac_CO2;

20  D_frac_NO3=D_frac_CO2;

21  D_frac_HPO4=D_frac_CO2;

22  D_frac_H2PO4=D_frac_CO2;

23  D_frac_SO4=D_frac_CO2;

24

25  %calculate diffusive permeability in biofilm

26  D_CO2_b=D_frac_CO2*D_CO2_w;

27  D_HCO3_b=D_frac_HCO3*D_HCO3_w;

28  D_O2_b=D_frac_O2*D_O2_w;

29  D_NO3_b=D_frac_NO3*D_NO3_w;

30  D_HPO4_b=D_frac_HPO4*D_HPO4_w;

31  D_H2PO4_b=D_frac_H2PO4*D_H2PO4_w;
```

```
32

33    %calculate diffusive permeabilities in porous medium

34    D_CO2_pm=f_v*D_CO2_w;

35    D_HCO3_pm=f_v*D_HCO3_w;

36    D_O2_pm=f_v*D_O2_w;

37    D_NO3_pm=f_v*D_NO3_w;

38    D_HPO4_pm=f_v*D_HPO4_w;

39    D_H2PO4_pm=f_v*D_H2PO4_w;
```

E.3   Dominant species

```
1     function [D_C_b,D_C_pm,M_C,D_P_b,D_P_pm,M_P]...

2         =dominant_species(pH,D_CO2_b,D_CO2_pm,...

3         M_CO2,D_HCO3_b,D_HCO3_pm,M_HCO3,D_H2PO4_b,...

4         D_H2PO4_pm,M_H2PO4,D_HPO4_b,D_HPO4_pm,M_HPO4)

5

6     if pH<6.3

7         D_C_b=D_CO2_b;

8         D_C_pm=D_CO2_pm;

9         M_C=M_CO2;

10    else

11        D_C_b=D_HCO3_b;

12        D_C_pm=D_HCO3_pm;
```

```
13        M_C=M_HCO3;
14    end
15
16    if pH<7.2
17        D_P_b=D_H2PO4_b;
18        D_P_pm=D_H2PO4_pm;
19        M_P=M_H2PO4;
20    else
21        D_P_b=D_HPO4_b;
22        D_P_pm=D_HPO4_pm;
23        M_P=M_HPO4;
24    end
```

Appendix F

Matlab script for the vascular system modeling study (Chapter 4)

This code calculates the critical wetting length and total flow rate through a single rib of a Porous Substrate Bioreactor. First, the code uses an energy balance to iteratively solve for the water temperature at the membrane surface. It then uses that temperature to determine the evaporative flux, critical wetting length, and flow rate through the rib.

```matlab
1  clear
2
3  %load constants
4  R=8.314; %J/mol-K
5  M_w=18; %g/mol
6  M_a=29; %g/mol
7  g=9.8; %m/s2
8  rho_w=1000; %kg/m3
9  load('properties');%saturation pressure of water vapor,
10 % water viscosity
11
```

```matlab
12    %absorptance of exposed porous membrane
13    alpha=0.3;
14
15    P_a=101325; %Pa
16
17    h1=0.02;
18    he=0.015;
19
20    %set weather parameters
21    load('weather');
22    for season=2:2;
23        membrane=2;
24
25        for hour=1:24
26            RH=weather(hour,2,season);
27            v_wind=weather(hour,3,season); %m/s
28            T_a=weather(hour,4,season); %K
29            G_rib=weather(hour,5,season); %W/m2
30
31            P_sat_inf=interp1(properties(:,1),properties(:,2),T_a);
32            omega_inf=RH*M_w/M_a*P_sat_inf/(P_a-P_sat_inf);
33
34            %guess length scale
```

```matlab
35          L=0.1; %m

36          xc=0.2;

37          while abs((L-xc)/xc)>0.05

38              L=xc;

39

40              %iterate to find the

41              %temperature of exposed porous medium

42              T_w=T_a-20;

43              LHS=1;

44              while (isnan(LHS)==1 || LHS>0)

45

46                  %water properties

47                  mu_w=interp1(properties(:,1),...

48                      properties(:,3),T_w); %Pa-s

49                  sigma_w=interp1(properties(:,1),...

50                      properties(:,4),T_w);

51                  h_fg=interp1(properties(:,1),...

52                      properties(:,5),T_w);

53

54                  %calculate film temperature

55                  T_f=(T_a+T_w)/2;

56

57                  %air properties
```

```matlab
58          rho_a=P_a*M_a/(R*T_f)/1000;

59          D_wa=0.187e-9*T_f^2.072; %m2/s

60          nu_a=10^-6*(11.44+(T_f-250)*(15.89-11.44)/50);

61          k_a=10^-3*(22.3+(T_f-250)*(26.3-22.3)/50);

62          cp_a=1007; %J/kgK, assume constant

63          alpha_a=k_a/(rho_a*cp_a);

64          Sc=nu_a/D_wa;

65          Pr=nu_a/alpha_a;

66          beta=1/T_f; %1/K

67          P_sat_surf=interp1(properties(:,1),...

68              properties(:,2),T_w);

69          omega_s=M_w/M_a*P_sat_surf/(P_a-P_sat_surf);

70

71          %forced convection dimensionless groups

72          Lf=10;

73          Re=Lf*v_wind/nu_a;

74          if Re>5e5

75              Sh_f=(0.037*Re^0.8-871)*Sc^(1/3);

76              Nu_f=(0.037*Re^0.8-871)*Pr^(1/3);

77          else

78              Sh_f=0.664*Re^0.5*Sc^(1/3);

79              Nu_f=0.664*Re^0.5*Pr^(1/3);

80          end
```

```matlab
%natural convection dimensionless groups
Gr=g*beta*abs(T_w-T_a)*L^3/nu_a^2;

%for horizontal plates
%    if T_w<T_a(j)
%        Sh_n=0.27*Sc^0.25*Gr^0.25;
%        Nu_n=0.27*Pr^0.25*Gr^0.25;
%    else
%        Sh_n=0.15*Sc^(1/3)*Gr^(1/3);
%        Nu_n=0.15*Pr^(1/3)*Gr^(1/3);
%    end

%vertical plate
Sh_n=0.68+0.67*Sc^0.25*Gr^0.25...
    /(1+(0.492/Sc)^(9/16))^(4/9);
Nu_n=0.68+0.67*Pr^0.25*Gr^0.25...
    /(1+(0.492/Pr)^(9/16))^(4/9);

Sh=(Sh_f^3.5+Sh_n^3.5)^(2/7);
Nu=(Nu_f^3.5+Nu_n^3.5)^(2/7);

Nusum=Nu_f+Nu_n;
```

188

```
104            Lc=Nu_f/Nusum*Lf+Nu_n/Nusum*L;

105

106            kw=Sh*rho_a*D_wa/Lc; %kg/m2-s

107            h=Nu*k_a/Lc;

108

109            solar_flux=alpha*G_rib;

110            evap_flux=kw*(omega_s-omega_inf)*h_fg;

111            mdot_e=evap_flux/h_fg;

112            convective_flux=h*(T_a-T_w);

113            T_s=T_w;

114

115            LHS = solar_flux - evap_flux + convective_flux;

116

117            T_w=T_w+0.1;
118        end

119

120        %calculate critical wetting length

121

122        if membrane==1
123            t=0.13e-3; %m
124            r=0.65e-6; %m
125            f_v=0.7;
126            costheta=cos(55*pi/180);
```

```matlab
        elseif membrane==2
            t=0.33e-3; %m
            r=1.5e-6; %m
            f_v=0.85;
            costheta=cos(20*pi/180);
        elseif membrane==3
            t=0.2e-3; %m
            r=20e-6; %m
            f_v=0.87;
            costheta=cos(39*pi/180);
        end
        k=1/8*f_v^(4/3)*r^2; %permeability in m2

        P_c=2*costheta/r*sigma_w;
        aq=-mu_w*mdot_e/(t*k*rho_w);
        bq=-rho_w*g-2*mdot_e*mu_w*h1/(t*k*rho_w);
        cq=P_c-rho_w*g*h1;
        xc=max((-bq-sqrt(bq^2-4*aq*cq))/(2*aq),...
            (-bq+sqrt(bq^2-4*aq*cq))/(2*aq));
    end

    %calculate total mass flow rate
    if xc<he
```

```matlab
150            mdot_t=2*mdot_e*xc %kg/s-m
151        else
152            mdot_t=2*mdot_e*he;
153        end
154        Q_t=mdot_t; %L/s-m
155        u_p=mdot_t/(rho_w*t); %m/s
160    end
161 end
```

Appendix G

Matlab script for image analysis of biofilms (Chapter 5)

This code is used to measure the red, green, and blue coefficients of a given set of biofilms. First, the user crops a white reference region of the image. Then, the user crops a green biofilm region. The code calculates the red, green, and blue coefficients of the image as their respective values in the green region divided by their values in the white region. Used in conjunction with known biomass densities of the biofilms, this code is used to generate a calibration curve between green value and biomass concentration.

```matlab
1   clear
2
3   %specify image numbers (previously labeled)
4   image_numbers=[0:3,6:3:42,43,44]';
5
6   for index=1:length(image_numbers)
7
8       %get image of biofilm
9       number_string=num2str(image_numbers(index));
```

```matlab
10      filename=[number_string 'mL B.jpg'];

11      image(:,:,:)=imread(filename);

12

13      %user crops white region

14      icrop_w=imcrop(image);

15

16      %calculate r,g,b values of white region

17      r_w(index,1)=mean(mean(icrop_w(:,:,1)));

18      g_w(index,1)=mean(mean(icrop_w(:,:,2)));

19      b_w(index,1)=mean(mean(icrop_w(:,:,3)));

20

21      clear icrop

22

23      %now crop green region

24      icrop=imcrop(image);

25

26      %calculate r,g,b of green region

27      r(index,1)=mean(mean(icrop(:,:,1)));

28      g(index,1)=mean(mean(icrop(:,:,2)));

29      b(index,1)=mean(mean(icrop(:,:,3)));

30

31      %normalize r,g,b of green region w/r,g,b of white

32      g_n(index,1)=g(index,1)/g_w(index,1);
```

```
33     r_n(index,1)=r(index,1)/r_w(index,1);

34     b_n(index,1)=b(index,1)/b_w(index,1);

35

36     clear image

37

38  end
```

Appendix H

Matlab script for spatial biomass concentration analysis using imaging method (Chapter 6)

This code accepts as an input a set of biofilm images. It then calculates the biomass density of each image as a function of location using the previously generated calibration curve between the green value of the region and the biomass density. This code enables remote measurement of spatially and temporally dependent biomass concentration of Porous Substrate Biroeactors.

```
1   clear
2
3   %set inoculation time
4   inoc_month=3;
5   inoc_date=5;
6   inoc_hour=14;
7   inoc_minute=25;
8
9   %width of growth region
10  w_strip=0.5*2.54/100; %m
11
```

```matlab
12   %length of growth region
13   x_standard=0.02; %m
14
15   %identify picture filenames
16   chamber_number=2;
17   chamber_number_string=num2str(chamber_number);
18   loadstring=['chamber_' chamber_number_string '_data'];
19   load(loadstring);
20
21   picture_month=4;
22   month_string=['0',num2str(picture_month)];
23
24   %specify names of pictures (named by chamber, date and time)
25   if chamber_number==1
26       picture_day=[5,6,6,7,7,8,8,9,11,12,12,13,13,14,15,16,...
27           18,19,20,21,22,23,25,26,26,27,28,29,30,1,2,4,8];
28       picture_hour=[19,9,16,10,17,11,17,21,14,10,19,10,20,14,...
29           11,13,13,20,18,12,13,19,9,9,19,14,17,15,18,17,17,18,16];
30       picture_minute=[59,47,25,42,51,13,25,12,25,11,37,35,45,...
31           37,55,19,57,26,51,27,1,15,57,38,13,10,57,21,17,55,...
32           30,39,32];
33   elseif chamber_number==2
34       picture_day=[5,6,6,7,7,8,8,9,11,12,13,13,14,15,16,18,19,...
```

196

```matlab
35          20,21,22,23,25,26,26,27,28,29,1,2,4,8];
36      picture_hour=[20,9,16,10,17,11,17,21,14,19,10,20,14,11,...
37          13,13,20,18,12,13,19,9,9,19,14,17,15,17,17,18,16];
38      picture_minute=[0,47,25,42,52,13,25,12,24,37,35,45,37,...
39          55,19,57,26,51,27,1,15,57,38,13,10,57,21,55,30,39,32];
40  else
41      picture_day=[5,6,6,7,7,8,8,9,11,12,12,13,13,14,15,16,18,...
42          19,20,21,22,23,25,26,26,27,28,29,30,1,2,4,8];
43      picture_hour=[20,9,16,10,17,11,17,21,14,10,19,10,20,14,...
44          11,13,13,20,18,12,13,19,9,9,19,14,17,15,18,17,17,18,16];
45      picture_minute=[0,48,25,42,52,13,25,12,24,11,37,35,45,37,...
46          55,19,57,26,51,27,1,15,57,38,13,10,57,21,17,55,30,39,32];
47  end
48
49  %load constants for correlating biomass to green value
50  a=-39.53;
51  b=35.10;
52
53  max_index_time=6
54  for index_time=30:31
55
56      %calculate time of picture
57      absolute_time(index_time)=24*30*(picture_month...
```

```matlab
58          -inoc_month)+24*(picture_day(index_time)...
59          -inoc_date)+(picture_hour(index_time)-inoc_hour)...
60          +1/60*(picture_minute(index_time)-inoc_minute);
61
62      %convert times to string for filename acquisition
63      day_string=num2str(picture_day(index_time));
64      if length(day_string)==1
65          day_string=['0',day_string];
66      end
67
68      hour_string=num2str(picture_hour(index_time));
69      if length(hour_string)==1
70          hour_string=['0',hour_string];
71      end
72
73      minute_string=num2str(picture_minute(index_time));
74      if length(minute_string)==1
75          minute_string=['0',minute_string];
76      end
77
78      %generate filename and convert image
79      filename=[chamber_number_string,' ',month_string,...
80          day_string,' ',hour_string,minute_string,'.jpg']
```

```
81      image(:,:,:)=imread(filename);

82

83      %crop white region for reference
84      clear white_crop; clear white_crop_double
85      white_crop=imcrop(image);
86      white_crop_double=im2double(white_crop);
87      white_ref=mean(mean(white_crop_double(:,:,2)));

88

89      %crop biofilm region
90      biofilm_crop=imcrop(image);

91

92      %identify width of filter paper as length reference
93      %and orientation
94      imshow(biofilm_crop);
95      [x1,y1]=ginput(2);
96      pixel_conversion=w_strip/((x1(1)-x1(2))...
97          ^2+(y1(1)-y1(1))^2)^0.5; %m

98

99      %pre-allocate matrices
100     isgreen=zeros(length(biofilm_crop(:,1,1))...
101         ,length(biofilm_crop(1,:,1)));
102     g_n=zeros(length(biofilm_crop(:,1,1)),...
103         length(biofilm_crop(1,:,1)));
```

```matlab
104     X_A=zeros(length(biofilm_crop(:,1,1)),...
105         length(biofilm_crop(1,:,1)));
106     biofilm_crop_double=im2double(biofilm_crop);
107
108     %identify green region using threshold
109     for i=1:length(biofilm_crop(:,1,1))
110         for j=1:length(biofilm_crop(1,:,1))
111             if biofilm_crop_double(i,j,2)...
112                     /((biofilm_crop_double(i,j,1)...
113                     +biofilm_crop_double(i,j,3))/2)>1.25
114                 isgreen(i,j)=1;
115                 g_n(i,j)=biofilm_crop_double(i,j,2)/white_ref;
116                 X_A(i,j)=a*g_n(i,j)+b;
117             else
118                 X_A(i,j)=0;
119             end
120             if X_A(i,j)<0
121                 X_A(i,j)=0;
122             end
123         end
124     end
125
126     %sparse X_A
```

```matlab
127      sparsing_param=10;
128      clear y2; clear x2; clear X_A_sparse;
129      clear isgreen_sparse; clear g_n_sparse;
130      for i=1:floor(length(biofilm_crop_double(:,1,1))...
131              /sparsing_param)
132          for j=1:floor(length(biofilm_crop_double(1,:,1))...
133                  /sparsing_param)
134              X_A_sparse(i,j)=mean(mean((X_A(1+(i-1)...
135                  *sparsing_param:i*sparsing_param,...
136                  1+(j-1)*sparsing_param:j*sparsing_param))));
137              isgreen_sparse(i,j)=mean(mean((isgreen...
138                  (1+(i-1)*sparsing_param:i*sparsing_param,...
139                  1+(j-1)*sparsing_param:j*sparsing_param))));
140              g_n_sparse(i,j)=mean(mean((g_n(1+(i-1)...
141                  *sparsing_param:i*sparsing_param,1+(j-1)...
142                  *sparsing_param:j*sparsing_param))));
143              y2(i)=(i-1)*sparsing_param+5;
144              x2(j)=(j-1)*sparsing_param+5;
145          end
146      end
147
148      %conversion to absolute scale
149
```

```
150    %calculate slopes of lines defining
151    %leading edge of filter paper and
152    %side of filter paper
153    m1=(y1(2)-y1(1))/(x1(2)-x1(1));
154    m2=-1/m1;
155
156    clear x3; clear y3; clear xprime; clear yprime;
157
158    %(x3,y3) is the location where the line between (x2,y2)
159    %and the paper leading edge intersects the leading edge.
160    %(xprime,yprime) is the position of (x2,y2) in the
161    %coordinate system defined by the paper leading edge
162    for i=1:length(y2)
163        for j=1:length(x2)
164            x3(i,j)=(y2(i)-m2*x2(j)+m1*x1(1)-y1(1))/(m1-m2);
165            y3(i,j)=m1*x3(i,j)-m1*x1(1)+y1(1);
166            if y2(i)<y3(i,j)
167                xprime(i,j)=-((y3(i,j)-y2(i))...
168                    ^2+(x3(i,j)-x2(j))^2)^0.5;
169            else
170                xprime(i,j)=((y3(i,j)-y2(i))...
171                    ^2+(x3(i,j)-x2(j))^2)^0.5;
172            end
```

```matlab
173            if x3(i,j)<x1(1)
174                    yprime(i,j)=-((y3(i,j)-y1(1))^2+(x3...
175                        (i,j)-x1(1))^2)^0.5;
176            else
177                    yprime(i,j)=((y3(i,j)-y1(1))^2+(x3...
178                        (i,j)-x1(1))^2)^0.5;
179            end
180        end
181    end
182
183
184    %xspan and yspan are evenly spaced vectors
185    %that span the space of (xprime,yprime)
186    clear xspan; clear yspan;
187
188    xspan=[0:max(max(xprime))/(length(xprime(:,1))-1)...
189        :max(max(xprime))];
190    yspan=[0:max(max(yprime))/(length(yprime(1,:))-1)...
191        :max(max(yprime))];
192
193    %find the biofilm growth rate at (xspan,yspan)
194    clear findlocation; clear X_A_global;
195    clear isgreen_global; clear g_n_global
```

203

```matlab
196         for i=1:length(xspan)
197             for j=1:length(yspan)
198                 for m=1:length(xprime(:,1))
199                     for n=1:length(yprime(1,:))
200                         findlocation(m,n)=abs(xspan(i)...
201                             -xprime(m,n))+abs(yspan(j)...
202                             -yprime(m,n));
203                     end
204                 end
205                 [minval,ind] = min(findlocation(:));
206                 [I,J] = ind2sub([size(findlocation,1) size...
207                     (findlocation,2)],ind);
208                 X_A_global(i,j)=X_A_sparse(I,J);
209                 isgreen_global(i,j)=isgreen_sparse(I,J);
210                 g_n_global(i,j)=g_n_sparse(I,J);
211             end
212         end
213
214     %convert pixels to mm
215     clear x_mm; clear y_mm;
216     x_mm=xspan*pixel_conversion*1000;
217     y_mm=yspan*pixel_conversion*1000;
218
```

```matlab
219     %chop the X_A_final matrix so they all

220     %have the same dimensions

221     counter=1;

222     clear y_mm_chop; clear X_A_global_chop;

223     clear isgreen_global_chop; clear g_n_global_chop;

224     while y_mm(counter)<w_strip*1000

225         y_mm_chop(counter)=y_mm(counter);

226         X_A_global_chop(:,counter)=X_A_global(:,counter);

227         isgreen_global_chop(:,counter)=isgreen_global(:,counter);

228         g_n_global_chop(:,counter)=g_n_global(:,counter);

229         counter=counter+1;

230     end


232     counter=1;

233     clear x_mm_chop; clear X_A_final;

234     clear isgreen_final; clear g_n_final;

235     while x_mm(counter)<x_standard*1000;

236         x_mm_chop(counter)=x_mm(counter);

237         X_A_final(counter,:)=X_A_global_chop(counter,:);

238         isgreen_final(counter,:)=isgreen_global_chop(counter,:);

239         g_n_final(counter,:)=g_n_global_chop(counter,:);

240         counter=counter+1;

241     end
```

```matlab
242
243     %calculate total biomass and green area
244     S=size(X_A_final);
245     total_biomass=sum(sum(X_A_final))*w_strip...
246         *x_standard/(S(1)*S(2));
247     green_area=sum(sum(isgreen_final))*w_strip...
248         *x_standard/(S(1)*S(2));
249     strip_area=w_strip*x_standard;
250
251     %store data
252     data_array{1,index_time}=absolute_time(index_time);
253     data_array{2,index_time}=total_biomass;
254     data_array{3,index_time}=green_area;
255     data_array{4,index_time}=x_mm_chop;
256     data_array{5,index_time}=y_mm_chop;
257     data_array{6,index_time}=X_A_final;
258     data_array{7,index_time}=g_n_final;
259     data_array{8,index_time}=isgreen_final;
260
261     %save data
262     saveasstring=['chamber_' chamber_number_string '_data'];
263     save(saveasstring,'data_array');
264
```

```
265   end
266
267   % run plotting
```

Appendix I

Patents, articles, and presentations

I.1 Patents

- Berberoglu H., <u>Murphy T.</u>, Bebout L., and Fleming E. 2013. Capillary driven micro-organism cultivation platform for human life support. Serial number 13/929,646. Application filed June 27, 2013.

I.2 Peer-reviewed journal articles

- <u>Murphy T.</u> and Berberoglu H., 2013. Flux balancing of light and nutrients in a biofilm photobioreactor for maximizing photosynthetic productivity, *Biotechnology Progress* (in review).

- Crawford R., <u>Murphy T.</u>, da Silva A.K. and Berberoglu H., 2013. Experimental characterization of geometric parameters on evaporative pumping, *Experimental Thermal and Fluid Science*, http://dx.doi.org/10.1016 /j.expthermflusci.2013.07.013.

- <u>Murphy T.</u>, Macon K. and Berberoglu H., 2013. Multispectral image analysis for algal biomass quantification, *Biotechnology Progress*, vol. 29, no. 3, pp. 808-816.

- Crawford R., <u>Murphy T.</u>, da Silva A.K, and Berberoglu H. Pumpless

evaporative cooling of actively heated surfaces, *Energy and Buildings*, vol. 62, pp. 217-221.

- Murphy T. and Berberoglu H., 2012. Temperature Fluctuation and Evaporative Loss Rate in an Algae Biofilm Photobioreactor, *Journal of Solar Energy Engineering*, vol. 134, no. 1.

- Murphy T. and Berberoglu H., 2011. Effect of algae pigmentation on photobioreactor productivity and scale-up: A light transfer perspective. *Journal of Quantitative Spectroscopy and Radiative Transfer*, vol. 112, no. 18, pp. 2826-34.

I.3 Peer-reviewed articles in conference proceedings

- Taylan O., Murphy T., and Berberoglu H., 2013, Light transport analysis of smart windows for solar energy harvesting, *7th International Symposium on Radiative Transfer*, Kusadasi, Turkey, June 2-8.

- Murphy T., Fleming E., Bebout L., Bebout B., and Berberoglu H., 2012. A Novel Microbial Cell Cultivation Platform for Space Applications, *1st Annual International Space Station (ISS) Research and Development Conference*, Denver, CO, USA, June 26-28.

- Murphy T., Macon K. and Berberoglu H., 2012. An Image Processing Technique to Recover the Biomass Concentration in Algae Biofilm Photobioreactors, *ASME 2012 Summer Heat Transfer Conference*, Puerto Rico, USA, July 8-12, HT2012-58422.

- Murphy T. and Berberoglu H., 2011. Cellular Photosynthetic Rate of

Fully and Partially Pigmented Chlamydomonas reinhardtii as a Function of Irradiance, *ASME 2011 International Mechanical Congress and Exposition*, Denver, CO, November 11-17, IMECE2011-64550.

- Murphy T. and Berberoglu H., 2011. Transient Analysis of Microorganism Temperature and Evaporative Losses in an Algae Biofilm Photobioreactor, *ASME/JSME 8th Thermal Engineering Joint Conference*, Honolulu, Hawaii, March 13-17, AJTEC2011-44347.

- Murphy T. and Berberoglu H., 2010. Increased Photobioreactor Productivity Using Algae with Low Pigmentation: A Light Transfer Perspective, *ASME 2010 International Mechanical Congress and Exposition*, Vancouver, British Columbia, November 12-18, IMECE2010-39482.

I.4 Oral presentations

- Murphy T., Macon K., and Berberoglu H. A novel multispectral image analysis technique for monitoring the productivity of open pond algae cultivation systems. *ASME 2013 Summer Heat Transfer Conference*, Minneapolis, MN, USA, July 17, 2013.

- Murphy T. and Berberoglu H. Photon and nutrient flux balancing in a synthetic leaf for maximizing photosynthetic productivity. *ASME 2013 Summer Heat Transfer Conference*, Minneapolis, MN, USA, July 18, 2013.

- Berberoglu H., Murphy T., and Kulkarni A. Natural versus Artificial Light Usage in Algal Cultivation. *Algae Biomass Summit*, Denver, CO,

USA, September 24-27, 2012.

- <u>Murphy T.</u>, Fleming E., Prufert-Bebout L., Bebout B., and Berberoglu H. Algae bioproduct harvesting using synthetic trees: The Surface-Adhering Bioreactor (SABR) (poster). *Algae Biomass Summit*, Denver, CO, USA, September 24-27, 2012.

Bibliography

[1] S. Adham, K-P. Chiu, G. Lehman, C. Mysore, and J. Clouet. *Optimization of membrane treatment for direct and clarified water filtration.* American Waterworks Foundation, New York, 1st edition, 2006.

[2] P. Albertano, L. Bruno, D.D. Ottavi, D. Moscone, and G. Palleschi. Effect of photosynthesis on pH variation in cyanobacterial biofilms from Roman catacombs. *J Appl Phycol*, 12:379–384, 2000.

[3] R.A. Andersen. *Algal Culturing Techniques.* Elsevier Academic Press, London, 2005.

[4] L.A. Anderson. On the hydrogen and oxygen content of marine phytoplankton. *Deep-Sea Res Pt I*, 42(9):1675–1680, 1995.

[5] J. Asenjo and J. Merchuk. *Bioreactor System Design.* Marcel Dekker, New York, 1995.

[6] D. Baillis, L. Pilon, H. Randrianalisoa, R. Gomez, and R. Viskanta. Measurements of radiation characteristics of fused quartz containing bubbles. *J Opt Soc Am*, 21(1):149–159, 2004.

[7] R. Bakke, R. Kommedal, and S. Kalvenes. Quantification of biofilm accumulation by an optical approach. *J Microbiol Meth*, 44:13–26, 2001.

[8] R. Bakke and P.Q. Olsson. Biofilm thickness measurements by light microscopy. *J Microbiol Meth*, 5:93–98, 1986.

[9] C.M. Beal, R.E. Hebner, M.E. Webber, R.S. Ruoff, and A.F. Seibert. The energy return on investment for algal biocrude: results for a research production facility. *Bioenerg Res*, 5:341–362, 2011.

[10] C.M. Beal, C.H. Smith, M.E. Webber, R.S. Ruoff, and R.E. Hebner. A framework to report the production of renewable diesel from algae. *Bioenerg Res*, 4:36–60, 2011.

[11] E.W. Becker. *Microalgae biotechnology and microbiology*. Cambridge University Press, Cambridge, 1994.

[12] L. Beer, E. Boyd, J. Peters, and M. Posewitz. Engineering algae for biohydrogen and biofuel production. *Curr Opin Biotech*, 20(3):264–271, 2009.

[13] H. Berberoglu, H. Barra, L. Pilon, and J. Jay. Growth, CO_2 consumption, and H_2 production of *Anabaena variabilis* ATCC 29413-U under different irradiances and CO_2 concentrations. *J Appl Microbiol*, 104:105–121, 2008.

[14] H. Berberoglu, J. Jay, and L. Pilon. Effect of nutrient media on photobiological hydrogen production by *Anabaena variabilis* ATCC 29413. *Int J Hydrogen Energ*, 33(4):1172–1184, 2008.

[15] H Berberoglu and L Pilon. Experimental measurements of the radiation characteristics of *Anabaena variabilis* ATCC 29413-U and *Rhodobacter sphaeroides* ATCC 49419. *Int J Hydrogen Energ*, 32(18):4772–4785, 2007.

[16] H. Berberoglu and L. Pilon. Maximizing the solar to H_2 energy conversion efficiency of outdoor photobioreactors using mixed cultures. *Int J Hydrogen Energ*, 35(2):500–510, 2010.

[17] S. Bertilsson, O. Berglund, D.M. Karl, and S.W. Chisholm. Elemental composition of marine *Prochlorococcus* and *Synechococcus*: Implications for the ecological stoichiometry of the sea. *Limnol and Oceanogr*, 48(5):1721–1731, 2003.

[18] R.B. Bird, W.E. Stewart, and E.N. Lightfoot. *Transport Phenomena*. John Wiley & Sons, New York, 1st edition, 1960.

[19] R.E. Blankenship. *Molecular Mechanisms of Photosynthesis*. Blackwell Science Ltd., Oxford, 2002.

[20] E.G. Bligh and W.J. Dyer. A rapid method of total lipid extraction and purification. *Can J Biochem Phys*, 37(8):911–917, 1959.

[21] M.A. Borowitzka. Commercial production of microalgae: ponds, tanks, tubes, and fermenters. *J Biotechnol*, 70:313–321, 1999.

[22] C. Brindley, F.G. Acien, and J.M. Fernandez-Sevilla. The oxygen evolution methodology affects photosynthetic rate measurements of microal-

gae in well-defined light regimes. *Biotechnol Bioeng*, 106(2):228–237, 2010.

[23] British Nutrition Foundation. n-3 Fatty Acids and Health, 2000. http://www.nutrition.org/uk/home.asp?siteId=43sectionId=686parentSection =341which=.

[24] D. Campbell, V. Hurry, A.K. Clarke, P. Gustafsson, and G. Oquist. Chlorophyll fluorescence analysis of cyanobacterial photosynthesis and acclimation. *Microbiol Mol Biol R*, 62(3):667–83, 1998.

[25] S. Chinnasamy, A. Bhatnagar, R. Hunt, and K. Das. Microalgae cultivation in a wastewater dominated by carpet mill effluents for biofuel applications. *Bioresource Technol*, 101(9):3097–3105, 2010.

[26] Y. Chisti. Biodiesel from algae. *Biotechnol Adv*, 25:294–306, 2007.

[27] Y. Chisti and J. Yan. Energy from algae: Current status and future trends. *Appl Energ*, 88(10):3277–3279, 2011.

[28] A.F. Clarens, E.P. Resurreccion, M.A. White, and L.M. Colosi. Environmental life cycle comparison of algae to other bioenergy feedstocks. *Environ Sci Technol*, 44(5):1813–1819, 2010.

[29] R.C. Cottrell. Introduction: nutritional aspects of palm oil. *The American Journal of Clinical Nutrition*, 53:989S–1009S, 1991.

[30] R. Craggs, P. McAuley, and V. Smith. Wastewater nutrient removal by marine microalgae grown on a corrugated raceway. *Water Resour*, 31:1701–1707, 1997.

[31] R.J. Craggs, S. Heubeck, T.J. Lundquist, and J.R. Benemann. Algal biofuels from wastewater treatment high rate algal ponds. *Water Sci Technol*, 63(4):660–5, January 2011.

[32] M.K. Danquah, R. Harun, R. Halim, and G.M. Forde. Cultivation medium design via elemental balancing for *Tetraselmis suecica*. *Chem Biochem Eng Q*, 24(3):361–369, 2010.

[33] J.G. Day, E.E. Benson, and R.A. Fleck. *In vitro* culture and conservation of microalgae: applications for aquaculture, biotechnology and environmental research. *In Vitro Cell Dev-Pl*, 35:127–136, 1999.

[34] P-G. de Gennes, F. Brochard-Wyart, and D. Quere. *Capillarity and Wetting Phenomena: Drops, Bubbles, Pearls, Waves.* Springer, New York, 1st edition, 2004.

[35] K. Dehesh, A. Jones, D.S. Knutzon, and T.A. Voelker. Production of high levels of 8:0 and 10:0 fatty acids in transgenic canola by overexpression of *ChFatB2*, a thioesterase cDNA from *Cuphea hookeriana*. *Plant J*, 9:167–172, 1996.

[36] A. Demirbas. Use of algae as biofuel sources. *Energ Convers Manage*, 51(12):2738–2749, 2010.

[37] S. Dewald, S. Josiah, and B. Erdkamp. Heating with wood: Producing, harvesting and processing firewood. Technical report, University of Nebraska, Lincoln, Lincoln, NE, 2005.

216

[38] I. Dunn, E. Heinzle, J. Ingham, and J. Prenosil. *Biological reaction engineering: Dynamic modelling fundamentals with simulation examples.* Wiley-VCH, Germany, 2nd edition, 2003.

[39] L.Z. Durand and G. Goldstein. Photosynthesis, photoinhibition, and nitrogen use efficiency in native and invasive tree ferns in Hawaii. *Oecologia*, 126(3):345–354, 2001.

[40] L.S. Fan, R. Leyvaramos, K.D. Wisecarver, and B.J. Zehner. Diffusion of phenol through a biofilm grown on activated carbon particles in a draft-tube 3-phase fluidized-bed reactor. *Biotechnol Bioeng*, 35:279–286, 1990.

[41] G.E. Fogg, W.D.P. Stewart, P. Fay, and A.E. Walsby. *The blue-green algae.* Academic Press, London, 1973.

[42] A.G. Fontes, M.A. Vargas, J. Moreno, M.G. Guerrero, and M. Losada. Changes in the pigment content of *Anabaena variabilis* cells in outdoor culture. *J Plant Physiol*, 137(4):441–445, 1991.

[43] A.M. Gaffney, S.A. Markov, and M. Gunasekaran. Utilization of cyanobacteria in photobioreactors for orthophosphate removal from water. *Appl Biochem Biotechnol*, 91-93:185–193, 2001.

[44] B. Genty, J-M. Briantais, and N.R. Baker. The relationship between the quantum yield of photosynthetic electron transport and quenching of chlorophyll fluorescence. *BBA-Gen Subjects*, 990(1):87–92, 1989.

[45] M.L. Ghirardi, L. Zhang, J.W. Lee, T. Flynn, M. Seibert, E. Greenbaum, and A. Melis. Microalgae: a green source of renewable H_2. *Trends Biotechnol*, 18(12):506–11, 2000.

[46] F. Godia, J. Albiol, J. Perez, N. Creus, F. Cabello, A. Montras, A. Masot, and Ch. Lasseur. The MELISSA pilot plant facility as an integration test-bed for advanced life support systems. *Adv Space Res*, 34:1483–1493, 2004.

[47] C.V. Gonzalez-Lopez, F.G. Acien Fernandez, J.M. Fernandez-Sevilla, J.F. Sanchez Fernandez, M.C. Ceron Garcia, and E. Molina Grima. Utilization of the cyanobacteria *Anabaena* sp. ATCC 33047 in CO_2 removal processes. *Bioresource Technol*, 100:5904–5910, 2009.

[48] C. Gudin and C. Thepenier. Bioconverstion of solar energy into organic chemicals by microalgae. *Adv Biotechnol Process*, 6:73–110, 1986.

[49] C.A. Gueymard, D. Myers, and K. Emery. Proposed reference irradiance spectra for solar energy system testing. *Sol Energy*, 73(6):443–467, 2002.

[50] JP Gustafsson. Visual MINTEQ, 2011. http://www2.lwr.kth.se/English/ OurSoftware/vminteq/.

[51] J. Gutiérrez, M.A. Porta-Gándara, and J.L. Fernández. Passive temperature solar control of an outdoor photobioreactor. *Renew Energ*, 33(8):1892–1903, 2008.

[52] G.M. Hale and M.R. Querry. Optical constants of water in the 200-nm to 2000-nm wavelength region. *Appl Opt*, 12(3):555–563, 1973.

[53] T. Hastie, R. Tibshirani, and J.H. Friedman. *The Elements of Statistical Learning*. Springer, 1st edition, 2003.

[54] M. Heldal, J. Scanlan, S. Norland, F. Thingstad, and N.H. Mann. Elemental composition of single cells of various strains of marine *Prochlorococcus* and *Synechococcus* using X-ray microanalysis. *Limnol Oceanogr*, 48:1732–1743, 2003.

[55] T-Y. Ho, A. Quigg, V. Zoe, A.J. Milligan, P.G. Falkowski, and F.M.M. Morel. The elemental composition of some marine phytoplankton. *J Phycol*, 39:1145–1159, 2003.

[56] F.P. Incropera, D.P. Dewitt, T.L. Bergman, and A.S. Lavine. *Fundamentals of Heat and Mass Transfer*. John Wiley & Sons, Hoboken, NJ, USA, 6th edition, 2007.

[57] J. Jeanfils, M-F. Canisius, and N. Burlioni. Effect of high nitrate concentrations on growth and nitrate uptake by free-living and immobilized *Chlorella vulgaris* cells. *J Appl Phycol*, 5:369–374, 1993.

[58] O. Jorquera, A. Kiperstok, E.A. Sales, M. Embiruçu, and M.L. Ghirardi. Comparative energy life-cycle analyses of microalgal biomass production in open ponds and photobioreactors. *Bioresource Technol*, 101(4):1406–1413, 2010.

[59] S-K. Jung and S.B. Lee. *In situ* monitoring of cell concentration in a photobioreactor using image analysis: comparison of uniform light distribution model and artificial neural networks. *Biotechnol Progr*, 22(5):1443–1450, 2006.

[60] F. Kazemipour, V. Méléder, and P. Launeau. Optical properties of microphytobenthic biofilms (MPBOM): Biomass retrieval implication. *J Quant Spectrosc Ra*, 112(1):131–142, 2011.

[61] J.U. Kreft, C. Picioreanu, J.W. Wimpenny, and M.C. van Loosdrecht. Individual-based modelling of biofilms. *Microbiol*, 147(11):2897–912, 2001.

[62] V. Krivtsov, E.G. Bellinger, and D.C. Sigee. Modelling of elemental associations in *Anabaena*. *Hydrobiologia*, 414:77–83, 1999.

[63] V. Krivtsov, E.G. Bellinger, and D.C. Sigee. Elemental composition of *Microcystis aeruginosa* under conditions of lake nutrient depletion. *Aquat Ecol*, 39(2):123–134, 2005.

[64] K. Kumar, C.N. Dasgupta, B. Nayak, P. Lindblad, and D. Das. Development of suitable photobioreactors for CO_2 sequestration addressing global warming using green algae and cyanobacteria. *Bioresource Technol.*, 102(8):4945–4953, 2011.

[65] K.M. Lehto, H.J. Lehto, and E.A. Kanervo. Suitability of different photosynthetic organisms for an extraterrestrial biological life support

system. *Res Microbiol*, 157(1):69–76, 2006.

[66] Z. Lewandowski and H. Beyenal. *Fundamentals of Biofilm Research.* Taylor & Francis Group, Boca Raton, FL., 2007.

[67] Y. Li, W. Zhou, B. Hu, M. Min, P. Chen, and R.R. Ruan. Integration of algae cultivation as biodiesel production feedstock with municipal wastewater treatment: strains screening and significance evaluation of environmental factors. *Bioresource Technol*, 102(23):10861–10867, 2011.

[68] Q. Liao, Y-J. Wang, Y-Z. Wang, R. Chen, X. Zhu, Y-K. Pu, and D-J. Lee. Two-dimension mathematical modeling of photosynthetic bacterial biofilm growth and formation. *Int J Hydrogen Energ*, 37(20):15607–15615, 2012.

[69] Q. Liao, Y-J. Wang, Y-Z. Wang, X. Zhu, X. Tian, and J. Li. Formation and hydrogen production of photosynthetic bacterial biofilm under various illumination conditions. *Bioresource Technol*, 101(14):5315–5324, 2010.

[70] S.K. Liehr, J. Wayland Eheart, and M.T. Suidan. A modeling study of the effect of pH on carbon limited algal biofilms. *Water Res*, 22(8):1033–1041, 1988.

[71] T. Liu, J. Wang, Q. Hu, P. Cheng, B. Ji, J. Liu, Y. Chen, W. Zhang, X. Chen, L. Chen, L. Gao, C. Ji, and H. Wang. Attached cultiva-

tion technology of microalgae for efficient biomass feedstock production. *Bioresource Technol*, 127:216–222, 2013.

[72] F.A. Lopes Pinto, O. Troshina, and P. Lindblad. A brief look at three decades of research on cyanobacterial hydrogen evolution. *Int J Hydrogen Energ*, 27:1209–1215, 2002.

[73] M.F. Macedo, J.G. Ferreira, and P. Duarte. Dynamic behaviour of photosynthesis-irradiance curves determined from oxygen production during variable incubation periods. *Mar Ecol Prog Ser*, 165:31–43, 1998.

[74] R.K. Mandalam and B.O. Palsson. Elemental balancing of biomass and medium composition enhances growth capacity in high-density *Chlorella vulgaris* cultures. *Biotechnol Bioeng*, 59(5):605–11, 1998.

[75] G. Markou, I. Chatzipavlidis, and D. Georgakakis. Effects of phosphorus concentration and light intensity on the biomass composition of *Arthrospira (Spirulina) platensis*. *World J Microb Biot*, 28(8):2661–70, 2012.

[76] F.J. Marquez, K. Sasaki, N. Nishio, and S. Nagai. Inhibitory effect of oxygen accumulation on the growth of *Spirulina platensis*. *Biotechnol Lett*, 17(2):225–228, 1995.

[77] J.D. Mauseth. *Plant Anatomy*. Benjamin/Cummings, Menlo Park, CA, 1988.

[78] G.C. McLeod. Delayed light action spectra of several algae in visible and ultraviolet light. *J Gen Physiol*, 42(955):243–250, 1958.

[79] A. Melis, M. Spangfort, and B. Andersson. Light-absorption and electron transport balance between photosystem-II and photosystem-I in spinach chloroplasts. *Photochem Photobiol*, 45:129–136, 1987.

[80] J.J. Milledge. Commercial application of microalgae other than as biofuels: a brief review. *Rev Env Sci Biotechnol*, 10(1):31–41, 2010.

[81] R.J. Millington and J.P. Quirk. Permeability of Porous Solids. *T Faraday Soc*, 57:1200–1207, 1961.

[82] A.F. Mills. *Heat Transfer*. Prentice-Hall, Upper Saddle River, NJ, USA, 5th edition, 1999.

[83] A.F. Mills. *Mass Transfer*. Prentice-Hall, Upper Saddle River, NJ, USA, 2001.

[84] M. Mimuro and Y. Fujita. Estimation of chlorophyll a distribution in the pototsynthetic pigment systems I and II of the blue-green alga *Anabaena variabilis*. *Biochim Biophys Acta*, 459:376–389, 1977.

[85] M. Mitra and A. Melis. Optical properties of microalgae for enhanced biofuels production. *Opt Express*, 16(26):21807–21820, 2008.

[86] J.M. Moran and H.N. Shapiro. *Fundamentals of Engineering Thermodynamics*. John Wiley & Sons, Hoboken, NJ, USA, 5th edition, 2004.

[87] F.M.M. Morel and J.G. Hering. *Principles and Applications of Aquatic Chemistry*. John Wiley & Sons, Hoboken, NJ, USA, 1993.

[88] D. Mu, Z-S. Liu, C. Huang, and N. Djilali. Determination of the effective diffusion coefficient in porous media including Knudsen effects. *Microfluid Nanofluid*, 4(3):257–260, 2007.

[89] W. Mulbry, S. Kondrad, C. Pizarro, and E. Kebede-Westhead. Treatment of dairy manure effluent using freshwater algae: Algal productivity and recovery of manure nutrients using pilot-scale algal turf scrubbers. *Bioresource Technol*, 99:8137–8142, 2008.

[90] T.E. Murphy and H. Berberoglu. Cellular photosynthetic rate of fully and partially pigmented *Chlamydomonas reinhardtii* as a function of irradiance. In *Proceedings of IMECE2011*, Denver, CO, 2011.

[91] T.E. Murphy and H. Berberoglu. Effect of algae pigmentation on photobioreactor productivity and scale-up: a light transfer perspective. *J Quant Spectrosc Ra*, 112(18):2826–2834, 2011.

[92] T.E. Murphy and H. Berberoglu. Temperature Fluctuation and Evaporative Loss Rate in an Algae Biofilm Photobioreactor. *J Sol Energ-T ASME*, 134:011002–1–011002–9, 2012.

[93] T.E. Murphy, E. Fleming, L. Bebout, B. Bebout, and H. Berberoglu. A novel microbial cultivation platform for space applications. In *1st An-*

nual International Space Station Research and Development Conference, Denver, CO, 2012.

[94] T.E. Murphy, K. Macon, and H. Berberoglu. Multispectral image analysis for algal biomass quantification. *Biotechnology progress*, 29(3):808–16, May 2013.

[95] P.L. Nagler, E.P. Glenn, and T. Lewis Thompson. Comparison of transpiration rates among saltcedar, cottonwood and willow trees by sap flow and canopy temperature methods. *Agr Forest Meteorol*, 116(1-2):73–89, 2003.

[96] Y. Nakamura, H. Satoh, S. Okabe, and Y. Watanabe. Photosynthesis in sediments determined at high spatial resolution by the use of microelectrodes. *Water Res*, 38(9):2439–2447, 2004.

[97] T. Naumann, Z. Cebi, B. Podola, and M. Melkonian. Growing microalgae as aquaculture feeds on twin-layers, a novel solid state photobioreactor (in press). *J Appl Phycol*, 2013.

[98] D.R. Noguera, S. Okabe, and C. Picioreanu. Review on biofilm modeling: present status and future directions. *Wat Sci Tech*, 39(7):273–278, 1999.

[99] G. Norrman, W.G. Characklis, and J.D. Breyers. Control of microbial fouling in circular tubes with chlorine. *Dev Ind Microbiol*, 18:581–590, 1977.

[100] Oilgae. Algae Oil Extraction. http://www.oilgae.com/algae /oil/extract/extract.html, 2013.

[101] A. Ozkan, K. Kinney, L. Katz, and H. Berberoglu. Reduction of water and energy requirement of algae cultivation using an algae biofilm photobioreactor. *Bioresource Technol*, 114:542–548, 2012.

[102] M. Packer. Algal capture of carbon dioxide; biomass generation as a tool for greenhouse gas mitigation with reference to New Zealand energy strategy and policy. *Energ Policy*, 37(9):3428–3437, 2009.

[103] D. Pasquini, M.N. Belgacem, A. Gandini, and A.A. da Silva Curvelo. Surface esterification of cellulose fibers: characterization by DRIFT and contact angle measurements. *J Colloid Interf Sci*, 295(1):79–83, 2006.

[104] C. Picioreanu, M.C.M. van Loosdrecht, and J.J. Heinjen. Mathematical modeling of biofilm structure with a hybrid differential-discrete cellular automaton approach. *Biotechnol Bioeng*, 58(1):101–116, 1998.

[105] P.T. Pienkos and A. Darzins. of microalgal-derived biofuels . *Biofuel Bioprod Bior*, 3:431–440, 2009.

[106] L. Pilon, H. Berberolu, and R. Kandilian. Radiation transfer in photobiological carbon dioxide fixation and fuel production by microalgae. *J Quant Spectrosc Ra*, 112:2639–2660, 2011.

[107] C. Poynton. *Digital Video and HDTV: Algorithms and interfaces.* Morgan Kaufmann Publishers, San Francisco, CA, 2003.

[108] O. Pulz and W. Gross. Valuable products from biotechnology of microalgae. *Appl Microbiol Biot*, 65(6):635–648, 2004.

[109] V. Reipa, J. Almeida, and K.D. Cole. Long-term monitoring of biofilm growth and disinfection using a quartz crystal microbalance and reflectance measurements. *J Microbiol Meth*, 66:449–459, 2006.

[110] N.B. Reppas and C.P. Ridley. Methods and compositions for the recombinant biosynthesis of n-alkanes (USPTO 7794969), 2010.

[111] N.P. Revsbech, B.B. Jorgensen, T.H. Blackburn, and Y. Cohen. Microelectrode studies of the photosynthesis and O_2, H_2S, and pH profiles of a microbial mat. *Limnol Oceanogr*, 28(6):1062–1074, 1983.

[112] L. Rodolfi, G. Chini Zittelli, N. Bassi, G. Padovani, N. Biondi, G. Bonini, and M.R. Tredici. Microalgae for oil: strain selection, induction of lipid synthesis and outdoor mass cultivation in a low-cost photobioreactor. *Biotechnol Bioeng*, 102(1):100–12, 2009.

[113] U. Schuchardt, R. Sercheli, and R.M. Vargas. Transesterification of vegetable oils: A review. *J Braz Chem Soc*, 9:199–210, 1998.

[114] S.A. Scott, M.P. Davey, J.S. Dennis, I. Horst, C.J. Howe, D.J. Lea-Smith, and A.G. Smith. Biodiesel from algae: challenges and prospects. *Curr Opin Biotechnol*, 21(3):277–86, 2010.

[115] F. Seibert and M. Poenie. Non-dispersive process for insoluble oil recovery from aqueous slurries (patent 13/006032), 2011.

[116] P.K. Sharma and G.S. Singhal. Influence of photoinhibition peroxidation on photosynthesis and lipid. *J Photochem Photobiol B*, 13:83–94, 1992.

[117] B. Sialve, N. Bernet, and O. Bernard. Anaerobic digestion of microalgae as a necessary step to make microalgal biodiesel sustainable. *Biotechnol Adv*, 27(4):409–16, 2009.

[118] R. Siegel and J. Howell. *Thermal Radiation Heat Transfer*. Taylor & Francis, New York, 4th edition, 2002.

[119] D.C. Sigee, J. Teper, and E. Levado. Elemental composition of the cyanobacterium *Anabaena flos-aquae* collected from different depths within a stratified lake. *Eur J Phycol*, 34(5):477–485, 1999.

[120] F.R. Silva-Aciares and C.E. Riquelme. Comparisons of the growth of six diatom species between two configurations of photobioreactors. *Aquacult Eng*, 38(1):26–35, 2008.

[121] R.N. Singh and S. Sharma. Development of suitable photobioreactor for algae production: A review. *Renew Sust Energ Rev*, 16(4):2347–2353, 2012.

[122] D.A. Skoog and J.J. Leary. *Principles of Instrumental Analysis*. Saunders College Publishing, Austin, 4th edition, 1992.

[123] P. Spolaore, C. Joannis-Cassan, E. Duran, and A. Isambert. Commercial applications of microalgae. *J Biosci Bioeng*, 101(2):87–96, 2006.

[124] R.Y. Stanier, R. Kunisawa, M. Mandel, and G. Cohen-Bazire. Purification and properties of unicellular blue-green algae (order Chroococcales). *Bacteriol Rev*, 35(2):171–205, 1971.

[125] S.E. Stevens, C.O.P. Patterson, and J. Myers. The production of hydrogen peroxide by blue-green algae: a survey. *J Phycol*, 9:427–430, 1973.

[126] P.S. Stewart. A review of experimental measurements of effective diffusive permeabilities and effective diffusion coefficients in biofilms. *Biotechnol Bioeng*, 34(3):261–272, 1999.

[127] P.S. Stewart. Diffusion in biofilms. *J Bacteriol*, 185(5):1485–1491, 2003.

[128] A.L. Sumner, E.J. Menke, Y. Dubowski, J.T. Newberg, R.M. Penner, J.C. Hemminger, L.M. Wingen, and B.J. Finlayson-Pitts. The nature of water on surfaces of laboratory systems and implications for heterogeneous chemistry in the troposphere. *Phys Chem Chem Phys*, 6:604–613, 2004.

[129] D.A. Sveshnikov, N.V. Sveshnikov, K.K. Rao, and D.O. Hall. Hydrogen metabolism of mutant forms of Anabaena variabilis in continuous cultures and under nutritional stress. *FEMS Microbiol Lett*, 147:297–301, 1997.

[130] W.A. Thompson, G.C. Stocker, and P.E. Kriedemann. Growth and photosynthetic response to light and nutrients of *Flindersia brayleyana* F . Muell., a rainforest tree with broad tolerance to sun and shade. *Aust J Plant Physiol*, 15:299–315, 1988.

[131] A.A. Tsygankov, L.T. Serebryakova, K.K. Rao, and D.O. Hall. Acetylene reduction and hydrogen photoproduction by wild-type and mutant strains of *Anabaena* at different CO_2 and O_2 concentrations. *FEMS Microbiol Lett*, 167:13–17, 1998.

[132] O. Wanner, H. Eberl, E. Morgenroth, D. Noguera, C. Picioreanu, B. Rittman, and M. van Loosdrecht. *Mathematical Modeling of Biofilms*. IWA Publishing, London, 2006.

[133] T.D. Wheeler and A.D. Stroock. The transpiration of water at negative pressures in a synthetic tree. *Nature*, 455(7210):208–12, 2008.

[134] F. White. *Viscous Fluid Flow*. McGraw-Hill, 3rd edition, 2005.

[135] S. Wilcox and W. Marion. Users manual for TMY3 data sets. Technical report, National Renewable Energy Laboratory, Golden, CO, 2008.

[136] G. Wolf, C. Picioreanu, and M.C.M. van Loosdrecht. Kinetic modeling of phototrophic biofilms : The PHOBIA model. *Biotechnol Bioeng*, 97(5):1064–1079, 2007.

[137] Y. Yang, Q. Liao, X. Zhu, H. Wang, R. Wu, and D-J. Lee. Lattice Boltzmann simulation of substrate flow past a cylinder with PSB biofilm for

bio-hydrogen production. *Int J Hydrogen Energ*, 36(21):14031–14040, 2011.

[138] F. Zhang, L-H. Cheng, W-L. Gao, X-H. Xu, L. Zhang, and H-L. Chen. Mechanism of lipid extraction from *Botryococcus braunii* FACHB 357 in a biphasic bioreactor. *J Biotechnol*, 154(4):281–4, 2011.

[139] F. Zhang, L-H. Cheng, X-H Xu, L. Zhang, and H-L. Chen. Screening of biocompatible organic solvents for enhancement of lipid milking from *Nannochloropsis* sp. *Proc Biochem*, 46(10):1934–1941, 2011.

[140] C.J. Zhu and Y.K. Lee. Determination of biomass dry weight of marine microalgae. *J Appl Phycol*, 9:189–194, 1997.

Vita

Thomas Eugene Murphy attended York Community High School in Elmhurst, IL. He earned a Bachelor of Science with Honors in Mechanical Engineering from Brown University in May 2009. He began graduate study in the Thermal/Fluid Systems track of the Mechanical Engineering Department at the University of Texas at Austin in the fall of 2009. In January 2010, he began research with Dr. Halil Berberoglu in the Solar Energy and Renewable Fuels Laboratory, where his work has primarily focused on energy and mass transport processes in novel algae cultivation environments for energy and water efficient biofuel production. During the summers of 2011 and 2012, he was also a visiting researcher at NASA Ames Research Center in Moffett Field, CA in the laboratory of Leslie Pruffert-Bebout.

Permanent address: 261 E. St. Charles Rd., Elmhurst IL, 60126

This dissertation was typeset with LaTeX[†] by the author.

[†]LaTeX is a document preparation system developed by Leslie Lamport as a special version of Donald Knuth's TeX Program.